Comparative exoplanetology using thermal phase curves and Bayesian hierarchical modelling

Dylan Keating

April 15, 2021

McGill University

Tiohtià:ke / Montréal, QC

A thesis submitted for the degree of Doctor of Philosophy.

©Dylan Keating 2021

Contents

Abstract

Short-period gas giants, more commonly known as hot Jupiters, are the most well-studied class of exoplanets to date. They are tidally locked into synchronous rotation around their host stars, with permanent daysides and permanent nightsides. Around 100 hot Jupiters have had their atmospheres characterized using infrared observations with the *Spitzer* and *Hubble* space telescopes. This dissertation presents my work looking for trends in dayside and nightside temperatures on hot Jupiters, using observations of secondary eclipses and full-orbit phase curves. I compare and contrast the *Spitzer* phase curves of WASP-43b and Qatar-1b, two planets that receive the same amount of irradiation from their host stars, yet unexpectedly have very different bright spot offsets: WASP-43b exhibits a significant eastward shifted bright spot, whereas the bright spot of Qatar-1b is consistent with no such shift. The discrepancy in circulation patterns points to the importance of secondary parameters like rotation rate and surface gravity, the presence or absence of clouds, and magnetic effects in determining atmospheric conditions on hot Jupiters. Using a larger suite of phase curves and their corresponding longitudinal brightness maps, I show that all hot Jupiters have nightside temperatures around 1100 K, which we attribute to a universal nightside cloud composition, the most likely culprit being silicate clouds. Lastly, I show how to use Bayesian hierarchical models to simultaneously fit multiple *Spitzer* secondary eclipses of hot Jupiters. For repeated observations of a single planet, this allows us to pool information across epochs and robustly measure dayside temperature variability. For observations of multiple planets, this enables us to share information across different planets by accounting for the expectation that dayside temperatures scale with instellation. In both cases, estimates of parameters like secondary eclipse depths benefit from improved precision. Hierarchical modelling is useful for all statistical surveys of exoplanets, and this work helps to set the stage for surveys that will be undertaken with upcoming next-generation space telescopes like *James Webb* and *Ariel*.

Résumé

Les gazeuses géantes possédant une courte période orbitale, plus communément appelées "Jupiters chaudes", sont la classe d'exoplanètes la mieux étudiée à ce jour. Pour ces planètes, on observe une synchronisation entre la rotation autour de leur axe et la révolution autour de leur étoile hôte. De plus, ces planètes sont caractérisées par leur présentation permanente de la même face à leur étoile, résultant en des faces distinctes et permanentes diurne et nocturne de la planète. Des données obtenues avec les télescopes spatiaux *Spitzer* et *Hubble* nous ont permis de caractériser l'atmosphère d'une centaine de Jupiters chaudes. Cette thèse résume l'ensemble de mon travail servant à l'exploration des tendances des températures des faces diurne et nocturne des Jupiters chaudes, à partir d'observations d'éclipses secondaires et de courbes de phase d'orbite complète. En premier lieu, je compare les courbes de phase *Spitzer* de WASP-43b et de Qatar-1b. Quoique ces deux planètes reçoivent la même quantité d'irradiation de leurs étoiles hôtes, elles présentent, étonnement, des décalages de points lumineux très différents : WASP-43b a un point brillant significativement décalé vers l'est, alors que nous avons trouvé que le point brillant de Qatar-1b n'a pas ce décalage. La divergence des modèles de circulation souligne l'importance des paramètres secondaires, tel que la période de rotation et la gravité de surface, la présence ou l'absence de nuages ainsi que les effets des champs magnétiques, dans la détermination des conditions atmosphériques sur les Jupiters chaudes. En utilisant une collection de courbes de phase et leurs cartes de luminosité longitudinale correspondantes, je démontre que toutes les Jupiters chaudes ont des températures nocturnes d'environ 1100 K. Nous attribuons cette observation à une espèce universelle de nuages nocturnes, probablement, étant des nuages de silicate.

Finalement, j'applique des modèles hiérarchiques Bayésiens pour ajuster simultanément plusieurs éclipses secondaires *Spitzer* de Jupiters chaudes. Pour les observations répétées d'une seule planète, cela nous permet de mettre en commun les informations entre les époques et de mesurer de manière robuste la variabilité de la température diurne. Pour les observations de plusieurs planètes, cela nous permet de partager les informations entre les différentes planètes en tenant compte du fait que les températures diurnes sont proportionnelles à l'instellation. Dans les deux cas, les estimations de paramètres, tels que les profondeurs d'éclipse secondaire, bénéficient d'une amélioration en termes de précision. La modélisation hiérarchique est utile pour toutes les études statistiques des exoplanètes, et permet de préparer le terrain pour les études qui seront faites avec les télescopes spatiaux de nouvelle génération à venir, comme *James Webb* et *Ariel*.

List of Figures

List of Tables

Acknowledgments

To my supervisor, Nick Cowan. Your support over the years is immeasurable. Thanks for your guidance and encouragement, even though my career trajectory was not an academic one. This has been an extremely fun few years working in an exciting, fast-moving field and I'm glad I got to be an inaugural member of your group at McGill.

To my comrades Taylor and Lisa, thanks for sharing the journey. I appreciated having you both to bounce ideas off of, and as conference compatriots. Best of luck with wherever life takes you next.

To the McGill Space Institute. Thanks for providing a comfortable and stimulating house on the hill. I still salivate when 3pm rolls around, thinking about the daily coffee and cookies sessions.

To my Mom. Among many other things, you gave me a love of reading and a curiosity about the world. I still remember how to spell australopithecus, almost thirty years later. You have such a big heart and compassion for people and you make the world a better place.

To Fiona. Merci for keeping me positive and challenging me intellectually, and teaching me how to relax (I'm still trying). I don't know how I would have made it through this past year without laughing together. I can't wait to jab vaccines into our arms and finally see the world together. JTM.

Lastly, I want to acknowledge that McGill University is located on unceded Indigenous lands. Tiohtià:ke/Montréal is historically known as a gathering place for many First Nations. The Kanien'kehá:ka Nation is recognized as the custodians of the lands and waters on which McGill University is situated.

Format of thesis

This thesis is comprised of three published manuscripts, and one that is currently under review. Chapter 1 serves as a literature review to motivate the questions explored in the chapters that follow. The manuscript in Chapter 2 was published in *The Astrophysical Journal Letters*. Chapter 3 was published in *Nature Astronomy*. The manuscript in Chapter 4 was published in *The Astronomical Journal*. Lastly, the manuscript in Chapter 5 is currently under review in *Monthly Notices of the Royal Astronomical Society*.

Contribution to original knowledge

This doctoral work contributed to the detailed understanding of two individual hot Jupiter exoplanets, as well as to the understanding of statistical trends across dozens of hot Jupiters.

In Chapter 2, I describe our paper titled "Revisiting the Energy Budget of WASP-43b: Enhanced Day-Night Heat Transport" (Keating and Cowan, 2017). In this paper we showed that the published full-orbit phase curve of WASP-43b was unphysical because it required negative brightness on the planet's nightside, or a negative nightside temperature. After correcting the unphysical regions of the phase curve, we showed that the planet's nightside temperature was in fact close to 1000 K. Additionally, we showed that the dayside flux of the planet was likely overestimated because the authors of the original paper had neglected reflected light when interpreting the *Hubble* Wide Field Camera 3 measurements.

Chapter 3 describes our paper titled "Uniformly hot temperatures on short period gas-giants" (Keating et al., 2019), which was a meta-analysis of twelve hot Jupiters with published full-orbit phase curves from *Spitzer* and *Hubble*. A few of these planets had the same issues of unphysical phase curves, so we implemented two ways of correcting the phase curves. One used disk-integrated temperatures, and the other considered longitudinal brightness maps. Using both methods we showed that hot Jupiters all seem to have the same nightside effective temperature, $\sim$1100 K, despite having dayside temperatures that span a range of 2000 K between the coldest and hottest planet. We attributed this to a common nightside cloud species that condenses at a temperature slightly higher than $\sim$1100 K and emits at a cloud top temperature of $\sim$1100 K. Based on cloud condensation curves and the range of temperatures and pressures probed by *Spitzer*, these are most likely silicate clouds. Our paper was the first to point out this common nightside effective temperature and attribute it to a common cloud species.

Chapter 4 presents "Smaller than expected bright-spot offsets in Spitzer phase curves of the hot Jupiter Qatar-1b" (Keating et al., 2019). This was the first published *Spitzer* phase curve observations of Qatar-1b, a hot Jupiter that has the same irradiation temperature as WASP-43b and HD 209458b. I used two separate reduction and analysis pipelines, in order to compare the best-fit phase curve parameters for Qatar-1b. This had never been done by a single author before because at the time *Spitzer* pipelines were proprietary to each research group. We found that the phase curve of Qatar-1b was consistent with its brightest spot being located at the substellar point, despite predictions that the bright spot would be shifted eastward as was observed for WASP-43b and HD 209458b. The differences in dayside heat advection in these three planets points to the importance of secondary physical parameters for understanding the atmospheric circulation of hot Jupiters.

In Chapter 5 "Atmospheric characterization of hot Jupiters using hierarchical models of Spitzer observations" (Keating et al., 2020), we present the first application of Bayesian hierarchical modelling to atmospheric characterization of hot Jupiters. Hierarchical modelling is a powerful way of sharing information across observations of disparate targets, or repeated observations of the same target. We showed hierarchical models make better predictions than the types of analyses typically performed on suites of multiple observations. Additionally, we did not find evidence of a previously observed trend that hotter planets are brighter at 4.5 μm than 3.6 μm

Contribution of authors

The works in Chapters 2 to 5 were completed under the supervision of Dr Nicolas B. Cowan at the McGill Department of Physics and Department of Earth and Planetary Science. The work in Chapter 4 was co-supervised by Dr Kevin B. Stevenson at the Space Telescope Science Institute.

The manuscript that comprises Chapter 2 was published in *The Astrophysical Journal Letters* in November 2017 and is authored by myself and Nicolas B. Cowan. N.B.C. discussed ideas and contributed to writing the manuscript. I wrote the code, performed the analysis, and wrote the bulk of the manuscript.

The manuscript presented in Chapter 3 was published by *Nature Astronomy* on August 26 2019 and is authored by myself, Nicolas B. Cowan, and Lisa Dang. I collected the published phase curve parameters, wrote the code to perform the analysis, and wrote the bulk of the manuscript. N.B.C. discussed ideas and contributed to writing the manuscript. L.D. provided the *Spitzer* analysis pipeline, and helped analyze two phase curves.

The manuscript in Chapter 4 was published in *The Astronomical Journal* in May 2020, and is authored by myself, Kevin B. Stevenson, Nicolas B. Cowan, Emily Rauscher, Jacob L. Bean, Taylor Bell, Lisa Dang, Drake Deming, Jean-Michel Désert, Y. Katherina Feng, Jonathan J. Fortney, Tiffany Kataria, Eliza M.-R Kempton, Nikole Lewis, Michael R. Line, Megan Mansfield, Erin May, Caroline Morley, and Adam P. Showman. K.B.S. was the principal investigator of the observing proposal that the data were taken from. K.B.S co-wrote the *Spitzer* reduction and analysis pipeline POET, and taught me how to use it. I reduced and analyzed the two *Spitzer* phase curves and wrote most of the manuscript with help from K.B.S. and N.B.C. E.R. contributed text to the discussion regarding GCM predictions and clouds. L.D. and T.B. cowrote the other pipeline that I used. All authors contributed useful feedback and edits to the manuscript.

The manuscript in Chapter 5 is currently under review in *Monthly Notices of the Royal Astronomical Society*. Shortly before submitting this dissertation, I received notice from the journal that the reviewer recommended the manuscript for publication contingent upon some moderate revisions. I wrote the code, performed the analysis, and wrote the manuscript. N.B.C. discussed ideas, gave valuable feedback, and helped edit the manuscript.

1 Introduction

It has been just over a quarter century since we first learned that stars other than the Sun also host planets. Over 4000 exoplanets have been confirmed since then, and the latest estimates suggest that the majority of stars are likely to host planets (Gaudi et al., 2020). Remarkably, nearly all of the known planets are unlike the solar system planets in terms of radius, mass, and orbital period. Some of these are several times the size of Earth— so-called super-Earths, like the lava planet 55 Cnc e (McArthur et al., 2004; Fischer et al., 2008; Dawson and Fabrycky, 2010), which receives so much heat from its star that its rocky surface might be molten. There are also multi-planet systems, like the archetypal TRAPPIST-1 system, whose seven planets all orbit their host star closer than the distance between Mercury and our Sun. Still others seem to be straight out of science fiction: circumbinary planets like TOI 1338b (Kostov et al., 2020), or the triple-star terresterial planet LTT 1445Ab (Winters et al., 2019).

Most planets have been discovered using two methods: the transit method and the radial velocity method. A transit occurs when a planet passes in front of its host star, blocking out a fraction of starlight. Transit surveys stare at the night sky continuously to look for stars that periodically decrease in brightness due to a planet passing in front of its host star. The radial velocity method is more subtle— as a planet orbits its host star, it exerts a gravitational force and causes the star to wobble slightly. By measuring the Doppler shift in stellar spectral lines as this occurs, it is possible to measure the line-of sight velocity and infer a lower limit on the mass of a planet.

Two less common planet detection methods are microlensing and direct imaging. Microlensing uses unseen planets as gravitational lenses to focus the light and temporarily brighten dim background stars. Direct imaging is conceptually the simplest method, because it amounts to taking a resolved image of the planet orbiting its star. It is also the most challenging in practice because it requires sufficiently massive, hot planets far enough away from their host stars, for which there are not many examples. Direct imaging has only been used to observe about a dozen planets. For the time being, indirect methods are the most successful ways to study exoplanets.

This thesis will focus on a class of planets known as hot Jupiters, gas giants similar in radius and mass to Jupiter but with extremely short orbital periods around their host stars. Of all the nearby F, G, and K type stars, 1% are believed to host hot Jupiters (Wright et al., 2012). Their close-in orbits means that hot Jupiters receive extreme amounts of stellar flux, 1000—10000 times more flux than Earth receives from the Sun. Based on their ages they are expected to be tidally locked into synchronous rotation, with permanent daysides that face towards their host stars, and permanent nightsides that face the darkness of space (Showman and Guillot, 2002). This leads to atmospheric dynamics unlike those seen for the solar system gas giants.

1.1 Observing hot Jupiters

Hot Jupiters are not resolvable from their host stars with current telescope capabilities. Fortunately, most of the hot Jupiters we know of are transiting planets, and we can study them indirectly by measuring the combined flux from the planet and star. Stars that host hot Jupiters emit most of their radiation at visible wavelengths, whereas hot Jupiters emit most of their radiation in the infrared. For this reason, infrared observations yield the highest signal-to-noise ratio for hot Jupiter atmospheric emission.

As a hot Jupiter orbits its star the total flux of the system changes periodically, which can be used to make a differential measurement. When a planet transits, the fraction of blocked light, or transit depth, gives the ratio of the planetary radius to stellar radius at the observing wavelength. A half orbit later, during the secondary eclipse, the planet passes behind the star. Just before and after the eclipse, the combined planetary

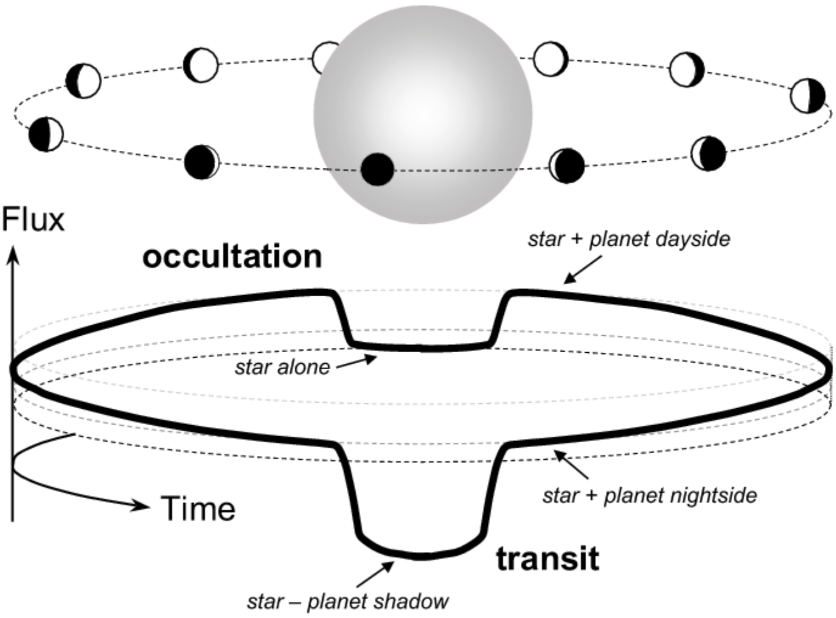

Figure 1.1: Depiction of a phase curve of a transiting planet from Winn (2010). A full-orbit phase curve is a measurement of the changing flux as a planet orbits its host star. During a transit, the planet blocks out a significant amount of starlight. The transit depth is equal to the ratio of the planetary radius divided by the stellar radius, all squared. A secondary eclipse is sometimes called an occultation. Just before and after the secondary eclipse, the planets dayside is visible, which manifests as an increase of the total flux. Subtracting the stellar flux gives the dayside flux of the planet, which can be used to calculate the planets dayside brightess temperature.

and stellar flux peaks, as the hot dayside of the planet is visible. When measuring in the infrared, this gives the ratio of the dayside planetary flux to the stellar flux, which can be used to calculate the dayside brightness temperature of the planet. Between the transit and eclipse the sinusoidal phase variations of the planet are observable, as different parts of the planet are revealed. The phase variations can be used to measure the disk-integrated brightness temperature as a function of orbital phase, and also to infer the longitudinal brightness map of a planet (Cowan and Agol, 2008). The amplitude of the phase variations can be used to measure the nightside temperature of a planet.

In all, a full-orbit phase curve consists of a transit, a secondary eclipse, and phase variations, and is the best way to test theoretical predictions for hot Jupiter atmospheric dynamics. See Figure 1.1 for a cartoon depiction. Because hot Jupiter orbital periods are typically a few days or less, it is feasible to continuously observe an entire orbit.

1.2 The Spitzer space telescope

Most hot Jupiter atmospheric characterization has been done using the *Spitzer* and *Hubble* space telescopes, as well as using ground-based photometry and high resolution spectroscopy. This thesis will mainly focus on phase curve and secondary eclipses observations taken with the *Spitzer* space telescope. An artist's depiction of the telescope can be seen in Figure 1.2. *Spitzer* was not originally designed to observe exoplanets, but exoplanet science turned out to be a big part of its legacy (Deming and Knutson, 2020). Their large size and hot temperatures mean that hot Jupiters were the best candidates to study with *Spitzer*, which made the first detections of infrared light emitted by a transiting planet (Deming et al., 2005; Charbonneau et al., 2005). The lessons learned from adapting *Spitzer* to perform hot Jupiter science helped to refine and greatly extend the original mission (Deming and Knutson, 2020; Ingalls et al., 2016).

In its first phase, the telescope was cryogenically cooled and could observe photometrically at 3.6 μm, 4.5 μm, 5.8 μm, and 8 μm using the Infrared Array Camera (IRAC)

Figure 1.2: Artist's depiction of the *Spitzer* space telescope. Courtesy: NASA/JPL-Caltech

instrument (Fazio et al., 2004), and spectroscopically at 5.3 μm to 38 μm using the Infrared Spectrograph (IRS) instrument (Houck et al., 2004). This phase lasted from 2003 to 2009, when the telescope ran out of cryogen. Only a handful of planets were observed using the full capabilities of IRAC and IRS. The subsequent Spitzer Warm Mission, which lasted until early 2020, allowed for Channels 1 and 2 (3.6 μm and 4.5 μm) of IRAC to be used despite the lack of cryogen. Most exoplanet observations were performed during the Warm Mission.

Although we can't study individual exoplanets with the same detail as we can study the solar system planets, comparative exoplanetology has the advantage of sheer numbers. In total, IRAC observations have been used to study the atmospheres of around a hundred hot Jupiters by observing transits, secondary eclipses, and planetary phase variations at 3.6 and 4.5 μm (Cowan and Agol, 2011a; Sing et al., 2016; Schwartz and Cowan, 2015; Schwartz et al., 2017; Parmentier and Crossfield, 2018; Zhang et al., 2018; Keating et al., 2019, 2020; Baxter et al., 2020; Bell et al., 2020).

1.3 Predictions

Early predictions for hot Jupiter atmospheric circulation used general circulation models (GCMs), which are also used to model Earth's climate. GCMs solve the Navier-Stokes equations of fluid motion for large scale atmospheric flows. They are computionally intensive to run, so most use various levels of approximations to make them computationally tractable (Fortney et al., 2021).

No matter the level of sophistication, all hot Jupiter GCMs predict qualitatively similar features (Heng and Showman, 2015). For instance, the large day-night temperature differences should lead to several-kilometer per second winds in the atmospheres of hot Jupiters that transport heat from their daysides to their nightsides. These winds would be fastest at the equator and directed eastward, the same direction as the planet's spinward rotation (Showman and Guillot, 2002). The hottest part of a hot Jupiter atmosphere is predicted to be shifted to the east of the substellar point. Additionally, the atmospheric dynamics should depend strongly on the amount of incoming stellar radiation, quantified by the irradiation temperature $T_0 = T_{\rm eff}\sqrt{\frac{R_\star}{a}}$, where $T_{\rm eff}$ is the stellar effective temperature and $\frac{R_\star}{a}$ is the ratio of the stellar radius to the semi-major axis of the planet's orbit. In other words, the irradiation temperature depends on how hot the star is, how big the star is, and how closely the planet orbits.

1.4 Early phase curve results

The first continuous phase curve was observed for HD 189733b, and spanned just over half an orbit (Knutson et al., 2007). It was taken at 8 μm using the Infrared Array Camera onboard the *Spitzer* space telescope. The phase curve showed that the brightest longitude of HD 189733b's atmosphere was shifted $16 \pm 6°$ east of the substellar point, as seen in Figure 1.3. The planet had a hot dayside temperature, 1212 ± 11 K, and a cooler but still hot nightside temperature of 973 ± 33 K, meaning that HD 189733b transports a moderate amount of heat from its dayside to its nightside.

The amount of heat a planet can transport from its dayside to its nightside is determined by two competing timescales. The radiative timescale is how fast a planet can re-radiate the flux it receives, and the advective timescale is how fast the planet can transport heat from one hemisphere to another. The radiative timescale is inversely

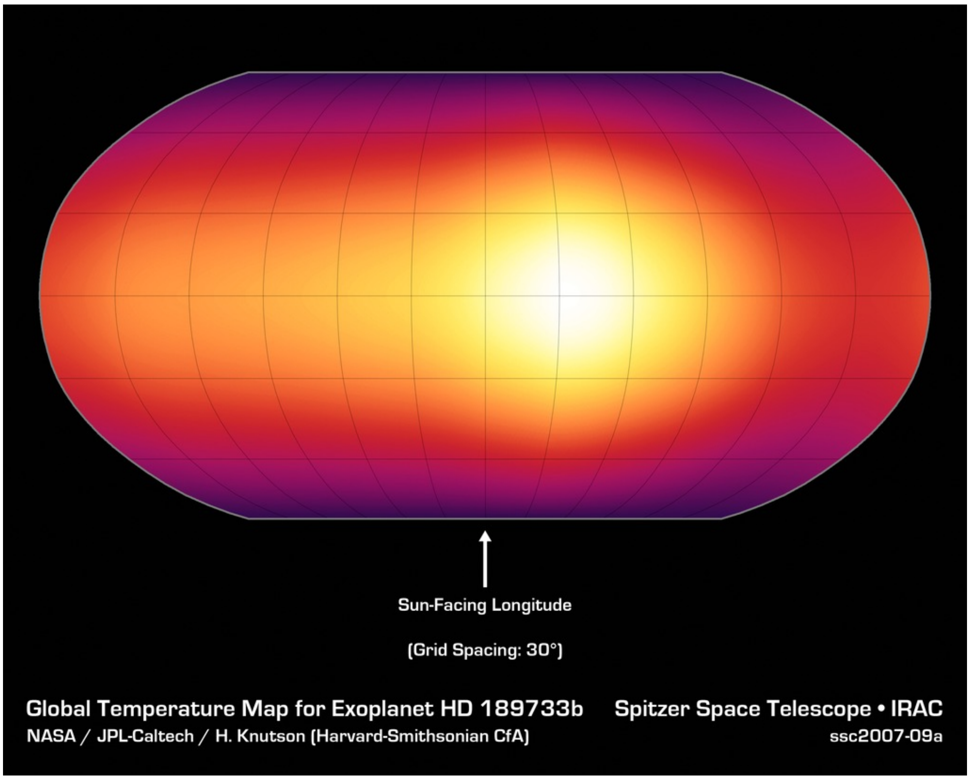

Figure 1.3: The first map of an extrasolar planet, for the hot Jupiter HD 189733b (Knutson et al., 2007). The brightest part of the planet's atmosphere is shifted $16 \pm 6°$ east of the substellar point, matching predictions from general circulation models. Courtesy: NASA/JPL-Caltech

related to planetary irradiation temperature, raised to the third power (Showman and Guillot, 2002; Cowan and Agol, 2011a). The advective timescale is inversely related to the wind speed. Planets that receive more irradiation from their host stars are expected to transport heat less efficiently from day to night.

Subsequent phase curve measurements confirmed significant eastward offsets and day-night heat transport for other hot Jupiters, like HD 209458b, which has a higher irradiation temperature than HD 189733b. The phase curve of HD 209458b showed an offset of $40 \pm 6°$ east (Zellem et al., 2014). The measured dayside temperature was 1499 ± 15 K and the nightside temperature was 972 ± 44 K, which means that HD 209458b is less efficient at transporting heat from day to night than HD 189733b, in line with predictions (Showman et al., 2008).

All else being equal, two hot Jupiters that receive the same amount of stellar irradiation should have the same atmospheric circulation patterns. Any discrepancies must be due to other differences, like rotation rate, mass, radius, or metallicity. Comparing two planets with the same irradiation temperature, but different planetary and stellar physical parameters should help untangle the effects of those secondary parameters. The planet WASP-43b has the same irradiation temperature as HD 209458b, but a higher mass, smaller radius, and shorter rotational period. The initial published phase curves suggested that WASP-43b had a hot dayside but was emitting no heat from its nightside, meaning it transported no heat from day to night (Stevenson et al., 2014, 2017), unlike GCM predictions for this planet (Kataria et al., 2015).

1.5 Nightside temperatures

Dayside temperatures on hot Jupiters are predicted and observed to increase proportional to their irradiation temperatures (Schwartz and Cowan, 2015; Schwartz et al., 2017; Garhart et al., 2020; Baxter et al., 2020; Bell et al., 2020). For nightside temperatures the picture is more complicated: planets must reradiate all the flux they receive, and the timescale for this to happen depends strongly on the amount of incoming stellar flux. The more flux a planet receives, the faster it radiates the flux back to space. The wind speed and hence advective time scale are thought to be determined by the complex interplay of physical processes in hot Jupiter atmospheres: magnetic effects, coriolis forces, gravity waves, and hydrogen dissociation all conspire to set the wind speeds (Komacek and Showman, 2016; Komacek et al., 2017; Zhang and Showman, 2017; Bell and Cowan, 2018; Tan and Komacek, 2019). There is no simple prediction for how nightside temperatures should scale with irradiation temperature.

1.6 Bayesian inference

Most exoplanet research makes use of Bayesian methods to fit astrophysical models to observations. For instance, we may be interested in the amplitude and offset of a planet's phase variations, which in the simplest case can be described by a sinusoid with an amplitude and offset. Bayesian inference allows us determine the most likely values of the amplitude and offset, along with how certain (or uncertain) we are about these values, given the data and any prior knowledge.

Bayes' theorem states that the probability of a model's parameters, given the data, is proportional to the probability of the data given the model parameters multiplied by the ratio of the prior probabilities (Gelman et al., 2014; McElreath, R., 2020). Mathematically, Bayes' theorem looks like:

$$P(\text{model} \mid \text{data}) = \frac{\mathrm{P}(\text{data} \mid \text{model})\ \mathrm{P}(\text{model})}{\mathrm{P}(\text{data})}. \tag{1.1}$$

The term on the left is called the posterior, the first term in the numerator on the right is called the likelihood, the second term in the numerator is called the prior, and the term in the denominator is called the marginal likelihood; these are all probability distributions. To make inferences, we use the posterior probability to calculate the most probable values and uncertainties for our model parameters.

For some models, we can analytically calculate the posterior. For low-dimensional models with no analytic solution, their posteriors can be approximated by trying many combinations of parameters values and calculating the likelihood; this is known as a grid search. A grid search quickly becomes intractable as the number of parameters is increased; we must instead approximate the posterior by sampling from it in a clever way.

1.6.1 Markov Chain Monte Carlo

Markov Chain Monte Carlo (MCMC) is an efficient and accurate way of estimating the shape of a posterior probability distribution by drawing samples that are representative of that distribution. To use a real-world example, this is similar to the way that a well-constructed opinion poll is representative of the larger population.

There are many different MCMC algorithms, but the basics remain the same. The idea is that many combinations of model parameters are so unlikely that they contribute almost nothing to the probability distribution. An MCMC sampler is comprised of one or more "chains" that traverse through probability space using a random walk combined with a proposal algorithm that is related to the ratios of probabilities of two locations in the joint parameter space. Rather than trying all combinations of model parameters, the chains traverse in and around regions that contribute appreciably to the posterior. When the number of samples is large enough, the samples represent an accurate estimate of the true posterior (Gelman et al., 2014; McElreath, R., 2020), enabling us to make inferences about the model parameters.

1.7 Rationale, Hypothesis, and Objectives

This doctoral work consists of four studies of atmospheric circulation on hot Jupiters that address several outstanding questions from the literature.

The first study, Chapter 2, is a reanalysis of the published phase curves of WASP-43b. Despite receiving the same amount of stellar flux as HD 209458b, the planet WASP-43b seemed to transport no heat from day to night, which was not predicted by GCMs. We noticed that in the original WASP-43b phase curve paper, the authors' best-fit model was physically impossible because it required negative nightside flux. We proposed that this was due to mishandling of instrumental systematics, and that correcting the phase curves would show that the planet had a cooler dayside, and hotter nightside, than originally reported.

Zooming the lens out a bit, Chapter 3 examines nightside temperatures for twelve planets with published *Spitzer* phase curves. Hot Jupiter dayside temperatures were predicted and observed to increase proportionally to the their irradiation temperatures, but it was unknown what sort of trend the nightside temperatures would follow. The measurements are harder to make, because full-orbit phase curves are necessary. I collected published phase curves at multiple wavelengths from twelve planets at a range of irradiation temperature, and used them to infer the nightside effective temperatures for all twelve planets using Gaussian process regression. Some phase curves implied unphysical, negative nightside flux, so it was necessary to correct for this in order to obtain a robust temperature estimate. By combining phase curves at multiple wavelengths, I estimated the bolometric flux and nightside effective temperatures for twelve hot Jupiters at a range of irradiation temperatures. I fit several predictive models to the observed nightside effective temperatures in order to test predictions.

The manuscript in Chapter 4 presents an analysis of *Spitzer* phase curve observations of Qatar-1b, a planet with the same irradiation temperature as HD 209458b and WASP-43b. Because they have the same incoming stellar flux, any differences in circulation patterns between the three planets can be attributed to secondary planetary parameters like rotation rate, radius, or mass. In order to determine the eclipse depth, phase curve amplitude, and bright spot offset of Qatar-1b, I used two reduction and analysis pipelines to obtain time series photometry at 3.6 μm and 4.5 μm, and fit the data using MCMC to obtain best-fit parameters values and uncertainties. Lastly, I compared the values that I found for Qatar-1b to the published values for HD 209458b and WASP-43b to test the importance of secondary parameters on atmospheric circulation patterns.

Finally, the field of exoplanet characterization is in a transitional period. Despite not being designed for exoplanet science, *Spitzer* was used to characterize hundreds of hot Jupiters in the infrared. Next generation space telescopes like *James Webb* and *Ariel* have been designed with exoplanets in mind. *Ariel* is completely dedicated to exoplanets and will survey ∼1000 planets in the near infrared. The best way to make the most of this huge number of observations is to use Bayesian hierarchical modelling, which is a powerful and intuitive way of sharing information across disparate observations. Hierarchical models are routinely used in other fields, but have not yet been applied to exoplanet atmospheric characterization. In preparation of forthcoming exoplanet surveys, I tested hierarchical modelling on *Spitzer* data in Chapter 5. I used hierarchical models to fit a suite of ten repeated eclipse observations of the hot Jupiter XO-3b to search for dayside variability, and then to simultaneously fit 74 eclipse observations of 37 planets. This helps set the stage for surveys with *James Webb* and *Ariel*.

2 Revisiting the Energy Budget of WASP-43b: Enhanced day-night heat transport

Prologue

This Chapter presents a second look at the full-orbit phase curves of the well-studied hot Jupiter WASP-43b, by considering the planet's longitudinal brightness maps and accounting for dayside reflected light. Initially WASP-43b seemed to be an oddball because its published phase curves suggest abnormally low (negative) flux is being emitted from its nightside. Additionally, the original paper neglected reflected light in the near infrared, but this is not a safe assumption to make if the planet has an appreciable geometric Albedo. As this Chapter will show, accounting for both the unphysical negative flux and dayside reflected light has important implications for the energy budget of WASP-43b.

2.1 Abstract

The large day–night temperature contrast of WASP-43b (Stevenson et al., 2014, 2017) has so far eluded explanation (e.g., Kataria et al., 2015). We revisit the energy budget of this planet by considering the impact of reflected light on dayside measurements, and the physicality of implied nightside temperatures. Previous analyses of the infrared eclipses of WASP-43b have assumed reflected light from the planet is negligible and can be ignored. We develop a phenomenological eclipse model including reflected light and thermal emission and use it to fit published *Hubble* and *Spitzer* eclipse data. We infer a near-infrared geometric albedo of 24±1% and a cooler dayside temperature of 1483±10 K. Additionally, we perform lightcurve inversion on the three published orbital phase curves of WASP-43b and find that each suggests unphysical, negative flux on the nightside. By requiring non-negative brightnesses at all longitudes, we correct the unphysical parts of the maps and obtain a much hotter nightside effective temperature of 1076 ± 11 K. The cooler dayside and hotter nightside suggests a heat recirculation efficiency of 51% for WASP-43b, essentially the same as for HD 209458b, another hot Jupiter with nearly the same temperature. Our analysis therefore reaffirms the trend that planets with lower irradiation temperatures have more efficient day-night heat transport. Moreover, we note that 1) reflected light may be significant for many near-IR eclipse measurements of hot Jupiters, and 2) phase curves should be fit with physically possible longitudinal brightness profiles — it is insufficient to only require that the disk-integrated lightcurve be non-negative.

2.2 Introduction

In many ways, the hot Jupiter WASP-43b (Hellier et al., 2011) is like other planets of this classification. It has a radius of 1.036 ± 0.019 $R_{\rm J}$, a mass of 2.034 ± 0.052 $M_{\rm J}$, and an orbital period of 0.81 days (Gillon et al., 2012). However, unlike other hot Jupiters, it orbits a fairly cool K7V star. Secondary eclipses of WASP-43b have been observed in multiple photometric bands (Wang et al., 2013; Blecic et al., 2014; Chen et al., 2014; Zhou et al., 2014). Full orbit phase curves from Hubble Space Telescope Wide Field Camera 3 (WFC3) using the G141 grism (1.1–1.7 μm), and *Spitzer* Infrared Array Camera (IRAC) at 3.6 and 4.5 μm, were used to retrieve phase resolved emission spectra (Stevenson et al., 2014, 2017). Emission and transmission spectroscopy measurements with WFC3 were used by Stevenson et al. (2014) to determine the precise amount of water in the atmosphere of WASP-43b. The planet's transit times are consistent with a constant period and show no evidence of orbital decay (Hoyer et al., 2016).

Previous analyses of WASP-43b reported an eastward hotspot offset that is typical of hot Jupiters and almost nonexistent heat transport from dayside to nightside (Stevenson et al., 2014; Schwartz and Cowan, 2015; Schwartz et al., 2017). The three-dimensional atmospheric circulation models of Kataria et al. (2015) were able to provide a good match to the WFC3 dayside emission spectrum and were able to reproduce the eastward offset by invoking equatorial superrotation. The model nightside, however, was too bright (hot) compared to the low measured nightside flux. Nightside clouds have been postulated as a way to explain the low measured nightside flux (Kataria et al., 2015; Stevenson et al., 2017). Clouds or not, if the observations are taken at face value, then WASP-43b does a poor job of moving heat from day to night. This is in stark contrast to theoretical expectations and empirical trends, both of which favor increasing day–night temperature contrast with increasing irradiation (Cowan and Agol, 2011a; Perez-Becker and Showman, 2013; Schwartz and Cowan, 2015; Komacek and Showman, 2016).

All analyses of HST/WFC3 1.1–1.7 μm exoplanet secondary eclipses have assumed that the reflected light component in this bandpass is negligible compared to the thermal emission component. López-Morales and Seager (2007) showed that thermal emission dominates reflected light for highly irradiated hot Jupiters with low Bond albedo and inefficient heat redistribution. Previous studies have found that most hot Jupiters have very low geometric albedos at optical wavelengths (Rowe et al., 2008; Kipping and Spiegel, 2011; Heng and Demory, 2013; Dai et al., 2017) and it has since been taken for granted that reflected light is also negligible in the near infrared. However, López-Morales and Seager (2007) also showed that for planets with efficient heat redistribution and Bond albedo of 50%, reflected light can instead dominate thermal emission in the near infrared. Schwartz and Cowan (2015) found a systematic offset between Bond albedos inferred from thermal phase variations and geometric albedos obtained from visible light measurements; they suggested that hot Jupiters may reflect 30–50% of incident near-infrared radiation.

If a hot Jupiter reflects light at a given wavelength, then the eclipse depth will be greater, and one will infer too high a dayside temperature if the reflected light is ignored. Since total bolometric flux is proportional to the fourth power of temperature, even a small change in temperature leads to a significant change in bolometric flux.

With the notable exception of the earliest high-cadence phase curve measurements (Knutson et al., 2007, 2009), exoplanet researchers have been content to publish phase curve parameters without worrying about the particular brightness distribution that could give rise to such a lightcurve (Cowan and Agol, 2008). Instead, theorists have taken the extra step of producing mock observations, which can be compared to the real thing. In the few cases where theory and the observations have not matched up, it has been attributed to missing physics in the models, rather than unphysical phase curves.

In Section 2 of this letter, we revisit the dayside measurements, accounting for reflected light to obtain a new dayside effective temperature for WASP-43b. In Section 3, we revisit the nightside measurements, correcting for negative brightnesses at certain longitudes, to obtain a new nightside effective temperature. In Section 4, we use these two new effective temperatures to re-estimate the Bond albedo and heat recirculation efficiency for WASP-43b, and we discuss the implications for that planet as well as other hot Jupiters.

2.3 Thermal Plus Reflected Eclipse Model

Immediately before and after a secondary eclipse, the flux we observe from a planet is some combination of reflected starlight and thermal emission

$$\frac{F_{\rm day}}{F_*} = A_g \left(\frac{R_p}{a}\right)^2 + \frac{B_\lambda(T_{\rm day})}{B_\lambda(T_*)} \left(\frac{R_p}{R_*}\right)^2 \tag{2.1}$$

(Cowan et al., 2007). The eclipse depth, F_{day}/F_*, is the ratio of the planet's dayside flux to the stellar flux at a particular wavelength. The star's brightness temperature at this wavelength is T_*, and T_{day} is the planet's dayside brightness temperature at that wavelength. The geometric albedo, A_g, is the fraction of starlight that the planet reflects back toward the star (and hence the observer), and is also wavelength dependent. The planetary and stellar radii are given by R_p and R_* respectively, and a is the semimajor axis of the planet's orbit.

Given an eclipse depth, the geometric albedo and dayside brightness temperature are inversely related, as can be seen in Figure 2.1. For the *Spitzer*/IRAC 3.6 and 4.5 μm channels, thermal emission dominates and the reflected light term can be ignored. Even a geometric albedo in excess of unity can only account for a small fraction of the measured flux. For the HST/WFC3 1.1–1.7 μm wavelengths, the reflected light component is usually also neglected. However as Figure 2.1 shows, the WFC3 eclipse depths can be attributed solely to reflected light for even modest values of geometric albedo — in this case $\sim 40\%$, which is consistent with estimates of Bond albedos for hot Jupiters (Schwartz and Cowan, 2015), and theoretical predictions of geometric albedo for very hot planets (Sudarsky et al., 2000).

In general, we expect different brightness temperatures at different wavelengths as they should probe different depths in the atmosphere. However, Figure 1 of Schwartz and Cowan (2015) shows that the aggregate broadband brightness temperature spectrum of 50 hot Jupiters is flat and featureless. They attributed this to a vertically isothermal atmosphere, optically thick clouds, or both. Even without clouds, the band-integrated infrared dayside brightness temperatures of hot Jupiters are predicted to be within $\sim$100 K of the dayside effective temperature; using brightness temperatures in three broadbands to estimate the dayside effective temperatures for these planets should only introduce a systematic error of 4–5% (Cowan and Agol, 2011a). For our analysis we treat the dayside atmosphere of WASP-43b as isothermal and fit its emission with a blackbody.

We use the model of reflected light plus thermal emission from eq. (2.1) to fit the published secondary eclipse depths of WASP-43b from HST/WFC3 and *Spitzer*/IRAC

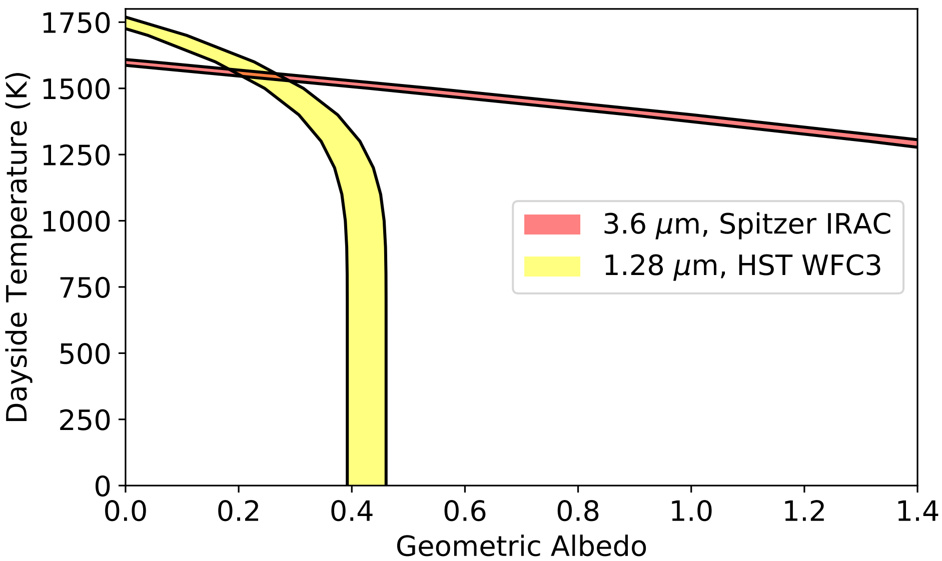

Figure 2.1: Degeneracy between thermal emission and reflected light for WASP-43b. The 1σ constraints from two published eclipse depths are shown. When $A_g = 0$, only thermal emission contributes to the eclipse depth. As A_g is increased, the amount of thermal emission decreases, and consequently so does $T_{\rm day}$. Only two wavelengths are shown here for clarity, but the following trend holds: the *Spitzer* IRAC eclipse depth lines never touch the horizontal axis for physically possible values of geometric albedo, meaning *Spitzer* measurements require thermal emission regardless of the value of A_g. For the HST/WFC3 measurements, the eclipse depths can be attributed solely to reflected light if the geometric albedo is $\sim 40\%$. It may not be safe to ignore reflected light in the HST/WFC3 1.1–1.7 μm bandpass.

(Stevenson et al., 2014, 2017); schematically, this is simply where the swaths intersect in Figure 2.1, but incorporating all of the eclipse depths. We used a Phoenix stellar model for the spectrum of the host star (Allard et al., 2000). A gray reflectance was assumed, meaning a constant albedo for all wavelengths (in practice this should be taken to be the albedo in the WFC3 bandpass). We follow the lead of Stevenson et al. (2017) and fit only the WFC3 and *Spitzer* data. Unsurprisingly, our model is also a bad fit to the ground-based photometric data (see Table 2.1). We omit data in the water band (1.35–1.6 μm) from our fit.[1] Using a Markov Chain Monte Carlo (Foreman-Mackey et al., 2013), we fit for the planet's geometric albedo and the dayside temperature. We find $A_g = 0.24 \pm 0.01$ and $T_{\rm day} = 1483 \pm 10$ K. A thermal-only model, with dayside temperature as the only

[1] We get a good match to data in the H_2O band between 1.35–1.6 μm by fitting the characteristic water feature from Iyer et al. (2016). However, the fitting is completely empirical and provides no additional information about the atmosphere of WASP-43b.

Table 2.1: Fit statistics for different combinations of eclipse depth data. We adopt the parameters from the fit that omits the water band, and incorporates only WFC3 and *Spitzer* data, in order to be consistent with Stevenson et al. (2017).

Data Used	Model	$T_{\rm day}$ (K)	A_g	$N_{\rm params}$	$N_{\rm data}$	χ^2	χ^2/Datum	BIC
WFC3, *Spitzer*, no water band	**Thermal + Reflected**	1483 ± 10	0.24 ± 0.01	2	9	**53**	5.9	**58**
WFC3, *Spitzer*, no water band	Thermal Only	1575 ± 7		1	9	333	37	335
All, no water band	**Thermal + Reflected**	1331 ± 482	0.36 ± 0.18	2	22	**332**	20	**337**
All, no water band	Thermal Only	1728 ± 163		1	22	614	47	616

parameter, yields $T_{\rm day} = 1575 \pm 7$ K. The Bayesian Information Criterion (BIC; Schwarz, 1978) is much lower for the reflected plus thermal model than the thermal-only model (Δ BIC = 277), meaning we can strongly reject the thermal-only model in favor of the model with reflected light. Our fits are summarized in Table 2.1.

Omitting the water band data means we are unable to directly compare Δ BIC between our toy model and the 6-parameter spectral retrieval of Stevenson et al. (2017). A full atmospheric retrieval, with the addition of reflected light, may be necessary for a statistically and physically complete model of WASP-43b's dayside. A comprehensive understanding of the dayside of WASP-43b should also address why the ground-based data disagree with the models.

2.4 Revisiting the phase variations of WASP-43b

Since WASP-43b is on a circular, edge-on orbit and expected to be tidally locked, we can use Equation 7 from Cowan and Agol (2008) to invert the phase curves, $F(\xi)$, into longitudinally resolved brightness maps, $J(\phi)$, where ξ is the planet's phase angle ($\xi = 0$ at secondary eclipse, $\xi = \pi$ at transit), and ϕ is longitude from the substellar point (where $-\pi/2 < \phi < \pi/2$ is the dayside of the planet). Since the phase curves were each fit using the fundamental frequency and its first harmonic (one and two cycles per orbit, respectively), the corresponding brightness maps also have two sinusoidal frequencies. Higher frequencies in the map are assumed to be zero, following Cowan and Agol (2008). As can be seen in Figure 2.3, all three published phase curves require certain longitudes on the nightside of WASP-43b to have negative brightness, which is physically impossible. To properly estimate the nightside temperature of this planet, we require a map with

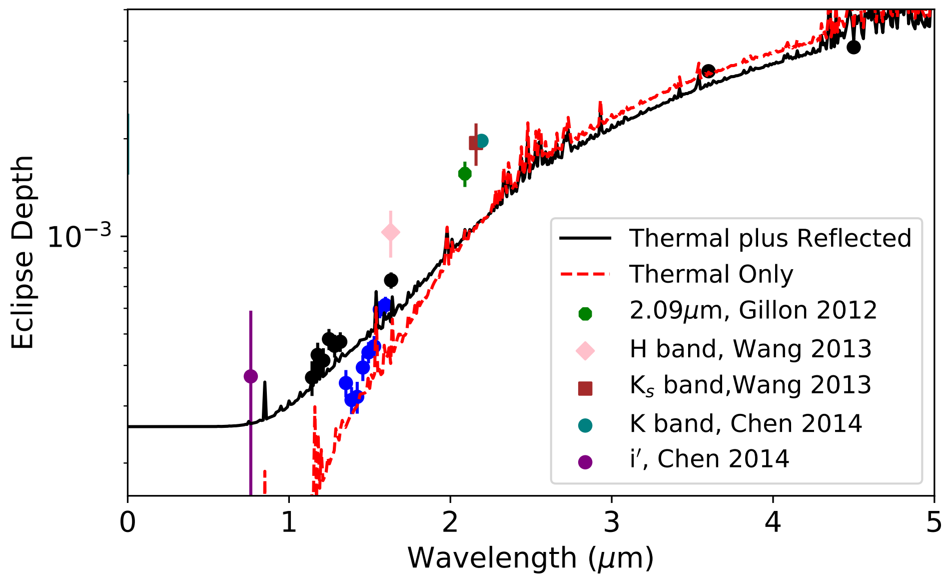

Figure 2.2: WFC3 and *Spitzer* IRAC eclipse depths fit with the two different toy models. The black points are the WFC3 and *Spitzer* points. The water band points (in blue) are omitted from the fits. Photometric eclipse depths in different bands are shown but are also not incorporated in the fits, following (Stevenson et al., 2014). The reflected light plus thermal emission model is preferred over the thermal-only model ($\Delta BIC = 277$).

non-negative brightness values at all longitudes.

For each brightness map, $J(\phi)$, we keep the map as-is but set the negative brightnesses to zero. We then compute the phase curve for this doctored map using (Cowan and Agol, 2008):

$$F(\xi) = \int_{-\xi-\frac{\pi}{2}}^{-\xi+\frac{\pi}{2}} J(\phi)\cos(\phi+\xi)\mathrm{d}\phi. \tag{2.2}$$

Evaluating this phase curve at $\xi = \pi$ gives the ratio of disk-integrated nightside flux to stellar flux, F_{night}. We then calculate a nightside brightness temperature at each wavelength using

$$T_b(\lambda) = \frac{hc}{\lambda k}\left[\ln\left(1 + \frac{e^{hc/\lambda k T_*} - 1}{F_{\mathrm{night}}/\delta_{\mathrm{tra}}}\right)\right]^{-1}, \tag{2.3}$$

where $\delta_{\mathrm{tra}} = (R_p/R_\star)^2$ is the transit depth. For the brightness temperature of the star at a given wavelength, $T_\star$, we use Phoenix stellar grid models. Applying this technique to the three published phase curves, we obtain nightside brightness temperatures of 1173 ± 12 K, 697 ± 55 K, and 706 ± 26 K, for the WFC3 and *Spitzer* 3.6 and 4.5 μm observations, respectively. The uncertainties were estimated using a 10^5 step Monte Carlo.

We compute the error weighted mean of the brightness temperatures to estimate an average nightside temperature and propagate uncertainties via Monte Carlo. We obtain a value of $T_{\rm n} = 1076 \pm 11$ K, much higher than the previous value 254 ± 182 K, estimated by Schwartz and Cowan (2017), who also used the error weighted mean and propagated uncertainties via Monte Carlo. The new nightside temperature is significantly higher than the previous value ($> 4\sigma$ discrepant).

If our updated brightness temperatures are taken at face value, then the nightside of WASP-43b bears a striking resemblance to the predicted emission spectrum of an isolated brown dwarf with an effective temperature of 600 K (Morley et al., 2012). It must be noted, however, that while setting certain longitudes on a planet's brightness map to zero is better than having negative values, it is still unrealistic. Even neglecting irradiation, hot Jupiters are predicted to have a remnant heat of formation of 50–75 K (Burrows et al., 2006). Our nightside brightness temperatures and effective temperature are probably best thought of as lower limits.

2.5 Discussion & Conclusions

Using our dayside and nightside temperature estimates, we can infer the planet's Bond albedo, $A_{\rm B}$, and heat recirculation efficiency, ε, using the equations from Cowan and Agol (2011a),

$$T_{\rm d} = T_0 (1 - A_B)^{1/4} \left(\frac{2}{3} - \frac{5}{12}\varepsilon \right)^{1/4}, \tag{2.4}$$

$$T_{\rm n} = T_0 (1 - A_B)^{1/4} \left(\frac{\varepsilon}{4} \right)^{1/4}, \tag{2.5}$$

where $T_0 \equiv T_\star \sqrt{R_\star / a}$ is the planet's irradiation temperature. Both $A_{\rm B}$ and ε range from 0 to 1.

We use a 10^5 step MCMC to propagate uncertainties and find $A_{\rm B} = 0.3 \pm 0.1$ and $\varepsilon = 0.51 \pm 0.08$. We plot the 1σ contour in the $A_{\rm B}$–ε plane in Figure 2.4. The Bond albedo and heat recirculation efficiency were previously found to be $A_B = 0.36^{+0.11}_{-0.12}$ and

$\varepsilon = 0.01^{+0.01}_{-0.01}$ (Schwartz et al., 2017), while Stevenson et al. (2017) reported $A_B = 0.19^{+0.08}_{-0.09}$ and $\varepsilon = 0.002^{+0.01}_{-0.002}$.[2] Our revised estimate of the Bond albedo is consistent with previous estimates, and indeed with the NIR geometric albedo we inferred above (this may be a coincidence, as only a small fraction of the incident stellar flux is in the WFC3 band). Our heat transport efficiency, on the other hand, is much greater than previously reported.

By demanding physically possible brightness maps, our estimate of the planet's energy budget has changed dramatically. Our updated energy budget puts WASP-43b in the same part of A_{B}–ε parameter space as HD 209458b, and in line with the trend that planets with lower irradiation temperatures have higher heat recirculation (WASP-43b and HD209485b have similar irradiation temperatures). In other words, WASP-43b is no longer an outlier with inexplicably low day-night heat transport. The models of Kataria et al. (2015) may not be missing crucial physics after all.

Doctoring the brightness maps of WASP-43b is the best one can do without completely refitting the phase curves. For best results, the condition of non-negative brightness maps should be used as a constraint when fitting phase curve parameters simultaneously with astrophysical and detector noise sources.

Additionally, we have found that reflected light matters in the near infrared for WASP-43b, and by extension for other hot Jupiters. Previous estimates of the dayside temperature of WASP-43b were probably too high, because reflected light may make up a significant portion of the light measured in the WFC3 1.1–1.7 μm bandpass. Reflected light has been neglected for all other planets with WFC3 dayside emission spectra, including TrES-3b, WASP-4b, WASP-12b, WASP-33b, WASP-103b CoRoT-2b, HD 189733b, and HD 209458b — these planets may also exhibit reflected light in the near infrared, and merit a second look.

2.6 Acknowledgments

The authors acknowledge support from the McGill Space Institute and l'Institut de recherche sur les exoplanètes. D. K. is supported by a Technologies for Exo-Planetary

[2] We convert their reported $\mathcal{F}$ to ε using algebra.

Science fellowship, and a Centre de recherche en astrophysique du Québec fellowship. Thanks to Aisha Iyer for providing the representative water band transmission spectrum, and to Joel Schwartz for providing a table of published planetary phase curve parameters. Thanks to James Xu for helping with the effective temperature estimate. Thanks to Jacob Bean, Taylor Bell, Laura Kreidberg, and Caroline Morley for helpful feedback on the manuscript.

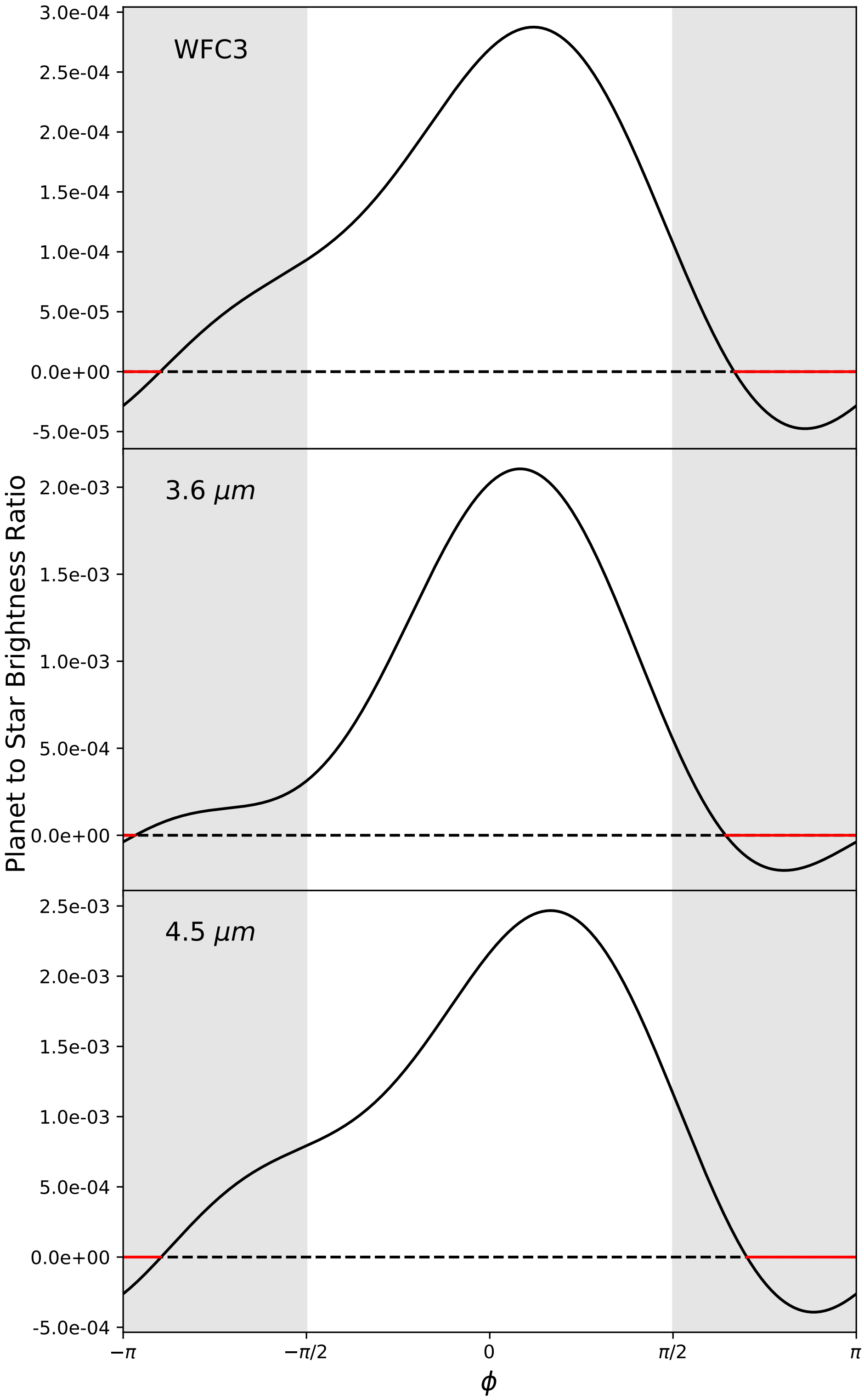

Figure 2.3: Brightness maps corresponding to the three full orbit phase curves of WASP-43b (Stevenson et al., 2014, 2017). Here ϕ is the longitude from the substellar point and the nightside of the planet is shown as the grey shaded area. All three phase curves require negative brightnesses at certain longitudes, which is unphysical. The red line shows where we doctor the maps by setting the brightness to zero.

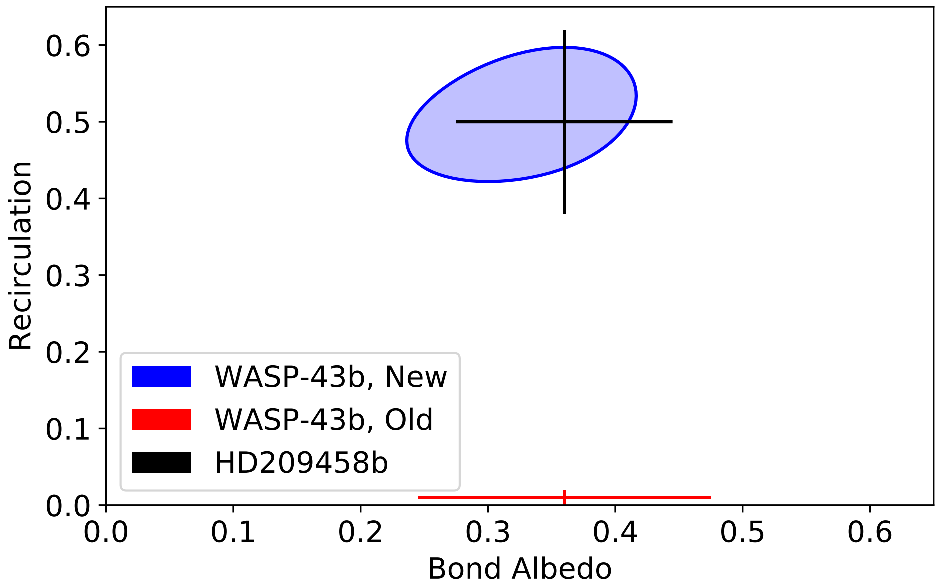

Figure 2.4: Energy budget of WASP-43b. The blue region is the 1σ contour after our reanalysis. We also plot the best fit values and uncertainties for WASP-43b before correcting the brightness maps and for HD 209458b, both from Stevenson et al. (2017). WASP-43b no longer hugs the bottom of the plot after our reanalysis, but is now similar to HD 209458b, which we would expect given the similar irradiation temperatures of the two planets (Cowan and Agol, 2011a; Perez-Becker and Showman, 2013; Schwartz and Cowan, 2015; Komacek and Showman, 2016).

Epilogue

Since the publication of the manuscript in this Chapter, there have been several reanalyses of the WASP-43b observations. Louden and Kreidberg (2018) refit the WFC3 phase curve, and found a hot nightside brightness temperature of 1290 ± 39 K. They also found that including a simple reflected light model decreased their dayside temperature by several hundred degrees.

The *Spitzer* phase curves have been rereduced and reanalyzed in four different papers (Mendonça et al., 2018; Morello et al., 2019; May and Stevenson, 2020; Bell et al., 2020). Their nightside brightness temperature estimates were 914 ± 75 K, 730 ± 97K, 838 ± 65 K, and 640 ± 105 K respectively. Our estimate of 1076 ± 11 K was higher, most likely due to the more simplified treatment we used. Regardless, all reanalyses agree that the planet does in fact transport heat from day to night.

Three of the analyses suggest that WASP-43b transports heat from day to night less efficiently than HD 209458b, which has the same irradiation temperature but a longer rotational period and smaller surface gravity. Chapter 4 presents an analysis of a third planet with the same irradiation temperature: Qatar-1b. For now, the next chapter will examine nightside temperatures for a suite of hot Jupiters with different irradiation temperatures.

3 Uniformly hot nightside temperatures on short-period gas giants

3.1 Prologue

This chapter describes a study of the nightside temperatures on twelve hot Jupiters using their published near-infrared phase curves. I performed a meta-analysis of multiple phase curve papers from different authors, using the published phase curve results and parameters for each planet. It turns out that WASP-43b was not the only planet with problematic phase curves— the planets WASP-14b and HAT-P-7b also had 3.6 μm phase curves with negative nightside flux, which makes it impossible to estimate their nightside effective temperature properly. Building on the work in the previous Chapter, I implemented two methods to correct for unphysical maps, and combined nightside brightness temperatures at multiple wavelengths to estimate nightside effective temperatures for each planet using Gaussian process regression (Pass et al., 2019).

3.2 Abstract

Short-period gas giants (hot Jupiters) on circular orbits are expected to be tidally locked into synchronous rotation, with permanent daysides that face their host stars, and permanent nightsides that face the darkness of space (Showman and Guillot, 2002). Thermal flux from the nightside of several hot Jupiters has been measured, meaning energy is transported from day to night in some fashion. However, it is not clear exactly what the physical information from these detections reveals about the atmospheric dynamics of hot Jupiters. Here we show that the nightside effective temperatures of a sample of 12 hot Jupiters are clustered around 1100 K, with a slight upward trend as a function of stellar irradiation. The clustering is not predicted by cloud-free atmospheric circulation models (Komacek et al., 2017; Komacek and Tan, 2018; Zhang and Showman, 2017). This result can be explained if most hot Jupiters have nightside clouds that are optically thick to outgoing longwave radiation and hence radiate at the cloud-top temperature, and progressively disperse for planets receiving greater incident flux. Phase curve observations at a greater range of wavelengths are crucial to determining the extent of cloud coverage, as well as the cloud composition on hot Jupiter nightsides (Morley et al., 2017; Tinetti et al., 2018).

3.3 Main Text

We collected published full orbit, infrared phase curves for twelve hot Jupiters: CoRoT-2b (Dang et al., 2018), HAT-P-7-b (Wong et al., 2016), HD 149026b (Zhang et al., 2018), HD 189733b (Knutson et al., 2012), HD 209458b (Zellem et al., 2014), WASP-12b (Cowan et al., 2012), WASP-14b (Wong et al., 2015), WASP-18b (Maxted et al., 2013), WASP-19b (Wong et al., 2016), WASP-33b (Zhang et al., 2018), WASP-43b (Stevenson et al., 2014, 2017; Mendonça et al., 2018; Louden and Kreidberg, 2018), and WASP-103b (Kreidberg et al., 2018). We also included the brown dwarf KELT-1b (Beatty et al., 2019). We calculated the nightside brightness temperatures from the phase curve parameters, and used Gaussian Process regression to estimate each planet's bolometric flux, and subsequently its disk-integrated nightside effective temperature. Several of the published phase curve fits imply negative nightside disk-integrated flux, which is unphysical, because it implies that the planets have negative brightness at some longitudes on their surface. We explain how we handled these cases in the Methods section. Future phase curve observations should be fit with the constraint that flux is non-negative everywhere on the planet. We also inferred nightside temperatures by considering and modifying negative brightness maps, which is similar in spirit to demanding positive phase curves and brightness maps when fitting the data. The mapping approach yielded a nightside temperature trend consistent with that of the disk-integrated approach.

In Figure 3.1 we show the dayside and nightside effective temperatures plotted against the stellar irradiation temperature, $T_0 \equiv T_\star\sqrt{R_\star/a}$, were $T_\star$ is the stellar effective temperature, $R_\star$ is the stellar radius, and a is semi-major axis. The nightside temperatures are all around 1100K and exhibit a slight upward trend with stellar irradiation. We tabulate the dayside temperature, nightside temperature, Bond Albedo, and heat recirculation efficiency for each planet in Table 3.1. While this paper was under review, a similarly flat trend for nightside brightness temperature was reported (Beatty et al., 2019).

Various theories have suggested that reradiation (Showman and Guillot, 2002), advection, wave propagation (Komacek and Showman, 2016), molecular dissocation (Bell and Cowan, 2018), coriolis forces, and magnetic drag could all play a role in atmospheric circulation on hot Jupiters. Models predict that the amount of day-night heat recirculation depends sensitively on planetary properties and the amount of stellar irradiation each planet receives, which vary between individual hot Jupiters (Komacek et al., 2017; Komacek and Tan, 2018; Zhang and Showman, 2017).

We fit the nightside temperatures using two models of atmospheric heat transport. The qualitative behaviour of each model is shown in Figures 3.8 and 3.9. The first model is a semi-analytic energy balance model incorporating atmospheric radiation and advection (Cowan and Agol, 2011b), and predicts nightside temperatures given the planetary and stellar properties. We fit for two parameters: a common wind velocity, and P/g, where the latter quantity is the mass per unit area of the active layer of the atmosphere, that is, the layer that responds to instellation. The model was updated recently to include the effects of hydrogen dissociation and recombination, by solving the Saha equation to determine the amount of hydrogen dissociated at a given atmospheric temperature and the resulting heat sinks/sources (Bell and Cowan, 2018). Hydrogen dissociation and recombination is predicted to significantly increase heat transport in ultra-hot Jupiters (Bell and Cowan, 2018; Komacek and Tan, 2018).

The second model is an analytic, dynamical model incorporating radiation, advection, magnetic drag, coriolis forces, and gravity waves (Komacek and Showman, 2016). This model predicts—rather than prescribes—the wind velocities for each hot Jupiter, and was shown to qualitatively match predictions of day-night temperature contrast from general circulation models. The model was recently updated to include the effects of hydrogen dissociation, albeit in a greatly simplified form (Komacek and Tan, 2018). As the magnetic field strengths of hot Jupiters are unknown to orders of magnitude (Yadav and Thorngren, 2017), we chose to neglect magnetic drag, but note that magnetic drag can potentially depress day-night heat transport for planets with very strong magnetic fields (~ 100 G). We fit for a universal P/g, hence this model has only one fit parameter.

For each model fit, we performed a grid search in parameter space to find the parameters that minimize χ^2. Models that allow for hydrogen dissociation provide better fits to the data than those without, even though this does not increase the number of parameters. The best fit model predictions can be seen in Figure 3.2. The semi-analytic energy balance model incorporating hydrogen dissociation yielded the best fit of all the models we considered. In the context of the energy balance model, the trend in observed nightside temperatures suggests that all hot Jupiters have similar wind velocities, contrary to predictions.

Alternatively, dynamical predictions may be correct, but ultimately overshadowed by optically thick nightside clouds. Clouds are predicted to be present on the nightsides of all hot Jupiters (Parmentier et al., 2016; Powell et al., 2018; Roman and Rauscher, 2019), but the cloud composition depends on the temperature, pressure, and cloud formation physics. Observationally, nightside clouds have been previously invoked to explain nondetections of nightside flux (Kataria et al., 2015; Wong et al., 2015; Stevenson et al., 2017). The nightside temperature trend – or lack thereof – implies that the hot Jupiters in our study all have nightside clouds that emit at similar temperatures. Vertical mixing sets the cloud top pressure, so in principle we could be seeing cloud tops from different cloud species that all happen to have similar vertical cloud-top temperatures.

A simpler explanation is that hot Jupiters all have the same species of nightside clouds, which condense at a similar cloud-base temperature. The emitting temperature corresponds to the cloud-top temperature, which would be slightly cooler than the condensation temperature. These clouds would emit thermal radiation around the same effective temperature, and block outgoing longwave radiation from below, requiring clouds with large grains. Potential cloud species include manganese sulfide or silicate clouds, based on condensation curves (Parmentier et al., 2016). As we show in Figure 3.3, the nightside infrared colours are roughly isothermal. The similarity of the brightness temperature between *Spitzer* bandpasses implies that they are probing parts of the atmosphere with similar temperatures, consistent with optically thick clouds.

Incorporating radiative feedback and detailed cloud microphysics is computationally intensive, which is the reason many studies have used cloud-free general circulation models, and post-processed clouds afterwards using the resulting temperature-pressure profiles and cloud condensation curves. However, post-processing of exoplanet clouds can lead to different predictions of cloud coverage, phase offsets, and day-night temperature contrasts than more intricate models (Roman and Rauscher, 2019; Powell et al., 2018). Fully three-dimensional models incorporating realistic cloud physics and heat transport due to hydrogen chemistry are clearly needed in order to properly understand hot Jupiters spanning the full range of irradiation temperatures. Realistic treatments of magnetic effects may be necessary for the hottest planets (Arcangeli et al., 2019; Yadav and Thorngren, 2017). On the observational front, spectroscopic phase curve observations at longer wavelengths (Morley et al., 2017), with the Mid-Infrared Instrument onboard the *James Webb Space Telescope*(Bean et al., 2018), and with the *Atmospheric Remote-sensing Infrared Exoplanet Large-survey*(Tinetti et al., 2018), will make it possible to characterize the

Table 3.1: Dayside temperatures, nightside temperatures, and energy budget parameters for twelve hot Jupiters. We also include the brown dwarf KELT-1b. Our heat recirculation parameter, ε, ranges from 0, for no day-night heat recirculation, to 1, for perfect day-night heat recirculation (Cowan and Agol, 2011a). A_{B} is the Bond Albedo.

	T_0 K	T_{day} K	T_{night} K	A_B	ε
HD 189733b	1636±14	1279±68	979±58	$0.16^{0.11}_{0.1}$	$0.59^{0.12}_{0.11}$
WASP-43b	2051±53	1664±69	984±67	$0.22^{0.13}_{0.12}$	$0.27^{0.07}_{0.07}$
HD 209458b	2053±38	1393±70	1015±86	$0.52^{0.08}_{0.09}$	$0.51^{0.15}_{0.13}$
CoRoT-2b	2175±47	1631±67	792±64	$0.48^{0.09}_{0.1}$	$0.13^{0.05}_{0.04}$
HD 149026b	2411±59	1883±106	1098±201	$0.33^{0.14}_{0.15}$	$0.25^{0.18}_{0.13}$
WASP-14b	2654±43	2351±142	1267±111	$0.12^{0.14}_{0.08}$	$0.22^{0.09}_{0.06}$
WASP-19b	2995±52	2181±133	986±233	$0.54^{0.1}_{0.12}$	$0.1^{0.12}_{0.07}$
HAT-P-7b	3211±75	2678±158	1507±285	$0.21^{0.16}_{0.14}$	$0.22^{0.17}_{0.12}$
KELT-1b	3391±29	2922±132	1128±108	$0.18^{0.12}_{0.11}$	$0.06^{0.03}_{0.02}$
WASP-18b	3412±49	2894±206	815±463	$0.26^{0.17}_{0.15}$	$0.01^{0.07}_{0.01}$
WASP-103b	3530±99	2864±122	1528±108	$0.27^{0.12}_{0.14}$	$0.19^{0.06}_{0.05}$
WASP-12b	3636±121	2630±258	1256±386	$0.53^{0.16}_{0.2}$	$0.13^{0.23}_{0.1}$
WASP-33b	3874±104	3101±206	1776±165	$0.28^{0.16}_{0.16}$	$0.25^{0.11}_{0.08}$

dominant cloud species on hot Jupiter nightsides.

3.4 Acknowledgements

The authors thank Taylor Bell for providing the updated energy balance model code, Tad Komacek for providing his analytic day-night temperature difference code, and to Laura Kreidberg for an early look at her WASP-103b phase curve paper. Thanks to João Mendonça for providing the phase curve parameters from his WASP-43b paper. Thanks to Emily Pass for an early look at her Gaussian process temperature estimate results. Thanks to Jacob Bean and Vivien Parmentier for helpful discussion and comments about the manuscript.

3.5 Author Information

3.5.1 Contributions

D.K. led the data analysis, and wrote the manuscript. N.B.C. discussed ideas and contributed to writing the manuscript. L.D. provided the *Spitzer* data analysis pipeline and helped with reducing *Spitzer* phase curves.

3.5.2 Corresponding author

Correspondence and requests for materials should be addressed to Dylan Keating (dylan.keating@mail.mcgill.ca).

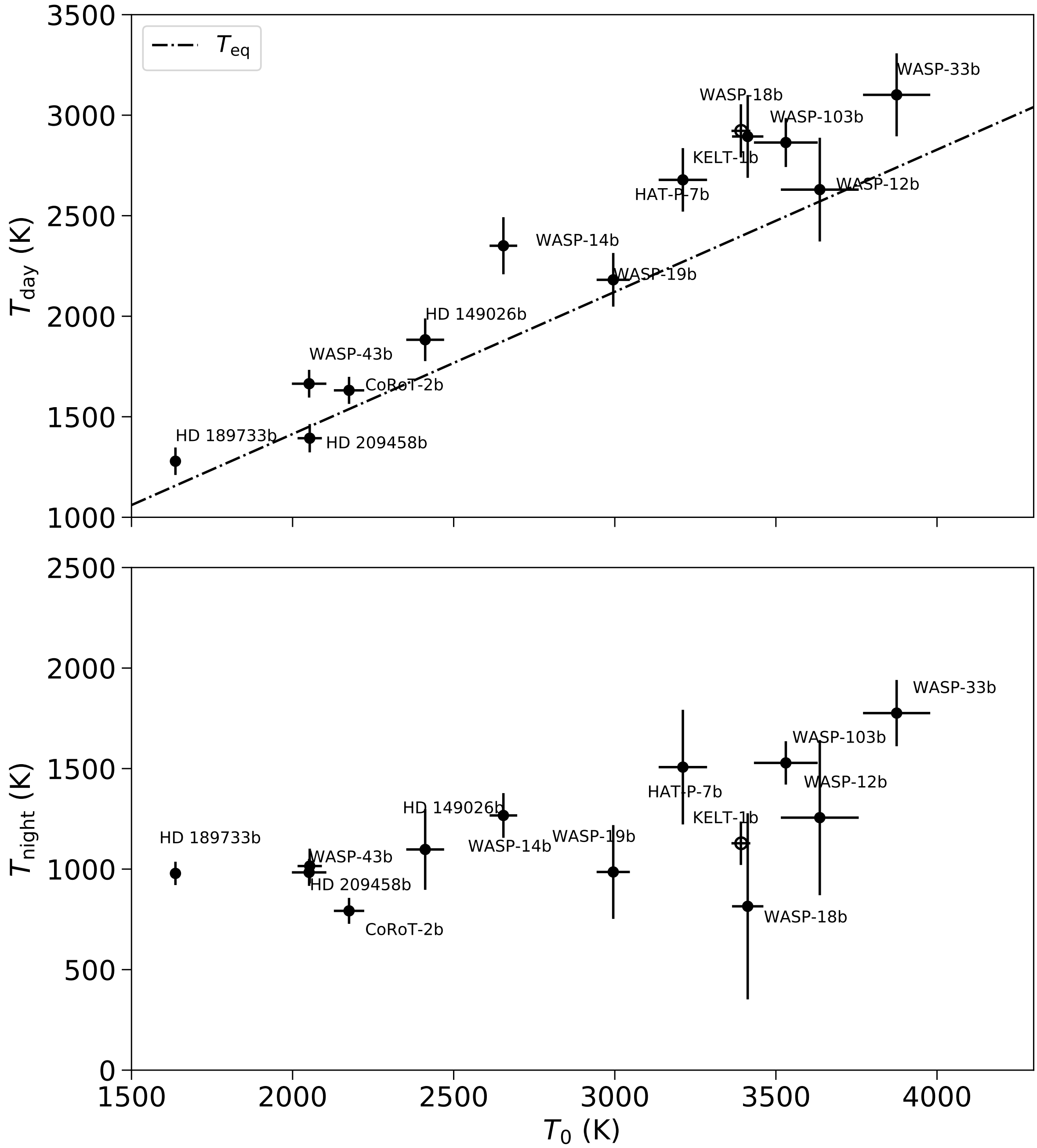

Figure 3.1: Dayside and nightside effective temperatures for twelve hot Jupiters, and one brown dwarf (KELT-1b). *Top panel:* Dayside temperatures for the hot Jupiters in our analysis are proportional to the planets' irradiation temperatures, $T_0 \equiv T_\star\sqrt{R_\star/a}$, where $T_\star$ is the stellar effective temperature, $R_\star$ is the stellar radius, and a is semi-major axis. The error bars correspond to the 1σ confidence intervals. To guide the eye, we plot the equilibrium temperature $T_{eq} \equiv (1/4)^{1/4}T_0$. *Bottom panel:* Nightside effective temperatures. The error bars correspond to the 1σ confidence intervals. Nightside temperatures are all around 1100K with a slight upward trend.

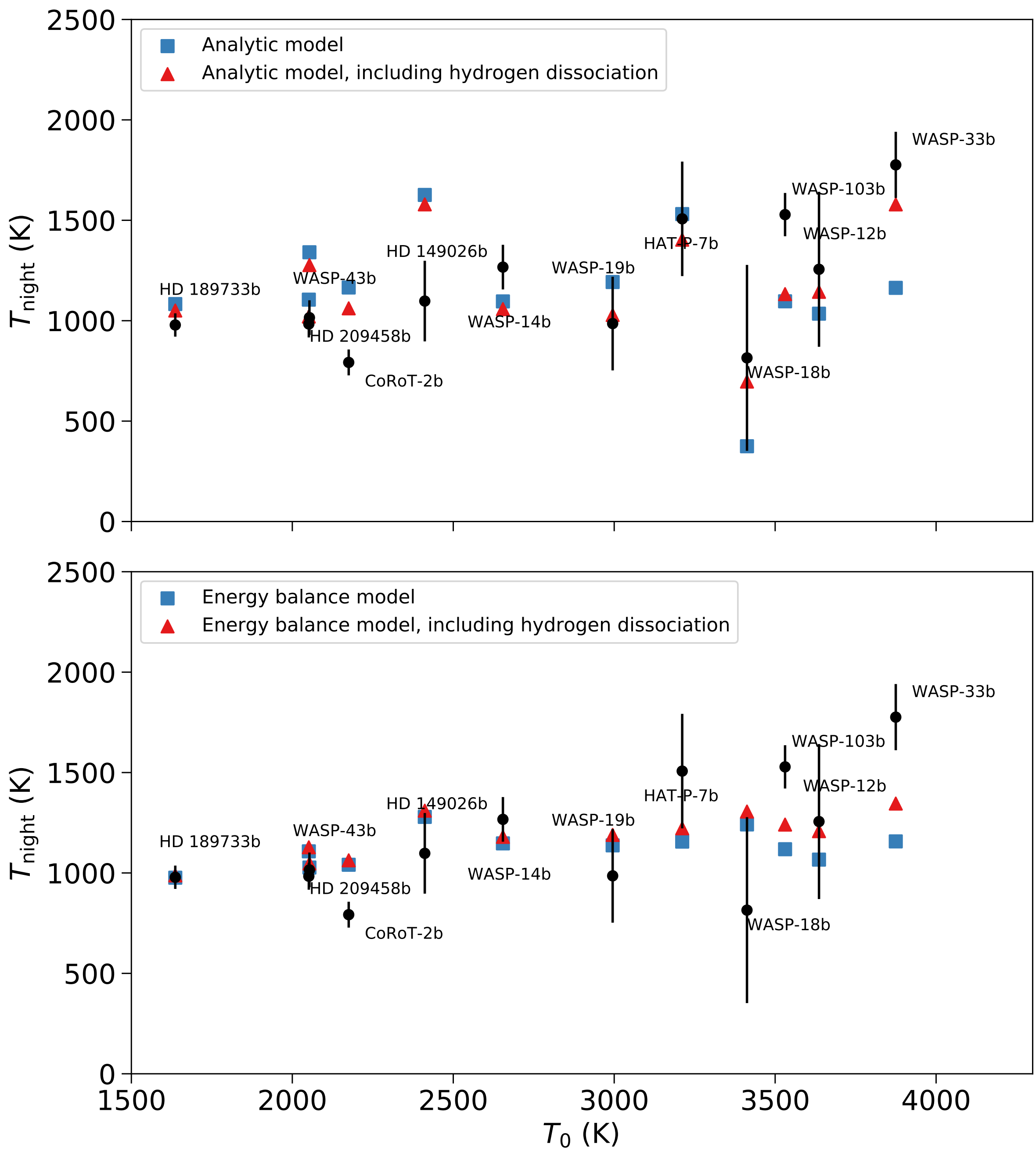

Figure 3.2: Best-fit models for the nightside temperatures of twelve hot Jupiters. *Top panel:* Best fit analytic, dynamical models (Komacek and Showman, 2016; Komacek and Tan, 2018; Zhang and Showman, 2017). The error bars correspond to the 1σ confidence intervals. The model including hydrogen dissociation is a much better fit (χ^2/datum = 4.5) than the model without (χ^2/datum = 8.5), but in both cases the model predicts greater planet-to-planet variance due to differences in predicted wind speeds. The wind speed depends on the gravity wave propagation timescale, which itself depends on the radius and mass of a planet. Differences in radius, mass, and rotation rate of these planets lead to variance in the predicted nightside temperatures. *Bottom panel:* Best fit semi-analytic energy balance models, using a common wind speed for all twelve planets (Cowan and Agol, 2011a; Bell and Cowan, 2018). The error bars correspond to the 1σ confidence intervals. The model that includes hydrogen dissociation is a better fit (χ^2/datum = 3.4) than the one without (χ^2/datum = 4.3), with $\Delta\chi^2 = 11$. The energy balance model, with a common wind speed for all twelve planets, is a better fit to the data than the analytic model, but neither fully captures the trend.

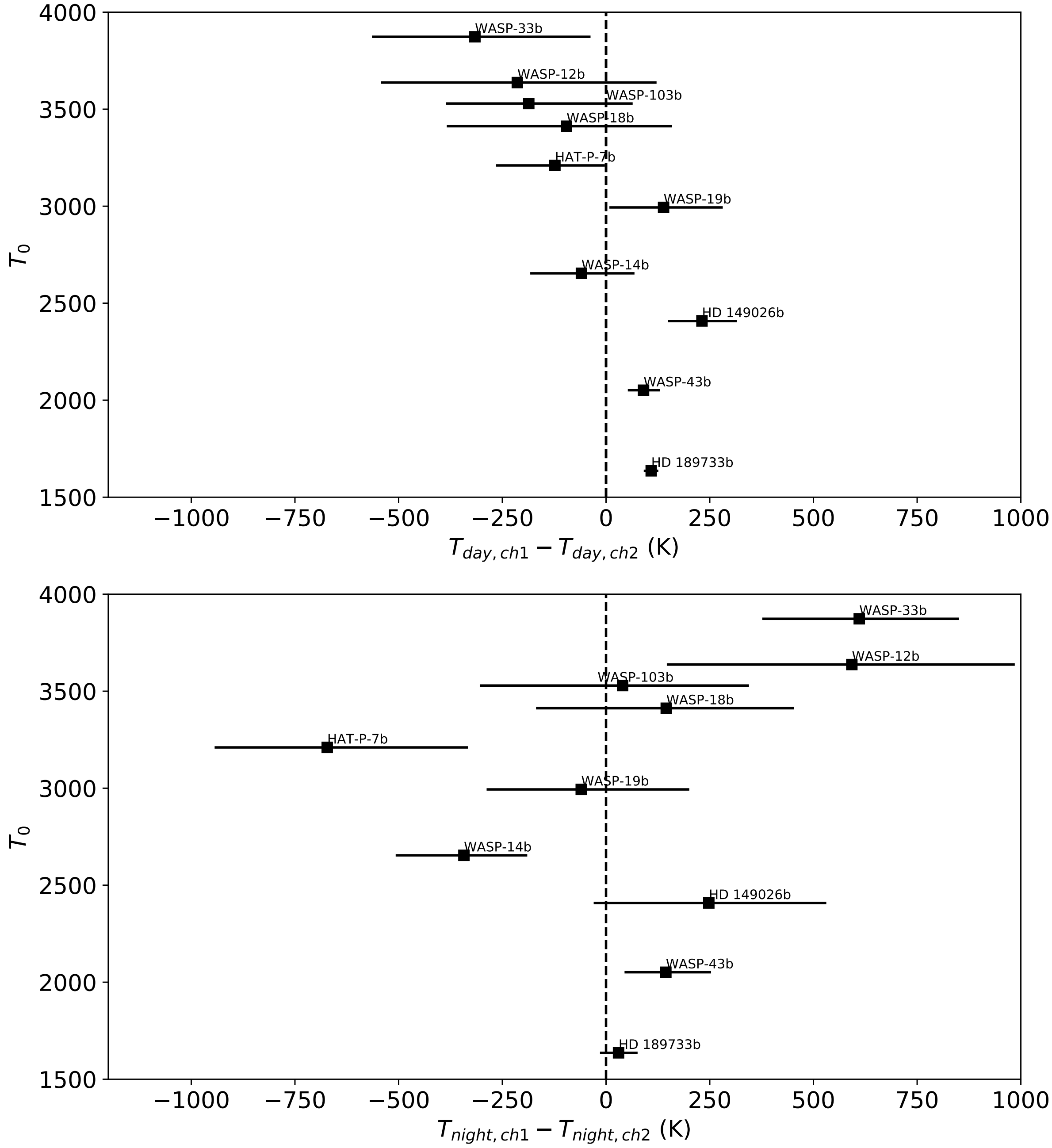

Figure 3.3: Difference in brightness temperatures at *Spitzer* wavelengths 3.6 μm and 4.5 μm for the ten planets with both 3.6 μm and 4.5 μm phase curves. The error bars correspond to the 1σ confidence intervals. *Top Panel:* Dayside brightness temperature colours. Cooler planets have blue IRAC colours (consistent with H_20 absorption), while hotter planets are isothermal or slightly red. *Bottom Panel:* Nightside brightness temperature colours. Half of the planets have nightside brightness temperature colours consistent with zero, meaning their nightside brightness temperatures are similar at both wavelengths. The rest are within 2σ of zero.

3.6 Methods

We estimated nightside effective temperatures with two different methods. We outline the methods in the sections that follow.

3.7 Method 1: Disk-Integrated Flux

Our fiducial analysis used the disk-integrated flux, from phase curves, to estimate effective temperatures. Previous efforts have used weighted averages or linear interpolation (Cowan and Agol, 2011b; Schwartz and Cowan, 2015; Schwartz et al., 2017). We used Gaussian Process regression (GP), to estimate the bolometric flux, and subsequently effective temperature and uncertainty given a handful of brightness temperatures, as it has recently been shown to produce more accurate uncertainty estimates (Pass et al., 2019).

The disk-integrated nightside brightness temperature is given by

$$T_{\mathrm{b,night}}(\lambda) = \frac{hc}{\lambda k}\left[\ln\left(1 + \frac{e^{hc/\lambda k T_*} - 1}{F_{\mathrm{night}}/\delta_{\mathrm{tra}}}\right)\right]^{-1}, \tag{3.1}$$

where λ is the wavelength of the observation, $T_\star$ is the brightness temperature of the star at that wavelength, δ_{tra} is the transit depth, and F_{night} is the planet-to-star flux ratio at a phase angle of π, where phase angle is defined to be 0 at secondary eclipse.

3.7.1 Propagation of Uncertainties

As the most common *Spitzer* decorrelation techniques have been shown to produce accurate, reproducible results (Ingalls et al., 2016), we chose to take all positive phase curves at face value. To estimate uncertainties on each planet's disk-integrated nightside flux and brightness temperature, we propagated uncertainties on planetary and stellar properties, and phase curve parameters, using a 1000 step Monte Carlo. The relevant physical properties are: the stellar effective temperature, stellar surface gravity, stellar metallicity, transit depth, and ratio of semi-major axis to stellar radius. We took the most up-to-date values from the literature. For each draw, we randomly sampled each parameter from a Gaussian centered on each best-fit published value, with the width given by the published uncertainty. This gives an approximately Gaussian probability density function for the nightside flux $\mathrm{Prob}(F_n) = f(T_n)$, where F_n is the nightside flux.

To calculate the brightness temperature for each nightside flux value, we inverted the Planck function at each flux to obtain a probability density function for nightside brightness temperature, T_n. This can be thought of as transforming the nightside flux probability density function to a function of nightside temperature through a change of variables. We have,

$$\mathrm{Prob}(T_n) = g(F_n(T_n))\frac{dF_n}{dT_n}, \tag{3.2}$$

where $F_n(T_n)$ is the Planck function (as a function of temperature, holding wavelength fixed), and $\frac{dF_n}{dT_n}$ is the derivative of the Planck function with respect to temperature. This transformation is only defined for positive fluxes and temperatures.

For most of the planets in our study, the nightside flux distribution is well above zero. The nightside temperature probability distribution also has a Gaussian-like shape, so we used the peak and width for our best-fit and uncertainty values. We took the average of the upper and lower limits when using the brightness temperatures to infer effective temperatures.

For planets with low or negative nightside flux, parts of the nightside flux probability distribution do not correspond to physical temperatures. This is typically interpreted to be a strong non-detection of nightside flux. Mathematically this is allowed, but physically, negative fluxes and temperatures are impossible. An example is HAT-P-7b at 3.6μm, where the peak of the probability density function $\mathrm{Prob}(F_n)$ is negative. In this case we set the best-fit flux, and hence brightness temperature, to zero, and used the width of the nightside flux distribution to calculate a 1σ upper limit on the brightness temperature, which we used as the error when estimating the bolometric flux. For planets with small but non-zero nightside flux (like WASP-18b at 3.6μm), a significant part of the flux distribution is negative, and the lower part gets truncated when converting to errors in brightness temperature. In these cases, we used the upper limit on brightness temperature when estimating bolometric flux and effective temperature, which is more conservative than taking the average of the upper and lower limits.

3.7.2 Brightness Temperature Difference Plot

To generate Figure 3.3, we used a 1000 step Monte Carlo. For each step in the Monte Carlo we calculated the difference between the 3.6 μm and 4.5 μm brightness temperatures. We took the mean and standard deviation of the distribution of differences for each planet.

3.8 Method 2: Mapping Method

We also calculated dayside and nightside temperatures by considering the brightness maps implied by each phase curve. For a planet on a circular, edge-on orbit, its orbital phase curve can be analytically inverted into a longitudinal brightness map (Cowan and Agol, 2008). WASP-14b has the highest eccentricity of the sample, $e = 0.08$. General circulation models using a small eccentricity ($e = 0.15$) predict negligible differences in circulation patterns compared to circular orbits (Lewis et al., 2010). For our purposes we treated the orbits of WASP-14b and the lower eccentricity planets in our sample as circular. We defined the phase curves to be $F(\xi)$, where ξ is the planet's phase angle ($\xi = 0$ at secondary eclipse, $\xi = \pi$ at transit). The corresponding brightness maps are defined as $J(\phi)$, where ϕ is longitude from the substellar point. We set $F(\xi = 0)$ equal to the eclipse depths, and obtained the map parameters analytically (Cowan and Agol, 2008).

Phase curves provide weak constraints on North-South asymmetry of planets (Cowan et al., 2013, 2017). It is possible to determine the latitudinal distribution using eclipse mapping, but so far this has only been done for HD 189733b at 8 μm (Majeau et al., 2012; de Wit et al., 2012; Rauscher et al., 2018). We therefore marginalize over the uncertainty in latitudinal brightness distributions when constructing the two-dimensional bolometric flux maps.

From the bolometric flux maps for the twelve planets, we obtained an estimate of the dayside and nightside effective temperatures of each planet.

3.8.1 Latitudinal Brightness Profiles

Longitudinal maps, $J(\phi)$, are weighted by the visibility of the observer, since the phase curve measures the disk-integrated flux from the planet. For an equatorial observer (a zero-obliquity planet orbiting edge-on), the longitudinal maps are related to the two-dimensional brightness distribution as a function of planetary co-latitude and longitude, $I(\theta, \phi)$, by

$$J(\phi) = \int_0^\pi I(\phi, \theta) \sin^2 \theta d\theta. \tag{3.3}$$

One of the powers of sine comes from the area element in spherical coordinates, and the other comes from the visibility for an equatorial observer. The longitudinal map $J(\phi)$ effectively integrates over the latitudinal dependence of $I(\phi, \theta)$. We adopted the simplifying assumption that $I(\phi, \theta)$ is separable, and accounted for our ignorance of the latitudinal dependence of brightness by letting it vary as $\sin^\gamma \theta$ with a polar brightness I_{pole}. The expression is

$$I_\lambda(\phi, \theta) = \left(\frac{J_\lambda(\phi) - \pi I_{\text{pole}}/2}{\int_0^\pi \sin^{2+\gamma} \theta d\theta} \right) \sin^\gamma \theta + I_{\text{pole}}(1 - \sin^\gamma \theta), \tag{3.4}$$

where I_{pole} is a constant representing the intensity at the poles. The full derivation can be found at the end of the Methods section. The $\gamma = 0$ case represents perfect poleward heat transport, or a constant temperature in the latitudinal direction. In the Rayleigh-Jeans limit of long wavelength, $I(\theta) \propto T(\theta)$, and thus $I(\theta) \propto T(\theta) \propto \sin^{1/4}(\theta)$ for no poleward heat transport, that is, $\gamma = 1/4$. To be conservative, we drew samples from the range $0 < \gamma \leq 1$, as we find that the value of γ doesn't drastically affect our calculated quantities. In Figure 3.11 we show how the value of γ changes the latitudinal brightness profile.

The brightness temperature map is related to the intensity map by the inverse Planck function

$$T_\lambda(\phi, \theta) = \frac{hc}{\lambda k} \left[\ln \left(1 + \frac{(e^{hc/\lambda k T_*} - 1)(R_p/R_\star)^2}{\pi I_\lambda(\phi, \theta)} \right) \right]^{-1}, \tag{3.5}$$

where T_* is the brightness temperature from Phoenix stellar models (Allard et al., 2011).

3.8.2 Brightness Temperatures to Effective Temperatures

From the wavelength dependent brightness maps in Equation (3.5), we inferred effective temperature maps. If the full spectrum at each location was known, one could integrate it to get the effective temperature at each location. Instead, we must estimate the bolometric flux by interpolating between, and extrapolating from, a few brightness temperatures. The Gaussian process regression used for the disk-integrated analysis is too computationally expensive to use at each location on the planet. We instead approximated the effective temperature via the error weighted mean (Schwartz and Cowan, 2015; Schwartz et al., 2017) of the brightness temperatures (or, in practice, the arithmetic mean of brightness temperatures, but embedded in a Monte Carlo). We adopted systematic uncertainties calibrated by performing such estimates on synthetic spectra (Pass et al., 2019). We took the arithmetic mean of the individual brightness temperatures at each location as an estimate of the effective temperature,

$$T_{\text{eff}}(\phi,\theta) = \frac{1}{n}\sum_{n} T_{\lambda,n}(\phi,\theta), \tag{3.6}$$

where n is the number of wavelengths. We propagated errors in a Monte Carlo fashion. From $T_{\text{eff}}(\phi,\theta)$ we calculated the disk-integrated dayside and nightside effective temperatures using the Stefan-Boltzmann law,

$$T_{\text{day}} = \frac{1}{2\pi}\int_{-\pi/2}^{\pi/2}\int_{0}^{\pi} T_{\text{eff}}^4(\phi,\theta)\sin\theta d\theta d\phi, \tag{3.7}$$

and

$$T_{\text{night}} = \frac{1}{2\pi}\int_{\pi/2}^{-\pi/2}\int_{0}^{\pi} T_{\text{eff}}^4(\phi,\theta)\sin\theta d\theta d\phi. \tag{3.8}$$

We also calculated the Bond albedo, the fraction of incoming stellar power that the planet reflects to space,

$$A_{\text{B}} \equiv 1 - \frac{\oint T_{\text{eff}}^4(\phi,\theta)\sin\theta d\theta d\phi}{\pi T_0^4}. \tag{3.9}$$

For day-night heat recirculation, we computed the ratio of heat radiated by the nightside to the total heat radiated by the planet,

$$\mathcal{P} = \frac{\int_{\pi/2}^{-\pi/2} \int_0^{\pi} T_{\text{eff}}^4(\phi, \theta) \sin\theta d\theta d\phi}{\oint T_{\text{eff}}^4(\phi, \theta) \sin\theta d\theta d\phi}. \tag{3.10}$$

Since the nightside absorbs no stellar radiation, this is the amount of heat that has moved from the dayside to nightside. A value of zero implies that no heat is transported to the nightside, and a value of 0.5 implies that half of the absorbed incoming stellar flux is recirculated to the nightside.

For each planet, we calculated T_{day}, T_{night}, A_{B}, and P simultaneously for 10^5 steps of a Monte Carlo. At each step we randomly drew all measured physical planetary parameters and published phase curve parameters from Gaussian distributions centered around their published values, with standard deviation given by their published uncertainties. We marginalized over our uncertainty of γ and I_{pole} by drawing these from a random uniform distribution where $0 \leq \gamma \leq 1$ and $0 \leq I_{\text{pole}} \leq \min \frac{2J(\phi)}{\pi}$. The constraint on I_{pole} ensures that the poles are not hotter than the equator. Lastly, we added the systematic uncertainty associated with estimating effective temperatures using the mean of a limited number of brightness temperatures; the systematic uncertainties are esimated based on retrieval exercises with synthetic cloud-free dayside emission spectra. The 1σ systematic uncertainties are 23% for planets with a phase curve at just 4.5 μm, 13% for planets with phase curves at 3.6 μm and 4.5 μm, and 3% for planets with phase curves at 3.6 μm, 4.5 μm, and 1.4 μm. This is a conservative estimate, as the observed nightside brightness temperatures are closer to isothermal than the dayside brightness temperatures (Figure 3.3).

3.8.3 Sensitivity Analysis

To determine how much each measured parameter affects the overall error of the calculated values, we performed a sensitivity analysis using the measured values, varying one parameter at a time. For most planets, the biggest source of uncertainty in the nightside temperatures is the systematic error we introduced, followed by the I_{pole} term. This suggests that obtaining phase curves at more wavelengths, as well as eclipse mapping, will yield better estimates of nightside effective temperatures.

3.8.4 Phase Curves and Brightness Maps

The first exoplanet map was of HD 189733b at 8 μm (Knutson et al., 2007). It showed an eastward shifted hotspot on the planet, in line with theoretical predictions of equatorial, super-rotating jets (Showman and Guillot, 2002). With the exception of HD 189733b (Knutson et al., 2007, 2009), 55 Cancri e (Demory et al., 2016; Angelo and Hu, 2017), CoRoT-2b (Dang et al., 2018), and WASP-43b (Louden and Kreidberg, 2018), WASP-103b (Kreidberg et al., 2018), and KELT-1b (Beatty et al., 2019), most phase curves have been fit and published without considering the brightness maps that could have produced them.

We distinguish between two problematic cases: negative phase curves, and positive phase curves that imply negative brightness maps, and explain how we handle these problematic cases. We summarize the suite of phase curves in Table 3.4.

3.8.5 Negative Phase Curves

A phase curve that is negative at any value of orbital phase guarantees that the underlying brightness distribution (map) is negative at some longitudes, because a phase curve measures the disk-integrated flux. Every phase curve that goes negative at any point implies the planet has negative flux somewhere.

The planets HAT-P-7b, WASP-14b, and WASP-43b have published phase curves that are negative on their nightsides, which ensures unphysical, negative brightness maps for these planets. The best one can do without refitting the phase curves is to modify the phase curves or brightness maps in some way. A possible solution previously adopted for WASP-43b is simply setting negative regions of each of brightness maps to zero (Keating and Cowan, 2017). The WFC3 phase curves for WASP-43b have since been refit while enforcing physically possible brightness maps and accounting for reflected light, resulting in a much higher nightside temperature than previous reported (Stevenson et al., 2014;

Louden and Kreidberg, 2018). The *Spitzer* phase curves for WASP-43b were refit by using a different instrument sensitivity model, shown to be better at removing residual red noise due to intra-pixel sensitivity, also resulting in much higher nightside temperatures (Mendonça et al., 2018). We use the reanalyzed *Spitzer* phase curves for our analysis. For the WFC3 phase curve, we treated the negative nightside flux as an upper limit, rather than simply setting the negative parts of the map to zero. We do not use the reanalyzed WFC3 phase curves as they were not fit with sinusoids, and hence could not be treated in a consistent manner to the other phase curves.

The published HAT-P-7b and WASP-14b 3.6 μm phase curves are negative on their nightsides. This can occur when not enforcing positive brightness maps when fitting the data. We refit both phase curves while enforcing physically possible phase variations, using a polynomial function to model detector systematics (Dang et al., 2018). For WASP-14b, we were able to obtain a good fit. The nightside temperature we infer is 4 K lower than when using the Monte Carlo rejection method. For HAT-P-7b, we were not able to obtain a good fit without allowing the phase curve to have significantly negative nightside flux. As the planet cannot have negative brightness, this could potentially be due to some unmodelled stellar effect, such as non-uniform stellar brightness, or that the detector models are inadequate for these particular data. For the purposes of this study, we chose to treat the negative nightside flux as an upper limit when estimating the effective temperature.

3.8.6 Positive Phase Curves, Negative Brightness Maps

It is also possible to measure a strictly positive phase curve, yet infer a brightness map that is not strictly positive. This is the case for WASP-12b, WASP-18b, WASP-19b, and WASP-103b. Although it is *mathematically* possible to obtain a non-negative phase curve from a brightness map that is not strictly positive, such a brightness map is physically impossible. This was pointed out long ago in the case of reflected light curves from asteroids (Russell, 1906), which is mathematically similar to the thermal emission case. Brightness maps obtained from inverting sinusoidal phase curves are not unique, as there is a nullspace of the transformation from map to light curve— excluding the fundamental mode, any odd sinusoidal mode present in the brightness map of a synchronously rotating planet on a circular, edge-on orbit will integrate to zero over a hemisphere, and will thus be invisible in the phase curves (Cowan and Agol, 2008; Cowan et al., 2013). If a measured phase curve implies a negative brightness map, then it may be possible to add higher order odd harmonics to correct the map — indeed, if a solution exists, then odd brightness map harmonics are necessary to ensure a physically possible solution.

For example, WASP-18b has strictly positive phase curves that were fit with first and second order sinusoids (Maxted et al., 2013). However, the published 3.6 μm phase curve parameters imply a negative brightness map at this wavelength. For each draw in our Monte Carlo, if the phase curve is positive but the brightness map is negative at any location for any planet, we numerically solve for the smallest amplitude third order harmonic that makes the brightness map non-negative. If no such solution exists, we reject the draw. We demonstrate this in Figure 3.7.

The brown dwarf KELT-1b also has positive phase curves that imply negative brightness maps (Beatty et al., 2019). The authors showed that a smoothed trapezoidal brightness map integrates to give an approximately sinusoidal phase curve close to their fiducial phase curve for KELT-1b, and conclude that KELT-1b's map must be non-sinusoidal. They argue that this solves the problem of negative brightness maps, and implies that all planets with seemingly negative sinusoidal brightness maps must instead have non-sinusoidal maps. As we have shown, for some planets with positive phase curves, the brightness map can be made non-negative by just adding the third harmonic to the brightness map. In fact, adding higher order sinusoids allows for trapezoidal temperature maps, or any other continuous function (in other words, Fourier analysis). The odd harmonic method is elegant and more robust than adopting a specific non-sinusoidal parameterization, and does not alter the phase curve. It may be necessary to fit for the odd map harmonics when fitting phase curves– even though they are not visible in the phase curve, they may be needed to ensure a physically possible map.

Lastly, the phase curves of WASP-12b are contentious — if the fiducial, polynomial fit for the 4.5 μm phase curve is taken to be solely due to brightness variations of a spherical planet, the map is negative and unphysical (Cowan et al., 2012). The authors note that part of the second harmonic could be due to ellipsoidal variations. A reanalysis of the same data, and a second set of phase observation at the same wavelengths, found that the 4.5 μm results were consistent with the previous results (Zhang et al., 2018). We adopt the interpretation ultimately chosen by the authors of the first paper: some of the second harmonic in the 4.5 μm phase curve is due to the planet's inhomogeneous temperature map, but the rest is due to ellipsoidal variations. To be consistent with their interpretation, we set the planet's aspect ratio to 1.5, calculated the resulting amplitude (Cowan et al., 2012), and subtracted it from the second order amplitude to yield a non-negative brightness map.

3.8.7 Dynamical Model

The radiative timescale in the analytic, dynamical model is scaled by pressure at the base of the radiatively active layer of the atmosphere, and equilibrium temperature (Komacek et al., 2017; Komacek and Tan, 2018; Zhang and Showman, 2017). Figure 3.8 shows a version of the model where all the planets have the same physical properties, but the irradiation temperature varies.

We updated the radiative timescale formulation to scale with P/g, as with the energy balance model. We neglected magnetic drag. Magnetic drag could decrease nightside temperatures for planets where magnetic drag is predicted to be significant ($T_0 \sim 2000$ K and up) (Komacek et al., 2017). Presumably, hotter planets have more ionized atmospheres, and thus shorter drag timescales due to interactions with magnetic fields. We "anchor" the air column mass to the nightside temperature of HD 189733b which has $T_0 = 1636$ K, and thus presumably no appreciable magnetic drag, so we can safely set the magnetic drag timescale to infinity. The predictions for the nightside temperatures of the more irradiated planets at this air column mass are all significantly *lower*, rather than higher, than the observed nightside temperatures. See Figure 3.10. Nightside clouds could only further depress the nightside effective temperature. This simple parameterization of magnetic drag is not sufficient to explain the entire nightside temperature trend, and including it gives a worse fit to the observations. This does not allow us to exclude the effects of magnetic fields in hot Jupiter atmospheres— instead, it motivates the need to include magnetohydrodynamics in general circulation models of hot Jupiter atmospheres.

The dynamical models do not predict the dayside or nightside temperatures themselves, but rather the day-to-night temperature contrast. To predict the nightside temperature, we use the analytic expression from the model to calculate the day-night temperature contrast, and solve for the nightside temperature, assuming that the dayside temperature is equal to the equilibrium temperature defined by $T_{\mathrm{eq}} = (1/4)^{1/4} T_0$ (a good approximation, as shown in the top panel of Figure 3.1). In true radiative equilibrium, the nightside temperature of a tidally locked, synchronously rotating planet would be zero. However, we note that GCMs suggest that the nightsides of hot Jupiters can never reach temperatures as cold as expected in radiative equilibrium (Komacek et al., 2017).

Rather than use a common photosphere pressure among the planets as has been previously done, we fit for a common air column mass above the emitting region, that is, the photosphere pressure (P) scaled by acceleration due to gravity (g): P/g. It is more a realistic assumption than a common photosphere pressure among the planets, as hot Jupiter masses, and hence surface gravities, can span an order of magnitude.

3.9 Data availability

The data that support the plots within this paper and other findings of this study are available from the corresponding author upon reasonable request.

3.10 Code availability

The Gaussian process regression code used is publicly available, and can be found here. The *Spitzer* Phase Curve Analysis pipeline is publicly available and can be found here.

3.11 Supplementary Information

The following figures and tables were included as supplementary information in the published version.

Table 3.2: Summary of model fits to the disk-integrated results. The best-fit parameters have values that are reasonable for hot Jupiters, with the best-fit P/g corresponding to a range of pressures between about 0.1 and 10 bar across the suite of planets in our sample. The best-fit wind speed for the energy balance model is also reasonable, as typical hot Jupiter wind speeds are on the order of 1 $km.s^{-1}$.

Model	$\chi^2/datum$	P/g (kgm^{-2})	$v_{\rm wind}$ ($km.s^{-1}$)
Bell and Cowan (2018)	3.4	$(1.7 \pm 0.2) \times 10^3$	1.4 ± 0.2
Cowan and Agol (2011)	4.3	$(1.9 \pm 0.5) \times 10^3$	1.3 ± 0.9
Komacek and Tan (2018)	4.5	$(2.1 \pm 0.3) \times 10^3$	
Zhang and Showman (2017)	8.5	$(3.1 \pm 0.4) \times 10^3$	

Table 3.3: Dayside Temperatures, Nightside Temperatures, and Energy Budget Parameters using the mapping approach described in the methods section. Our heat recirculation parameter, $\mathcal{P}$, ranges from 0, for no day-night heat recirculation, to 0.5, for perfect day-night heat recirculation. $A_{\rm B}$ is the Bond Albedo.

	T_0 K	T_{day} K	T_{night} K	A_B	$\mathcal{P}$
HD 189733b	1636±15	1172±154	913±125	$0.39^{+0.25}_{-0.24}$	$0.27^{+0.02}_{-0.02}$
HD 209458b	2051±36	1323±316	1024±248	$0.63^{+0.24}_{-0.33}$	$0.26^{+0.03}_{-0.03}$
WASP-43b	2052±55	1483±197	993±134	$0.43^{+0.22}_{-0.25}$	$0.17^{+0.02}_{-0.01}$
CoRoT-2b	2175±47	1584±372	833±197	$0.6^{+0.26}_{-0.36}$	$0.07^{+0.01}_{-0.01}$
HD 149026b	2409±58	1703±233	1160±173	$0.47^{+0.22}_{-0.27}$	$0.18^{+0.04}_{-0.03}$
WASP-14b	2655±41	2147±292	1291±183	$0.33^{+0.25}_{-0.21}$	$0.12^{+0.01}_{-0.01}$
WASP-19b	2994±52	2046±272	1228±169	$0.53^{+0.2}_{-0.25}$	$0.12^{+0.02}_{-0.02}$
HAT-P-7b	3214±75	2383±340	1459±227	$0.43^{+0.25}_{-0.25}$	$0.12^{+0.03}_{-0.02}$
WASP-18b	3411±52	2699±381	1201±196	$0.37^{+0.23}_{-0.21}$	$0.04^{+0.02}_{-0.01}$
WASP-103b	3524±97	2639±113	1597±70	$0.29^{+0.12}_{-0.15}$	$0.12^{+0.01}_{-0.01}$
WASP-12b	3643±122	3093±452	2110±325	$0.3^{+0.22}_{-0.21}$	$0.18^{+0.03}_{-0.03}$
WASP-33b	3875±106	2761±398	1722±264	$0.49^{+0.21}_{-0.28}$	$0.13^{+0.02}_{-0.02}$

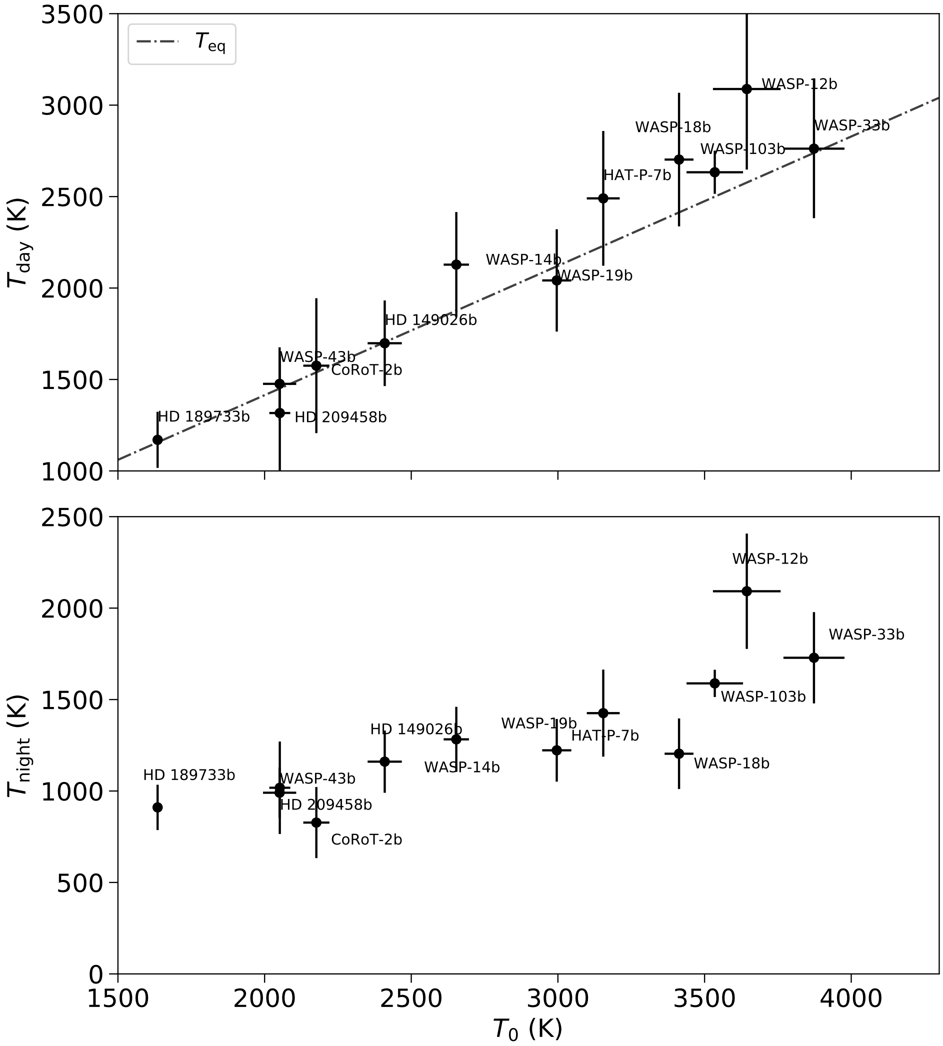

Figure 3.4: Dayside and nightside temperatures using the mapping method.

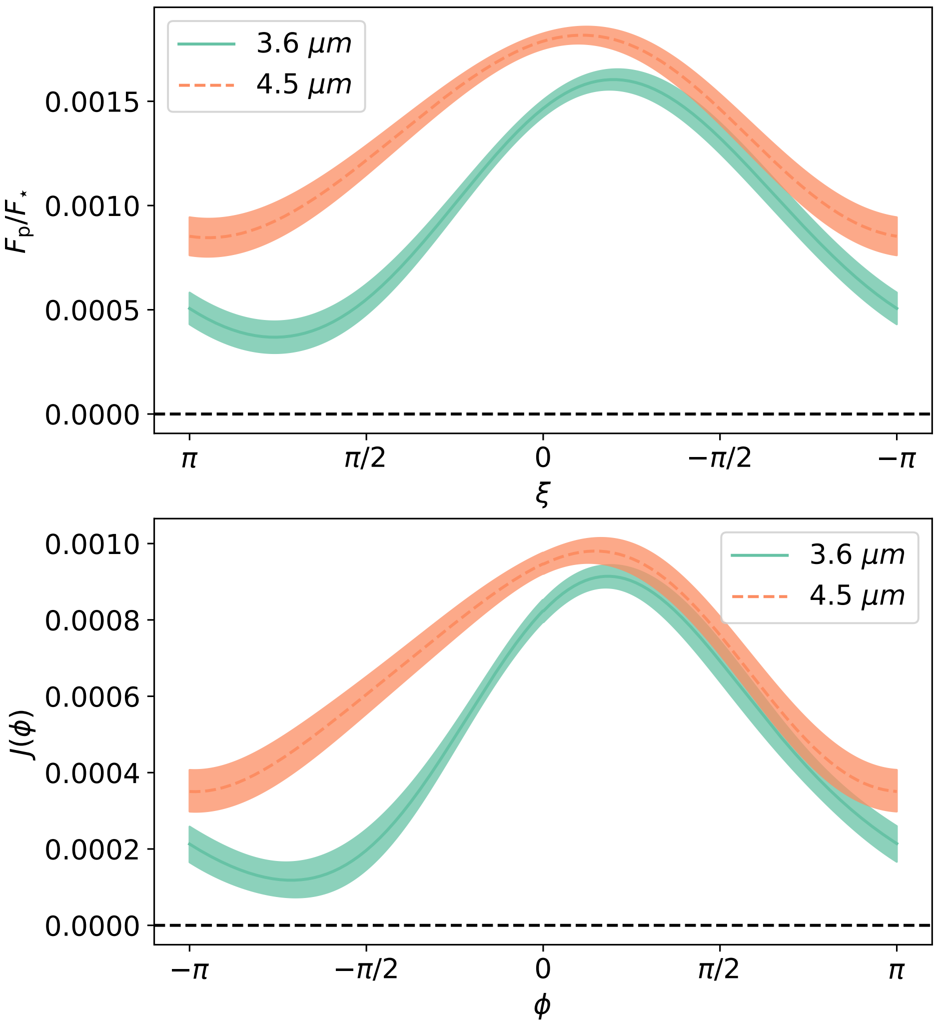

Figure 3.5: Example phase curve with corresponding longitudinal brightness maps for HD 189733b.

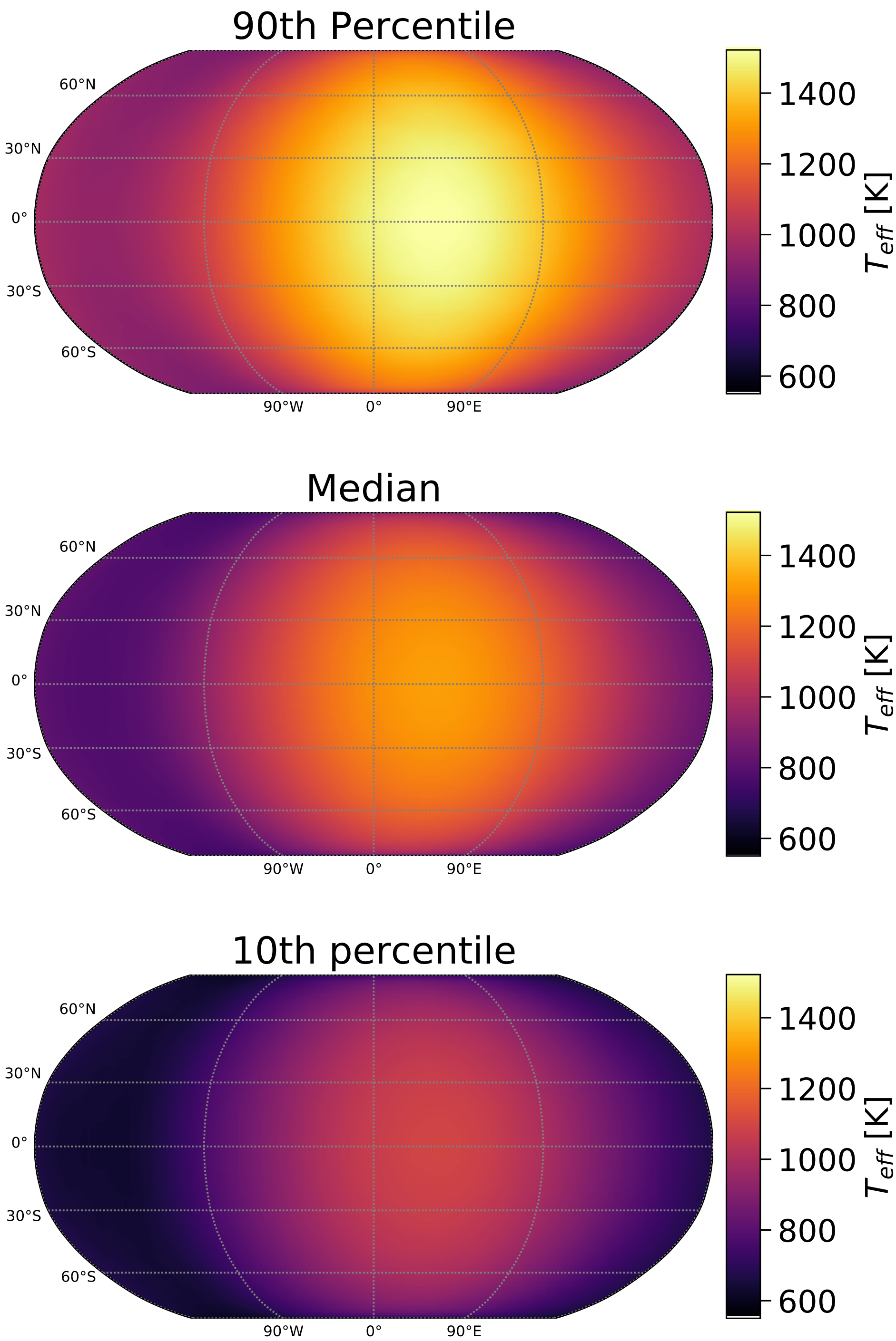

Figure 3.6: Two-dimensional effective temperature map of HD 189733b.

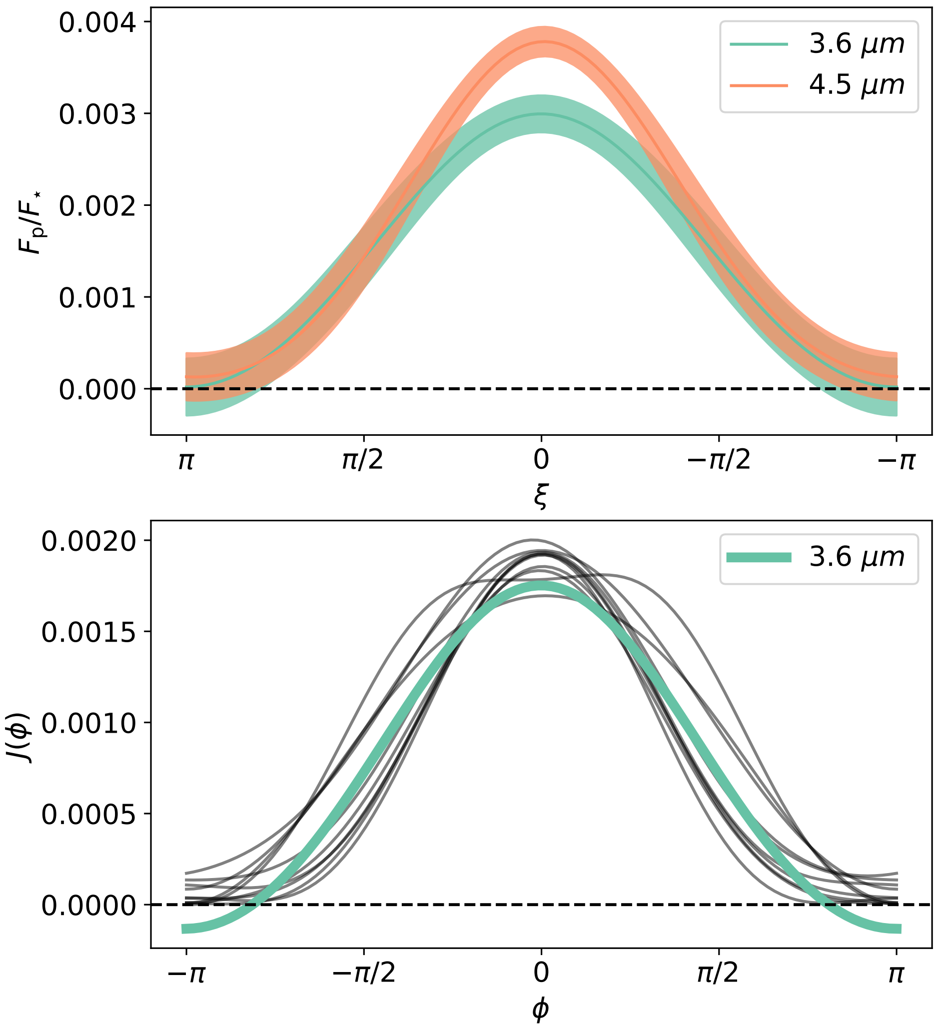

Figure 3.7: Effect of adding odd harmonics to a longitudinal brightness map.

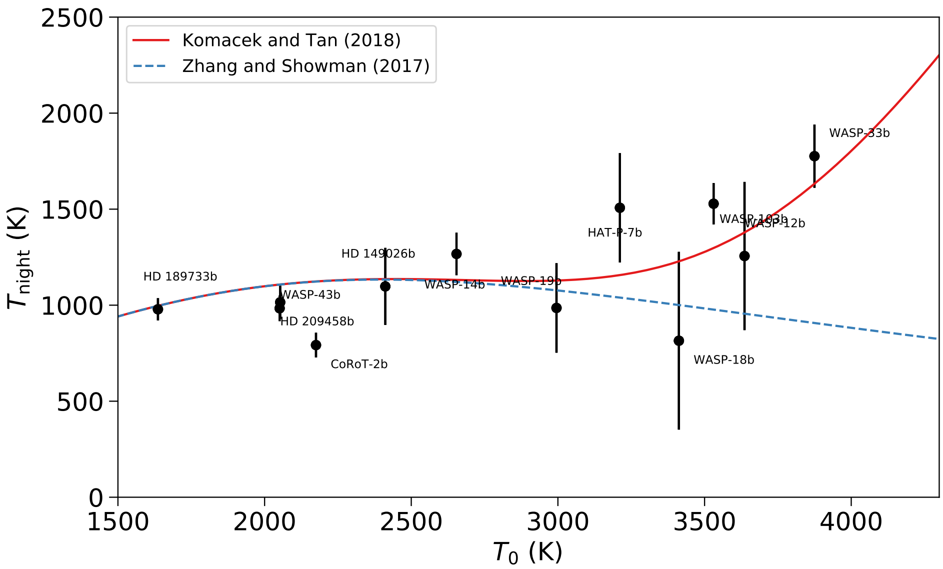

Figure 3.8: Qualitative behavior of the analytic dynamical model we fitted.

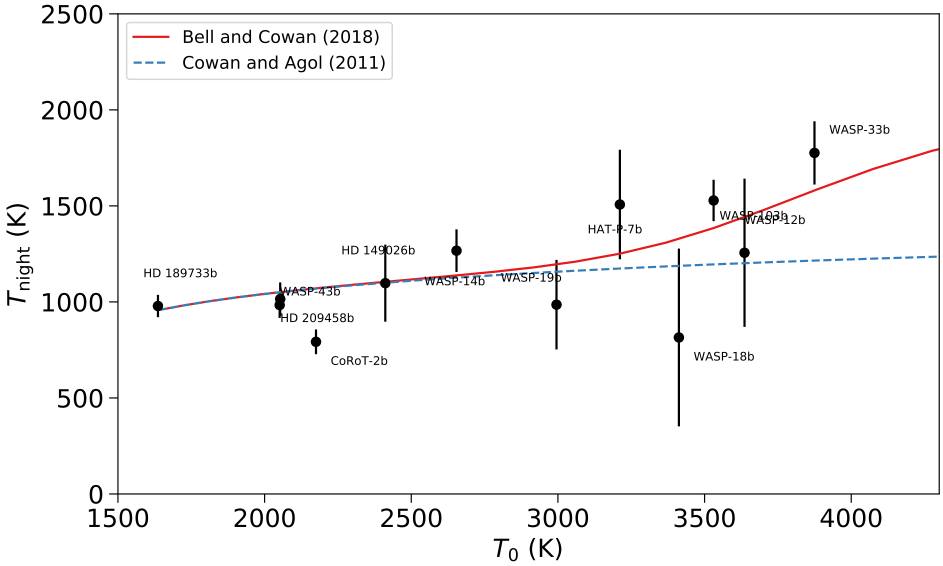

Figure 3.9: Behaviour of the semi-analytic energy balance models.

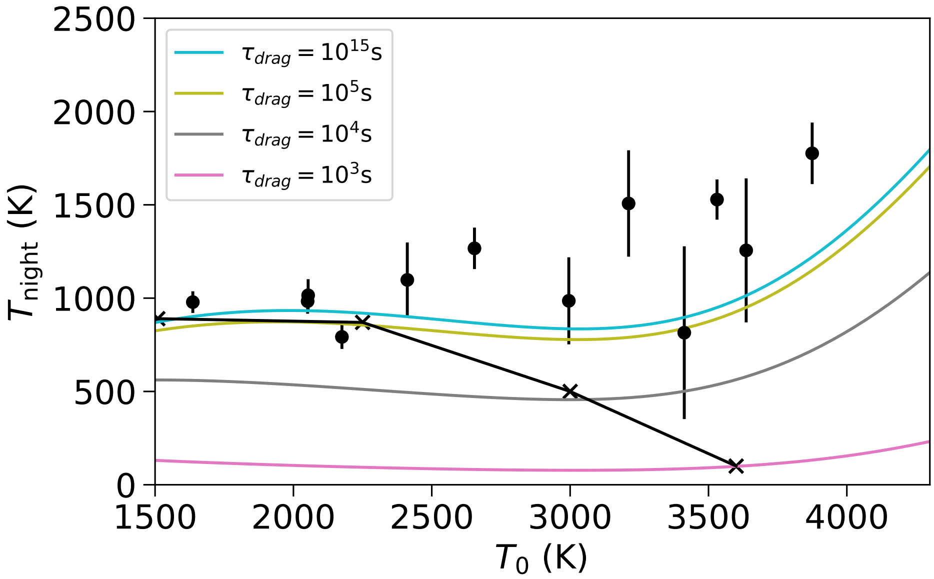

Figure 3.10: Nightside temperature trends for varying amounts of drag in the dynamical model.

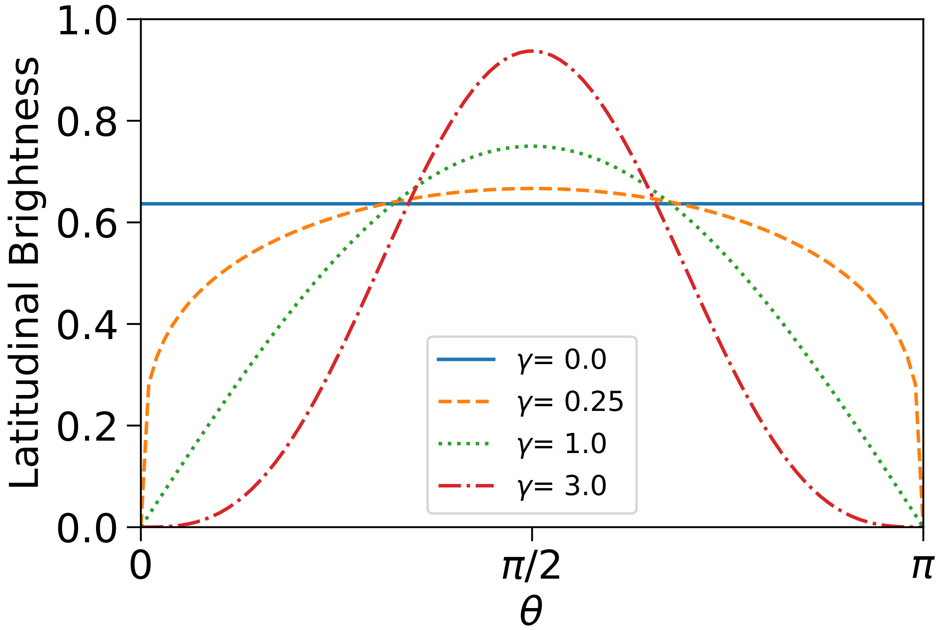

Figure 3.11: Various latitudinal brightness distributions.

Table 3.4: Summary of problematic hot jupiter phase curve observations. Plus signs denote phase curve or maps for which the mean phase curve or map is strictly positive. Minus signs denote phase curves or maps that are negative for any value of orbital phase, or longitude. Planet names in bold are planets with problematic phase curves. We also list the type of correction we use to deal with each problematic phase curve. Odd Harmonics means we correct the negative map by adding odd harmonics. We explain the correction for WASP-12b in the Methods. For HAT-P-7b at 3.6 μm, we used the negative nightside flux distribution to get an upper limit on brightness temperature in the phase curve method, and used Odd Harmonics rejection with the mapping method.

Planet Name	1.4 μm	3.6 μm	4.5 μm	1.4 μm Map	3.6 μm Map	4.5 μm Map	Correction
CoRoT-2b	N/A	N/A	+	N/A	N/A	+	
HAT-P-7b	N/A	−	+	N/A	−	+	Upper Limit / Odd harmonics
HD 149026b	N/A	+	+	N/A	+	+	
HD 189733b	N/A	+	+	N/A	+	+	
HD 209458b	N/A	N/A	+	N/A	N/A	+	
WASP-12b	N/A	+	+	N/A	−	−	Ellipsoidal Variations
WASP-14b	N/A	−	+	N/A	−	+	Refit 3.6μm
WASP-18b	N/A	+	+	N/A	−	+	Odd Harmonics
WASP-19b	N/A	+	+	N/A	−	+	Odd Harmonics
WASP-33b	N/A	+	+	N/A	+	+	
WASP-43b Old	−	−	−	−	−	−	
WASP-43b New	−	+	+	+	+	+	
WASP-103b	+	+	+	−	+	+	Odd Harmonics

3.12 Epilogue

This Chapter showed through a meta-analysis that hot Jupiters all have similar nightside temperatures: around 1100 K. The simplest explanation is that hot Jupiters all have nightside clouds with a similar composition. Ultra-hot Jupiters have an additional source of heat transport available to them in the form of hydrogen dissociation and recombination, which evaporates nightside cloud particles on these planets. The interpretation of clouds modulating *Spitzer* phase curves was also suggested by (Beatty et al., 2019) in an analysis using nightside brightness temperatures.

Both our analysis and that of Beatty et al. (2019) used phase curves that were analyzed by different groups using different *Spitzer* pipelines. Recently, Bell et al. (2020) performed a uniform data reduction and reanalysis of 15 *Spitzer* phase curves and confirmed the shallow dependence of nightside temperature on irradiation temperature.

3.13 Interlude: adventures in mapping

As part of the analysis in this Chapter, I explored longitudinal mapping of hot Jupiters. This exploration on mapping led to me joining two collaborations at the "Multi-dimensional characterization of distant worlds: spectral retrieval and spatial mapping" workshop hosted by the Michigan Institute for Research in Astrophysics, and spearheaded by Emily Rauscher. I was the second author on one manuscript that is currently under review, and a contributing author on a second one that was published in December 2020.

In our submitted manuscript, "Longitudinally Resolved Spectral Retrieval (ReSpect) of WASP-43b Cubillos et al. (2021)" we demonstrated a new method to retrieve the atmospheric composition of hot Jupiters using longitudinally resolved spectra. The most common atmospheric retrieval schemes use disk-integrated spectra. Disk-integrated retrievals been shown to potentially bias results, because they treat each hemisphere of a planet as homogeneous. In our approach, we analytically convert disk-integrated spectroscopic phase curves to spectroscopic, longitudinal brightness maps (Cowan and Agol, 2008), which are used to retrieve atmospheric abundances as a function of longitude.

We showed that applying the technique to simulated JWST data from a WASP-43b GCM gave more accurate atmospheric abundances compared to a disk-integrated version retrieval for the same computational cost. WASP-43b will be observed extensively with Guaranteed Time Observations on JWST so it will soon be possible to apply this technique to those data.

In the paper "Eigenspectra: A Framework for Identifying Spectra from 3D Eclipse Mapping" (Mansfield et al., 2020b), we showed how to use spectroscopic eclipse observations to construct maps of the dayside of a hot Jupiter as a function of latitude, longitude, and wavelength— effectively, three dimensional dayside maps. These maps can be used to determine the brightspot location, and atmospheric composition as a function of latitude and longitude. My contribution was code that uses K-means clustering, a machine learning algorithm, to group together regions with similar spectra in order to produce several characteristic spectra that can be used for atmospheric retrieval. Although not currently feasible with the signal-to-noise and wavelength coverage of current telescopes, 3D eclipse mapping of bright targets like HD 189733b will be possible with JWST.

4 Smaller than expected bright-spot offsets in Spitzer phase curves of the hot Jupiter Qatar-1b

4.1 Prologue

Most of the phase curves used in the previous chapter were analyzed by different groups, using disparate reduction and analysis pipelines. Although several of the most commonly used pipelines were shown to yield accurate and repeatable results for eclipse observations (Ingalls 2016), no rigorous comparison has been done for full-orbit phase curves. This Chapter presents a reduction and analysis of Spitzer phase curves of the hot Jupiter Qatar-1b using two different pipelines.

In 2019 I was funded by a McGill Graduate Mobility Award to participate in a research stay at the Space Telescope Science Institute in Baltimore, Maryland where I began a collaboration with Kevin Stevenson, and learned how to use his group's Photometry for Orbits, Eclipses, and Transits (POET) pipeline. I compared it with a preliminary version of the open-source and user friendly Spitzer Phase Curve Analysis (SPCA) pipeline, written by Taylor Bell and Lisa Dang from our exoplanet characterization group at McGill.

Qatar-1b is an interesting target because it has the same irradiation temperature as HD 209458b and WASP-43b, but its mass, radius, and orbital period are intermediate between those of HD 209458b and WASP-43b. This was the first work to compare phase curves of more than two hot Jupiters with the same irradiation temperature, and is a precursor to comparative planetology studies that will be performed with next generation telescopes.

4.2 Abstract

We present *Spitzer* full-orbit thermal phase curves of the hot Jupiter Qatar-1b, a planet with the same equilibrium temperature—and intermediate surface gravity and orbital period—as the well-studied planets HD 209458b and WASP-43b. We measure secondary eclipse of $0.21 \pm 0.02\%$ at 3.6 μm and $0.30 \pm 0.02\%$ at 4.5 μm, corresponding to day-side brightness temperatures of 1542^{+32}_{-31} K and 1557^{+35}_{-36} K, respectively, consistent with a vertically isothermal dayside. The respective nightside brightness temperatures are 1117^{+76}_{-71} K and 1167^{+69}_{-74} K, in line with a trend that hot Jupiters all have similar nightside temperatures. We infer a Bond albedo of $0.12^{+0.14}_{-0.16}$ and a moderate day-night heat recirculation efficiency, similar to HD 209458b. General circulation models for HD 209458b and WASP-43b predict that their bright-spots should be shifted east of the substellar point by tens of degrees, and these predictions were previously confirmed with *Spitzer* full-orbit phase curve observations. The phase curves of Qatar-1b are likewise expected to exhibit eastward offsets. Instead, the observed phase curves are consistent with no offset: $11^\circ \pm 7^\circ$ at 3.6 μm and $-4^\circ \pm 7^\circ$ at 4.5 μm. The discrepancy in circulation patterns between these three otherwise similar planets points to the importance of secondary parameters like rotation rate and surface gravity, and the presence or absence of clouds, in determining atmospheric conditions on hot Jupiters.

4.3 Introduction

Qatar-1b is a short-period gas giant (hot Jupiter), discovered with the Qatar Exoplanet Survey (Alsubai et al., 2011). Its mass, radius, and orbital period are all intermediate between those of the well-studied hot Jupiters WASP-43b and HD 209458b. The three planets all have the same equilibrium temperature (see Table 4.1). WASP-43b and HD 209458b were predicted and observed to have eastward phase curve bright-spot offsets, suggesting the presence of superrotating equatorial jets in their atmospheres (Showman et al., 2009; Zellem et al., 2014; Stevenson et al., 2014, 2017; Mendonça et al., 2018; Morello et al., 2019; Kataria et al., 2015). If the stellar flux a planet receives is what

Table 4.1: Summary of planetary properties for HD 209458b (Stassun et al., 2017), Qatar-1b (Collins et al., 2017), and WASP-43b (Esposito et al., 2017). Qatar-1b's physical properties are intermediate between those of HD 209458 and WASP-43, except for the metallicity, which is somewhat greater than HD 209458, but consistent with WASP-43.

Planet Name	Equilibrium Temperature (K)	Period (Days)	Mass (M_{Jup})	Radius (R_{Jup})	Surface Gravity (ms^{-2})	Stellar Metallicity [Fe/H]
HD 209458b	1412 ± 64	3.52	0.73 ± 0.04	1.39 ± 0.02	$9.79^{+0.61}_{-0.59}$	0.0 ± 0.05
Qatar-1b	1418 ± 27	1.42	$1.294^{+0.052}_{-0.049}$	$1.143^{+0.026}_{-0.025}$	$25.677^{+1.577}_{-1.489}$	$0.171^{+0.097}_{-0.094}$
WASP-43b	1427 ± 19	0.83	1.998 ± 0.079	1.006 ± 0.017	51 ± 11	0.05 ± 0.170

primarily determines its atmospheric dynamics, we expect the circulation of Qatar-1b to be similar to WASP-43b and HD 209458b.

The dayside brightness temperatures of Qatar-1b has been measured previously. Secondary eclipse measurements in the K_s band implied an unusually high dayside brightness temperature of 1885^{+212}_{-168} K, which taken at face value suggests negligible day-night heat redistribution for this planet (Cruz et al., 2016). Secondary eclipse measurements with *Spitzer*, combined with the K_s band eclipse depth, yielded a dayside effective temperature of 1506 ± 71 K (Garhart et al., 2018), which allows for a modest degree of heat recirculation. However, full-orbit phase curve observations are the only way to quantify the day-night heat recirculation, due to the degeneracy between recirculation efficiency and albedo when interpreting eclipse only observations.

In this work, we present *Spitzer* full-orbit phase curves for Qatar-1b, at 3.6 μm and 4.5 μm. From the phase curves we calculate the dayside and nightside temperatures, and in turn obtain an estimate of the Bond albedo and day-night heat recirculation efficiency (Cowan and Agol, 2011a).

4.4 Observations and Data Analysis

The observations consist of two full-orbit phase curves of Qatar-1b, taken with the IRAC instrument on board the *Spitzer Space Telescope* (Fazio et al., 2004). Phase variations were observed at 3.6 μm on April 28, 2018, and at 4.5 μm on May 2, 2018 (PID 13038, PI: Kevin Stevenson). Both used 2 s exposure times. We performed two parallel analyses using two completely independent pipelines. The first analysis used the Photometry for

Orbits, Eclipses, and Transits (POET) pipeline (Stevenson et al., 2012c; Cubillos et al., 2013), and the second used the Spitzer Phase Curve Analysis (SPCA) pipeline (Dang et al., 2018; Bell et al., 2019). Since the astrophysical signal is often buried 2–3 orders of magnitude below detector systematics, *Spitzer* results have sometimes been debated (Hansen et al., 2014; Schwartz et al., 2017). While several of the most common IRAC detector systematics models produce accurate, repeatable eclipse depths (Ingalls et al., 2016), such a study has never been performed for full-orbit phase curves. It is therefore becoming common to use multiple pipelines when analyzing phase curve observations (Dang et al., 2018; Bell et al., 2019; Mansfield et al., 2020a). We followed previous analyses as closely as possible to ensure a fair comparison between both pipelines.

4.4.1 Photometry

SPCA

SPCA first performs 4σ outlier rejection to flag frames in a given *Spitzer* datacube containing an outlier pixel within a 5×5 box centered on the pixel (15,15). Next, the pipeline performs frame-by-frame background subtraction by taking the median pixel value of each frame, excluding a 7×7 pixel box centered on the pixel (15, 15). The pipeline uses aperture photometry to sum the remaining flux, and estimates the centroids using either the flux weighted mean (FWM) of each frame or by fitting a 2D Gaussian.

POET

POET first performs frame by frame outlier rejection using two-iteration, four-sigma clipping to flag bad pixels. Next it fits a 2D gaussian to find the centroid of each frame, and uses the centroids to perform $5\times$ interpolated aperture photometry. The background flux is calculated using an annulus with an inner ring of 7 pixels and an outer ring of 15 pixels, and subtracted from the total.

4.4.2 Centroiding

The biggest source of noise in *Spitzer* observations of bright, transiting planets is detector systematics. For IRAC Channels 1 and 2 (3.6 μm and 4.5 μm) this is due to intrapixel sensitivity variations coupled with changes in target centroids. The IRAC detector pixels are not uniformly sensitive, and during each observation, the target drifts slightly across them. By now this effect is well studied, and several of the most commonly used systematics models were shown to produce repeatable, accurate eclipse depths for both real and synthetic eclipse data (Ingalls et al., 2016). Most schemes use the flux centroids to model the intrapixel sensitivity fluctuations and subtract them from the signal, which makes it crucial to obtain the correct centroids. Flux weighted mean and Gaussian centroiding are the two most commonly used methods.

In tests with synthetic data of the IRAC 3.6μm and 8μm detectors, Gaussian centroiding was shown to be more precise than the flux weighted mean method (Lust et al., 2014). However, this does not necessarily apply to every data set. In particular, Gaussian centroiding performs poorly on asymmetric point response functions. Additionally, fitting a Gaussian can introduce noise from the fitting process, whereas the flux weighted mean is computed arithmetically.

In our SPCA analysis, we tested both 2D Gaussian centroiding and flux weighted mean centroiding, using a range of apertures in increments of 0.25 pixels, as well as both fixed and moving apertures. To choose the aperture size for each centroiding method, we calculated the RMS scatter between the raw photometry, and a boxcar smoothed version of the photometry with a width of 10 datacubes ($\sim$ 21 minutes). We selected the aperture size with the lowest RMS scatter. In all cases, we found that apertures centered on the derived centroids (moving apertures) produced the least RMS scatter. For the 4.5 μm observations, a 3.25 pixel radius aperture centered using flux weighted mean, gave the least RMS scatter. For the 3.6 μm observations, a 4.25 pixel radius aperture using 2D Gaussian centroiding gave the least RMS scatter. For a given channel and aperture size, the flux difference between centroiding schemes was less than the scatter in the raw flux, meaning both centroiding schemes gave essentially the same raw flux. However, both schemes yielded significantly different centroid locations (see fig. 4.1).

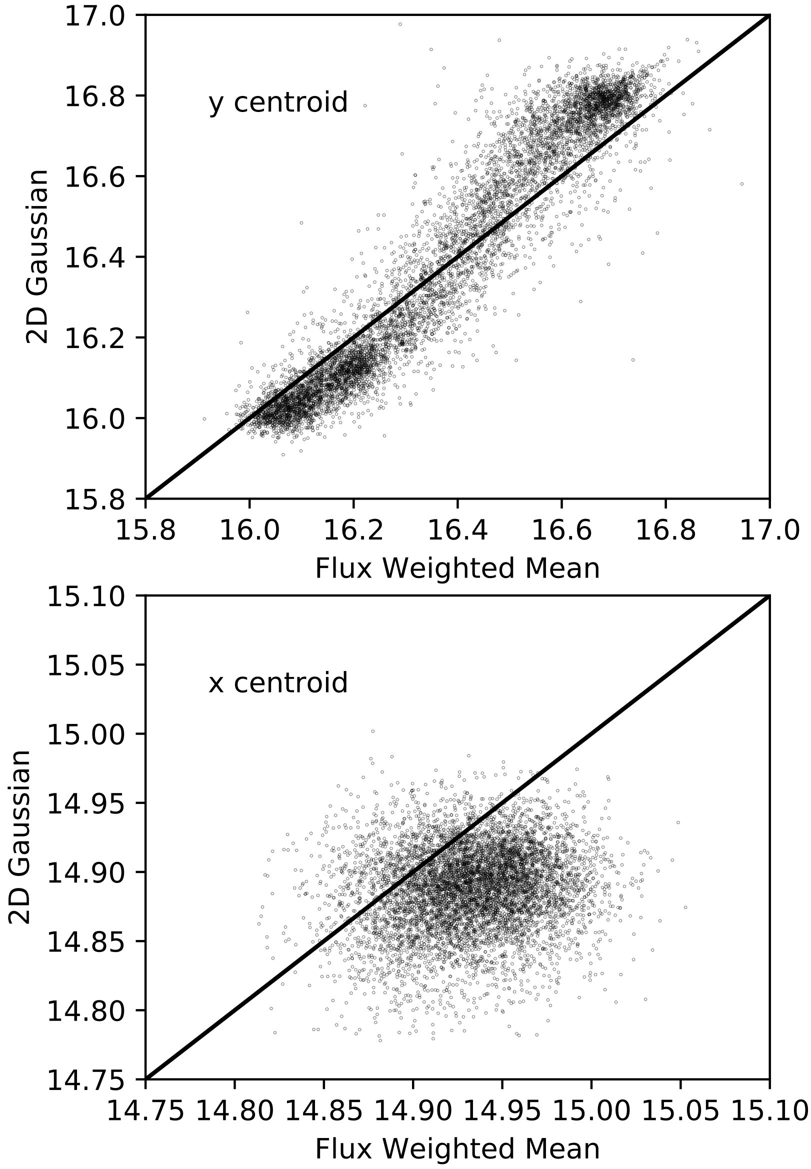

Figure 4.1: Centroid locations, in pixels, for the 3.6 μm observations, computed using two different algorithms. (The behaviour is qualitatively similar for 4.5 μm observations.) The black line is what we would expect if both algorithms gave the same centroid values. Most of the telescope drift is in the y direction. Although both centroiding schemes give similar raw flux, the centroid locations differ significantly, indicating that the PSF shape and asymmetry change over the course of the observation.

Most POET analyses have used Gaussian centroiding, with 5× interpolated aperture photometry (Stevenson et al., 2017; Kreidberg et al., 2018; Mansfield et al., 2020a). The metric to pick the aperture size is slightly different than SPCA: with POET, we selected the aperture size that minimized the standard deviation of the normalized residuals (SDNR) of the phase curve fit. For the 4.5 μm observations this was a 2.0 pixel radius moving aperture, and for 3.6 μm it was a 2.25 pixel radius moving aperture. The reason for the different preferred aperture sizes between SPCA and POET is because POET used interpolated photometry, and because the metric to select the aperture size is different between the two pipelines. Regardless, we get qualitatively similar raw flux using both pipelines. The median background levels are 17% and 4%, respectively, of the median flux uncertainty at Channels 1 and 2 for our preferred aperture sizes.

4.5 Modeling the Phase Curve

The observed flux variations of the system consist of two parts: the astrophysical signal of interest, and detector systematics. We modeled and fit for these simultaneously, as

$$F_{\text{model}}(t) = A(t) \times \tilde{D}(t), \tag{4.1}$$

where $A(t)$ represents the astrophysical signal, and $\tilde{D}(t)$ is the normalized detector model.

The astrophysical signal itself has the form

$$A(t) = F_*(t) + F_p(t), \tag{4.2}$$

where $F_*(t)$ is the stellar flux, and $F_p(t)$ is the planetary signal. With SPCA we used BATMAN (Kreidberg, 2015) to model the occultations —transits and secondary eclipses— assuming a quadratic limb darkening law. The apparent stellar brightness is

$$F_\star(t) = T(t), \tag{4.3}$$

where $T(t)$ is the transit light curve. Outside of transit, we assume that the stellar flux is constant.

The planetary flux ratio is

$$F_p(t) = F_{\text{day}}\Phi(\psi(t)), \tag{4.4}$$

where F_{day} is the secondary eclipse depth, $\Phi(\psi(t))$ is the phase variation of the planet, and $\psi(t)$ is the orbital phase, given by $\psi(t) = 2\pi\left(t - t_e\right)/P$ where t_e is the time of secondary eclipse, and P is the orbital period of the planet. Reflected light is negligible in the IRAC bandpasses, so we assume any light coming from the planet is thermal emission. We modelled the thermal phase variations as

$$\Phi(\psi) = 1 + C_1(\cos(\psi) - 1) + C_2\sin(\psi), \tag{4.5}$$

and imposed a prior that both the phase curve and the implied brightness map must be non-negative (Cowan and Agol, 2008; Keating and Cowan, 2017). We kept P fixed to 1.4200242 days (Collins et al., 2017).

With POET, we modelled the phase variations in an equivalent way:

$$\Phi(t) = 1 + C_1\cos\left[\frac{2\pi(t - t_e)}{P}\right]. \tag{4.6}$$

We tested higher order sinusoids, but found that including them led to overfitting. We also tested fits with and without an additional linear trend in time, which can account for additional instrumental systematics or stellar variability.

4.5.1 Detector Systematics

The detector systematics, $\tilde{D}(t)$, are primarily due to intrapixel sensitivity variations. With SPCA, we considered two methods that use the flux centroid locations to model the sensitivity of the detector. The first was to fit an n-th degree 2D polynomial, as a function of the x and y position of the centroids. We tested polynomials with order 2 through 7, and used the Bayesian Information Criterion (BIC) to select the best model—the one that fits the data best without overfitting (Schwarz, 1978).

The second detector model we used was BiLinear Interpolated Subpixel Sensitivity (BLISS) mapping, a non-parametric detector model. BLISS has been used successfully to analyze many phase curves (Stevenson et al., 2014, 2017; Kreidberg et al., 2018; Beatty et al., 2019; Bell et al., 2019; Mansfield et al., 2020a) and performed well in the *Spitzer* data challenge (Ingalls et al., 2016).

We fit several combinations of detector models and astrophysical signals to the observations in each channel. First, we used Levenberg-Marquardt optimization to find the best-fit parameters, and then sampled parameter space using a Markov-Chain Monte-Carlo to obtain error estimates. We computed the BIC, and used this to select the preferred astrophysical model.

Because BLISS calculates the detector sensitivity directly, rather than letting sensitivity vary as a jump parameter, it cannot be directly compared to the polynomial models using the BIC. However, the BIC can be used to select the preferred astrophysical model for a given BLISS implementation.

We also tested pixel-level decorrelation (PLD), which does not explicitly assume a functional form for the detector sensitivity and does not use centroids (Deming et al., 2015). Although first-order PLD is inadequate when the stellar centroid moves more than about 0.1 pixel, second-order PLD has been used successfully for phase curve observations (Zhang et al., 2018; Bell et al., 2019). In both of our observational channels the centroids move by nearly a pixel over the course of the observation, so we implemented second-order PLD. As PLD is parametric, it can be directly compared to the polynomial model using BIC.

For the POET analyses, we used a BLISS detector model. Because BLISS is non-parametric, it is flexible and has the advantage of running quickly in a Monte Carlo.

Lastly, because of the differences in photometry and sigma-clipping between pipelines, the respective datasets are not exactly the same between the two analyses. There is no perfect way to compare analyses between two different pipelines. One way is to compare which one of them gives the lowest fit residuals, and another is to compare the log-likelihoods per datum of the models (Bell et al., 2019).

4.5.2 Binning

Some phase curve analyses have fitted binned data while others have fitted the unbinned data. There are arguments for and against binning. Binning data before fitting filters

Table 4.2: Summary of key light curve parameters for both wavelengths. Our fiducial analysis is the POET fit to the unbinned data using a BLISS detector model, as it produced the smallest fit residuals.

Wavelength	Eclipse Depth (%)	$R_p/R_\star$	Amplitude (ppm)	Phase Offset	$T_{\mathrm{bright,day}}$ (K)	$T_{\mathrm{bright,night}}$ (K)
3.6 μm	0.21 ± 0.01	0.144 ± 0.001	660 ± 91	$11° \pm 7°$	1542^{+32}_{-31}	1167^{+69}_{-74}
4.5 μm	0.30 ± 0.02	0.145 ± 0.001	918 ± 114	$-4° \pm 7°$	1557^{+35}_{-36}	1117^{+76}_{-71}

out high frequency noise, improves centroid position accuracy, and makes the fits run faster, among other advantages (Deming et al., 2015). However, it can also distort the light curve shape if the bin size is too large (Kipping, 2010). Binning can also smooth over short timescale telescope pointing variations. To date, there has been no systematic study of the effects of bin size on retrieved phase curve shapes. There is some preliminary evidence, however, that coarse binning yields phase curve shapes discrepant with results from fitting unbinned data. This effect will be fully explored in upcoming work (May et al. 2020, in prep.)

Fitting unbinned data with SPCA was prohibitively slow, especially when testing multiple model combinations and higher order polynomial and PLD models. Therefore we binned the observations by datacube (64 frames, or 128 s) which is much shorter than the occultations, and equal to the bin sizes used in previous work with SPCA (Dang et al., 2018; Bell et al., 2019).

With POET we were able to fit the entire unbinned dataset, because POET is optimized to run with multiprocessing. Best-fit parameters and uncertainties from the two pipelines are shown in Tables 4.3 and 4.4.

4.6 Results

The intrapixel sensitivity variations are less severe for the 4.5 μm channel and typically easier to fit than the 3.6 μm channel, so we begin by summarizing the 4.5 μm results. See Table 4.2 for a summary of the fiducial light curve parameters at both wavelengths.

4.6.1 4.5 μm Observations

To see if using different centroid algorithms affected the fitted parameters, we fit the photometry obtained from both algorithms with SPCA. The flux weighted mean (FWM) centroiding gave lower scatter in the residuals, as well a higher log-likelihood than Gaussian centroiding. A first order sinusoid, and no linear slope, was the preferred astrophysical model. All combinations of detector models and centroiding algorithms produced consistent eclipse depths within the error bars. In all the fits we tried, we found a slight westward phase offset. The phase curve using the second order polynomial detector model is shown in the righthand column of Figure 4.2.

Our POET analysis used a BLISS detector model. We selected the knot spacing such that bilinear interpolation performed better than nearest neighbour interpolation (Stevenson et al., 2012a), which was 0.019 pixels in each direction. Again we found that a first order sinusoid, with no linear slope, gave the lowest BIC and lowest residuals in the final fit compared to other astrophysical models. We attempted decorrelating against the PSF width, but it gave a higher BIC for this wavelength.

The POET analysis yielded an eclipse depth consistent with the SPCA analysis, as well as a slightly westward phase offset of $-4° \pm 7°$, and lower residuals in the final fit (see Figure 4.2). The residuals were 1.11 greater than the photon noise limit. There was little red noise in the final fit (Figure 4.4). Using the phase curves fluxes, we get a dayside brightness temperature of 1557^{+35}_{-36} K, and a nightside brightness temperature of 1117^{+76}_{-71} K.

4.6.2 3.6 μm Observations

For the 3.6 μm phase curve observations, we also tried fitting photometry using both centroiding algorithms. We again experimented with different combinations of detector polynomial orders and astrophysical models. For this channel only, decorrelating against the PSF width resulted in a dramatically lower BIC for all the polynomial and BLISS fits we tried, with both SPCA and POET. For the flux weighted mean photometry, a second order polynomial gave a lower BIC than higher orders. For the 2D Gaussian photometry,

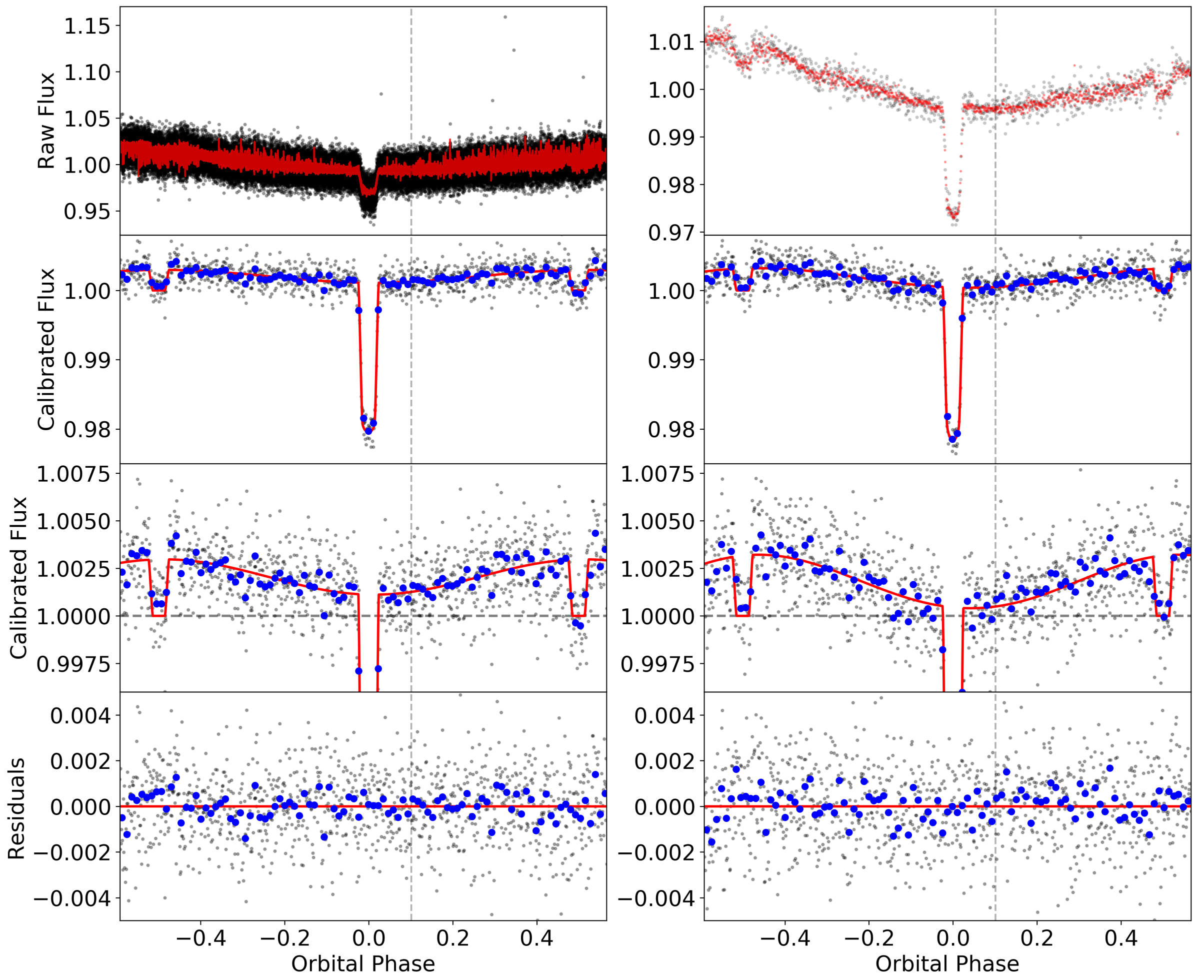

Figure 4.2: *Left:* Raw photometry and light curve model for the 4.5 μm observations of Qatar-1b using the POET pipeline. We fitted the unbinned dataset, shown in black in the top panel, but bin the data by datacube when plotting below for clarity. *Right:* Results from the SPCA pipeline. The best fit combined astrophysics $\times$ detector model for each pipeline is shown in red in the top panels. The grey dots come from binning the data by datacube (64 frames), and the blue dots are more coarsely binned. The red line is the final best fit model for each. The two middle panels show the best-fit astrophysics model, with the detector systematics removed. The bottom panels show the residuals of the best-fit light curve and detector systematics models subtracted from the raw signal. The dashed line indicates where the Astronomical Observing Request break occurs.

we tried polynomial orders from two to seven, and found that a sixth order polynomial gave the lowest BIC among the polynomial models.

Unlike for the 4.5 μm observations, the eclipse depths did not agree for the reductions using different centroiding algorithms. The eclipse depths from the flux weighted mean photometry were twice as deep as those using Gaussian centroiding or the one reported

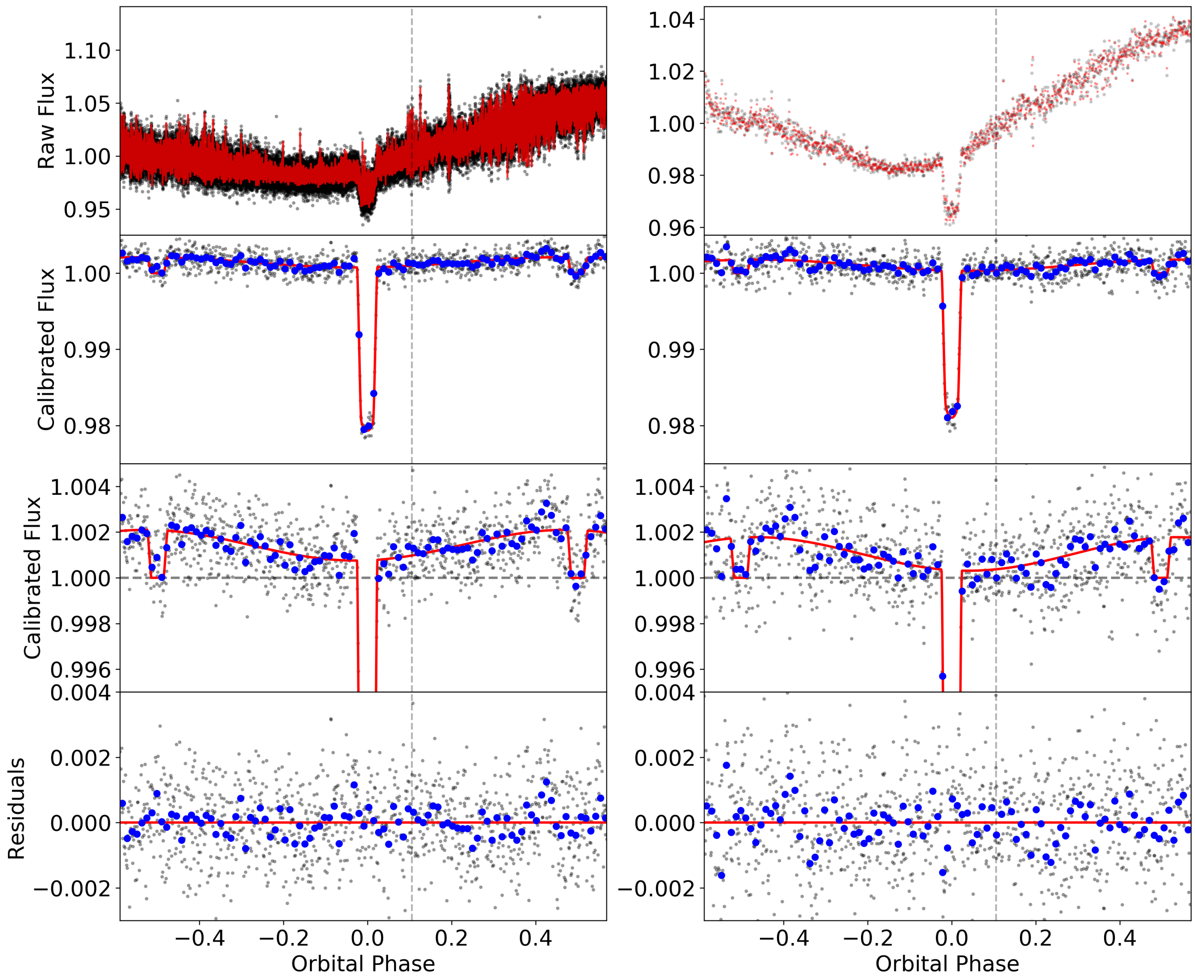

Figure 4.3: The same figure as Figure 4.2 but for the 3.6 μm observations.

by Garhart et al. (2018). The likelihoods were lower, and the residuals were higher, than the fits to the Gaussian centroiding photometry. Gaussian centroiding also gave lower scatter in the raw photometry and centroids. For these reasons we chose the Gaussian centroiding photometry as our fiducial dataset for the SPCA fits.

We also saw a discrepancy between the different detector models: the polynomial and BLISS models gave consistent eclipse depths to one another but the phase offsets are 2.5σ discrepant. With BLISS, an eastward phase offset was favoured, but with the polynomial detector model, a westward offset was favoured. BLISS gave a higher likelihood and lower residuals than the polynomial fit.

Because of the discrepancy in the inferred parameters, we tried a centroid-agnostic detector model: a second-order PLD using a 5×5 grid of pixels. We performed the decorrelation using the individual pixel fluxes, but used the 2D Gaussian aperture pho-

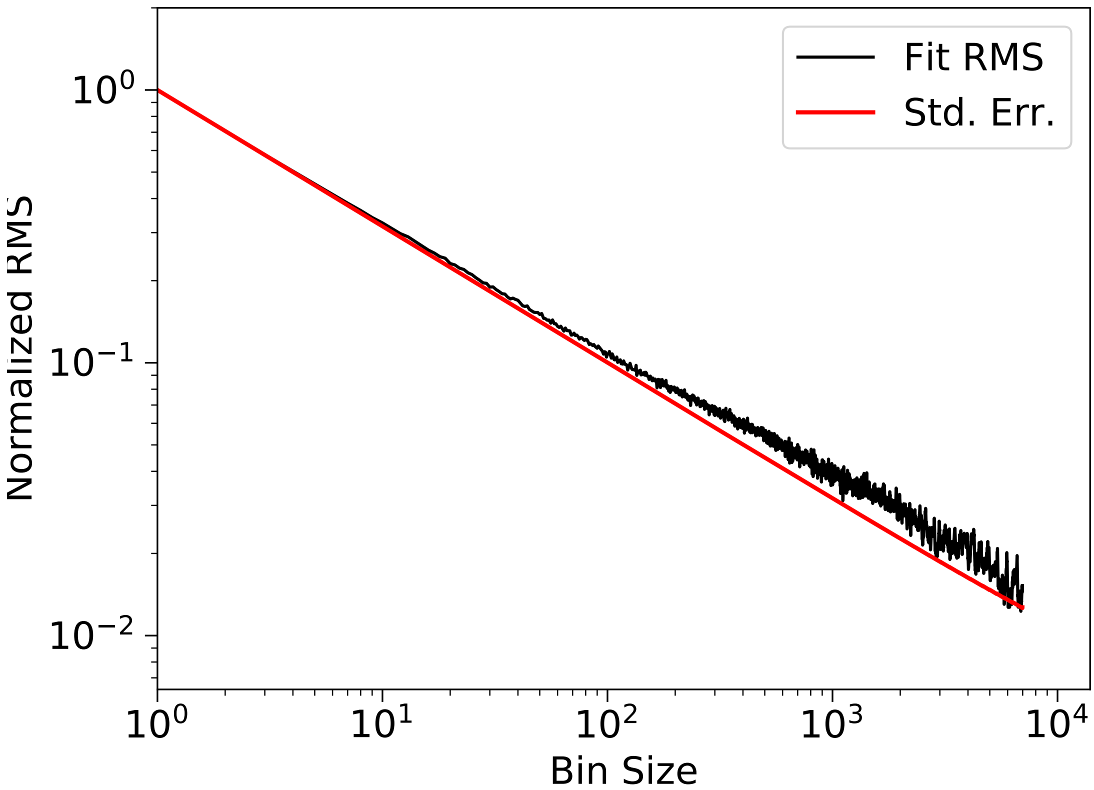

Figure 4.4: Root-mean-squared residuals versus bin size for the 4.5 μm phase curve fit with POET. The red line is the expected behaviour assuming white noise.

tometry as our dataset, rather than the sum of pixels, in keeping with past analyses (Deming et al., 2015; Zhang et al., 2018; Bell et al., 2019). PLD performed better than the polynomial models, achieving a higher log likelihood, lower BIC, and lower residuals in the final fit. The fitted phase curve is shown in the righthand column of Figure 4.3. The PLD fit gave a phase curve offset consistent with that of the sixth order polynomial fit.

Our POET analysis again used a BLISS detector model, with an ideal knot spacing of 0.012. A first order sinusoid, with a linear ramp, and a fit to the PSF width was the preferred model. The fit is shown in the left panel of Figure 4.3. We found an eastward offset of $11° \pm 7°$. This is 2.3σ away from the offset found with SPCA. Because the POET analysis used the full, unbinned dataset, and yielded lower residuals than SPCA, we take that as our fiducial analysis for the rest of this paper. The residuals were 1.16 times greater than the photon noise limit. The final fit removed most of the red noise

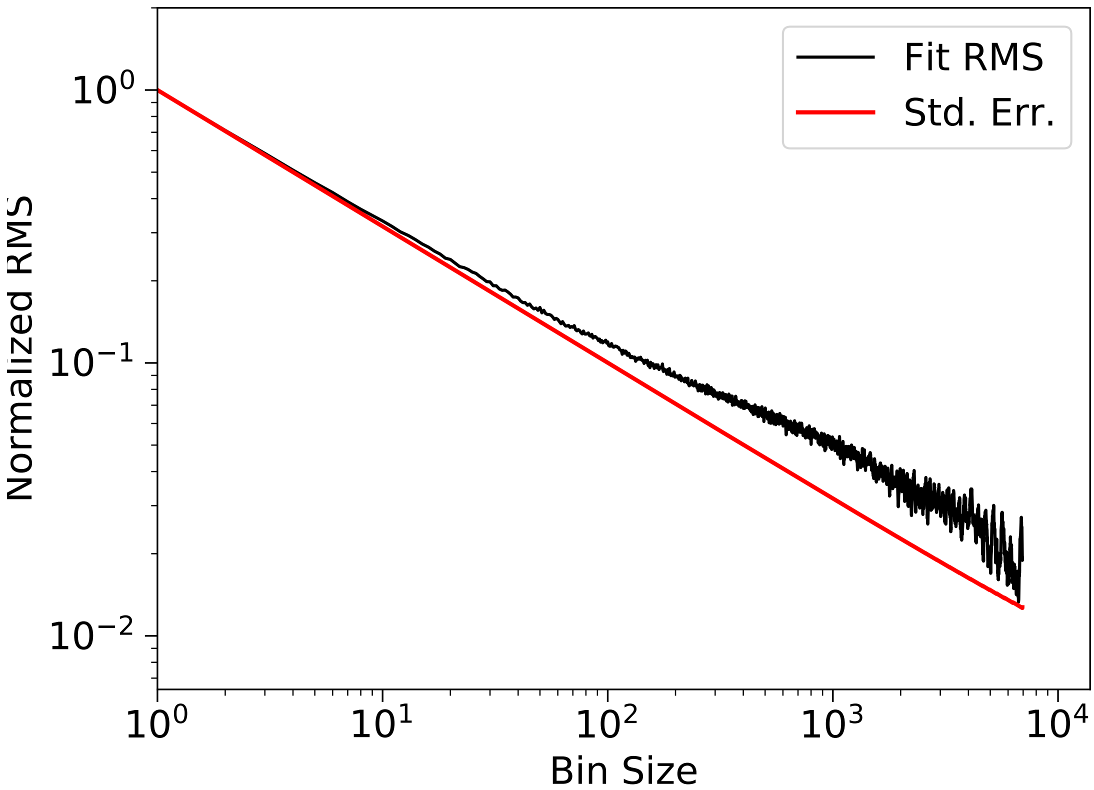

Figure 4.5: The same plot as fig. 4.4 but for the 3.6 μm phase curve.

(Figure 4.5). The dayside and nightside brightness temperatures are 1542^{+32}_{-31} K, and 1167^{+69}_{-74} K.

4.7 Discussion

The two main observational quantities calculated from thermal emission phase curves are the amplitude of variations, and the phase at which the peak flux occurs. These

Table 4.3: Comparison of the best 4.5 μm phase curve fit for each pipeline. SDNR stands for standard deviation of the normalized residuals, for which we show the residuals binned by datacube (128 s) for both fits. The fit using the POET pipeline gave the lowest residuals. The transit and eclipse depths are consistent within 1σ between both analyses, but the phase offsets and amplitudes are not.

Pipeline	Centroids	Bin Size	Detector	Eclipse Depth (%)	$R_p/R_\star$	Amplitude (ppm)	Offset	SDNR (ppm)
POET	Gaussian	2s	BLISS	0.30 ± 0.02	0.1453(8)	918 ± 114	$-4° \pm 7°$	1140
SPCA	FWM	128s	Poly 2	0.31 ± 0.02	0.146(1)	1336 ± 101	$-17° \pm 4°$	1660

Table 4.4: The same as Table 4.3 but for 3.6 μm The transit depths and phase amplitudes are consistent within 1σ between both analyses, but the transit depths and phase offsets are not.

Pipeline	Centroids	Bin Size	Detector	Eclipse Depth (%)	$R_p/R_\star$	Amplitude (ppm)	Offset	SDNR (ppm)
POET	Gaussian	2s	BLISS	0.21 ± 0.01	0.1443(6)	660 ± 91	$11° \pm 7°$	857
SPCA	Gaussian	128s	PLD 2	0.18 ± 0.02	0.137(1)	675 ± 134	$-22° \pm 18°$	1448

are, respectively, measures of the temperature differences between the day and night hemispheres of the planet, and the ability of the planetary winds to advect hot gas away from the substellar point before it can cool. There is a large body of literature examining expectations for hot Jupiter atmospheric circulation patterns and how these physics translate into observed thermal phase curves (e.g. see reviews by Parmentier and Crossfield (2018) and Heng and Showman (2015)). In a comprehensive study, Komacek et al. (2017) show that to first order, the day-night contrast on a planet should increase with increasing equilibrium temperature and the hottest region of the planet should be closer to the substellar point (i.e., smaller phase offsets). Higher order effects include the planet's rotation rate and its gravity. Moreover, if the rotation rate is too slow, it can disrupt the circulation pattern, breaking the predicted trends (Rauscher and Kempton, 2014).

Any sources of drag in an atmosphere can slow down the winds, leading to smaller bright-spot offsets (Komacek et al., 2017). One obvious culprit for hot Jupiters is magnetic drag. If a planet is hot enough for thermal ionization and has an appreciable magnetic field, then ions in the atmosphere can interact with the magnetic field, acting as a source of drag. All else being equal, the effective drag strength should increase with increasing stellar irradiation (Perna et al., 2010), but it depends on magnetic field strength and metallicity. Magnetic drag could directly impact atmospheric circulation.

Clouds can also directly affect the atmospheric circulation through feedback with the temperature and wind structures themselves. They can also influence the phase curves by disconnecting the emitted flux from the temperature structure (Roman and Rauscher, 2019). When clouds are thick enough to provide significant scattering, it becomes important to model their effects within a GCM simulation rather than post-processing. If the clouds are so thin that feedback is not important, Parmentier et al. (2016) predict that clouds should lead to observable trends in *Kepler* phase curve shapes as a function of equilibrium temperature.

By comparing thermal phase curves of planets with similar equilibrium temperatures, such as Qatar-1b, HD 209458b, and WASP-43b, any differences can be attributed to differences in circulation efficiency, due to differences in rotation, gravity, atmospheric drag, or clouds.

4.7.1 Temperatures and Energy Budget

First we consider the energy budget of Qatar-1b and compare it to HD 209458b and WASP-43b. By combining brightness temperatures at several wavelengths, it is possible to estimate the total bolometric flux emitted by a given hemisphere of a planet; this can be quantified by an effective temperature of the hemisphere. We estimated the dayside and nightside effective temperatures of Qatar-1b using Gaussian process regression, which was shown to give more robust temperature estimates than using the error weighted mean or linear interpolation (Pass et al., 2019).

The dayside effective temperature of Qatar-1b is 1588 ± 73 K, and the nightside effective temperature is 1163 ± 79 K. These include the systematic error introduced when converting from brightness temperatures to an effective temperature (Pass et al., 2019). Using these estimates, we obtain a Bond albedo of $0.12^{+0.14}_{-0.16}$ and a day-to-night heat recirculation efficiency of $0.52^{+0.12}_{-0.11}$ (Cowan and Agol, 2011a), confirming that Qatar-1b does in fact circulate heat from day to night. The heat recirculation efficiency is consistent with the value of $0.51^{+0.15}_{-0.13}$ for HD 209458b (Keating et al., 2019). The heat recirculation efficiency of WASP-43b is debated. It was initially reported to be negligible: $0.002^{+0.01}_{-0.002}$ (Stevenson et al., 2017), but demanding that the brightness map of WASP-43b be strictly positive gave a much higher value of 0.51 ± 0.08 (Keating and Cowan, 2017). Using the reanalyzed, non-negative phase curves of Mendonça et al. (2018) gives a heat recirculation efficiency of $0.27^{+0.12}_{-0.11}$ (Keating et al., 2019).

We plot the dayside and nightside temperatures along with those of all other hot

Jupiters with full-orbit infrared phase curves in Figure 4.6. The nightside temperature of Qatar-1b is in line with the trend that hot Jupiters all have nightside temperatures of approximately 1100 K, likely due to nightside clouds (Keating et al., 2019; Beatty et al., 2019), which are predicted to be ubiquitous on hot Jupiters (Parmentier et al., 2016). Ultra-hot Jupiters, with irradiation temperatures greater than about 3500 K, have hotter nightsides due to additional heat transport from hydrogen dissociation and recombination. For instance, the ultra-hot Jupiter KELT-9b is so irradiated that nothing can condense, even on its nightside (Mansfield et al., 2020a).

4.7.2 Phase Offsets

We detected no phase offset at 4.5 μm ($4 \pm 7°$, westward). This stands in stark contrast to the eastward offsets of $40 \pm 6°$ and $21.1 \pm 1.8°$ for HD 209458b and WASP-43b, respectively, at the same wavelength (Zellem et al., 2014; Stevenson et al., 2017). Two reanalyses of WASP-43b at 4.5 μm also found eastward phase offsets, of $12 \pm 3°$ (Mendonça et al., 2018) and $11.3 \pm 2.1°$ (Morello et al., 2019).

At 3.6 μm we detected a phase offset of $11 \pm 7°$ (eastward). This is consistent with the result of $12.2 \pm 7°$ for WASP-43b (Stevenson et al., 2017). The reanalyzed 3.6 μm offsets of WASP-43b are $3 \pm 2°$ (eastward) (Mendonça et al., 2018) and $5.6 \pm 2.7°$ (eastward) (Morello et al., 2019). The offsets we observed for Qatar-1b in both channels are on opposite sides of the substellar point, but are just 1.5σ away from one another. We plot the phase offsets for Qatar-1b with the *Spitzer* phase curve offsets for the whole suite of hot Jupiters in Figure 4.7, and plot the phase offsets of Qatar-1b with all published phase offsets of WASP-43b and HD 20945b in Figure 4.8.

The planet CoRoT-2b was the first hot Jupiter with a robustly detected westward phase curve offset (Dang et al., 2018). The offset was $21 \pm 4°$ west at 4.5 μm. A 3.6 μm phase curve was not observed. The authors suggested three scenarios to cause the westward offset: non-synchronous rotation, magnetic effects, or eastern clouds.

Like other hot Jupiters, Qatar-1b is expected to be tidally locked into synchronous rotation (Showman and Guillot, 2002). However, if it was not synchronously rotating,

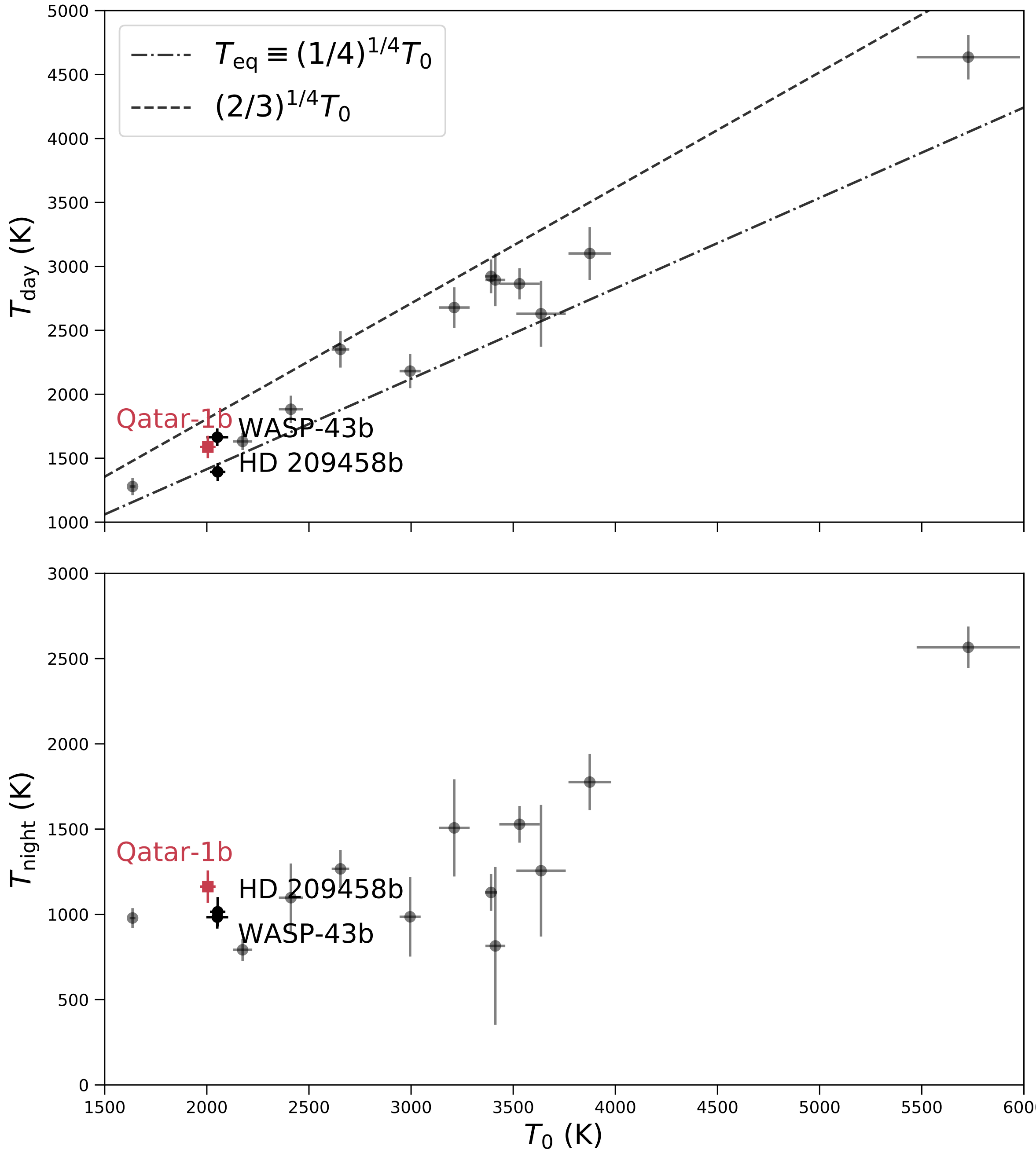

Figure 4.6: An updated version of the dayside (top panel) and nightside (bottom panel) temperatures plot from Keating et al. (2019), including Qatar-1b and KELT-9b (Mansfield et al., 2020a). Qatar-1b, HD 209458b, and WASP-43b are shown as opaque points. The horizontal axis is the irradiation temperature, $T_0 \equiv T_\star\sqrt{R_\star/a}$. On the top panel we also plot the equilibrium temperature $T_{\rm eq} \equiv (1/4)^{1/4}T_0$ (dashed-dotted line), and the dayside temperature in the limit of no heat transport: $(2/3)^{1/4}T_0$ (dashed line). Qatar-1b is plotted with a square marker, and fits the trend that hot Jupiters have nightside temperatures around 1100 K. Ultra-hot Jupiters, planets with irradiation temperatures above $\sim$3500 K, have hotter nightsides due to heat transport from hydrogen dissociation and recombination.

GCM simulations suggest Qatar-1b could have a reduced eastward offset or even westward offset (Showman et al., 2009; Rauscher and Kempton, 2014). Either way, we would expect to see the same direction of phase offset in both channels.

Magnetic drag can also reduce eastward phase offsets, or produce westward offsets (Rauscher and Menou, 2013; Hindle et al., 2019). At high enough equilibrium temperatures, alkali metals in a planet's atmosphere thermally ionize and interact with the planet's magnetic field, acting as a source of drag. The ultra-hot Jupiter WASP-18b was found to have a small phase offset in its Wide Field Camera 3 phase curve, which the authors attributed to magnetic drag (Arcangeli et al., 2019). Magnetic interactions can also cause phase offsets to periodically change from east to west (Rogers, 2017). Such a temporal change in phase offset was observed in *Kepler* phase curves of HAT-P-7b (Armstrong et al., 2016), and the 3.6 μm phase curve of WASP-12b (Bell et al., 2019).

Qatar-1b's equilibrium temperature is below the threshold where magnetic effects are expected to be significant (Menou, 2012), but its host star has a higher metallicity than HD 209458 and WASP-43. A higher stellar metallicity may a suggest a larger number of trace metals in the planetary atmosphere, resulting in a more strongly ionized atmosphere. Magnetic field strengths of hot Jupiters are unknown, but could potentially be orders of magnitude higher than Jupiter (Yadav and Thorngren, 2017). High metallicities and strong planetary magnetic fields can decrease the threshold for magnetic drag effects to become important (Menou, 2012).

The large uncertainty on the 4.5 μm phase curve offset means it is also consistent with a negligible eastward offset. This may be evidence of magnetic drag. Otherwise, if the phase curve offsets at both wavelengths are truly on opposite sides of the substellar point, this could be evidence of magnetic variability on the timescale of about five days (the time between the observations). If magnetic drag is reducing the wind speed, then deep transport is needed to move heat to the nightside.

Dayside clouds could also cause reduced eastward phase offsets, westward offsets, or variable offsets. The reflected optical phase curve of the planet Kepler-7b has a westward offset, best explained by westward clouds (Demory et al., 2013; Roman and Rauscher,

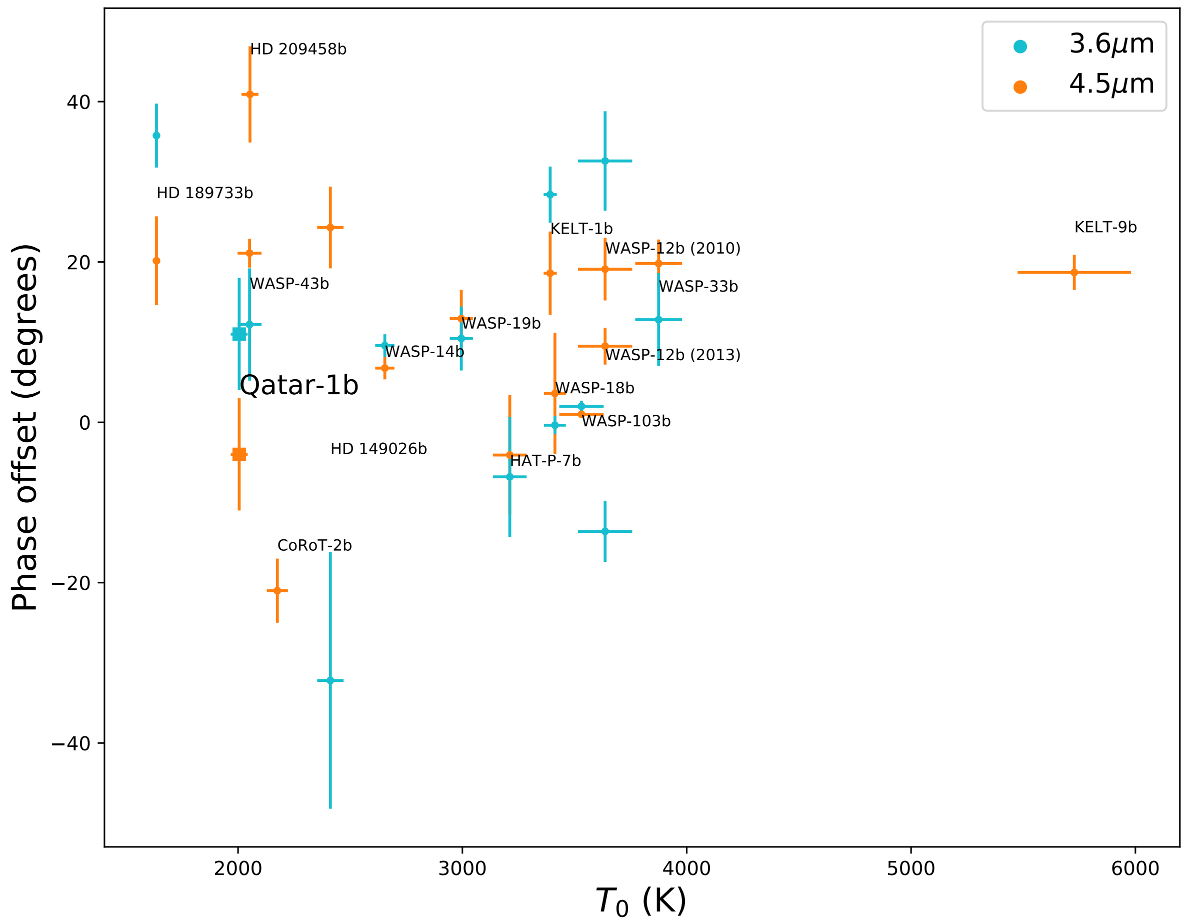

Figure 4.7: Phase offsets for all hot Jupiters with full-orbit phase curves. Qatar-1b is denoted with a square marker.

2017). In the infrared, a westward offset could be caused by eastward clouds (Dang et al., 2018), although cloud models do not generally predict this. Optically thick dayside clouds could simply be obscuring the transported heat of Qatar-1b, leading to negligible phase offsets in both channels. The dayside brightness temperatures are the same at both wavelengths, consistent with blackbody emission from an optically thick cloud deck. Time variable cloud coverage could also cause bright-spot variations, similar to the variability seen for brown dwarfs.

The presence or lack of clouds can be tested by measuring the albedo at optical wavelengths, using the UVIS mode of the Wide Field Camera 3 instrument on board the *Hubble Space Telescope*. Optical phase curves, such as one from the Transiting Exoplanet Survey Satellite (TESS), could also measure the offset at visible wavelengths. TESS has already observed the phase curve of Qatar-1b, so it could be analyzed as has been done

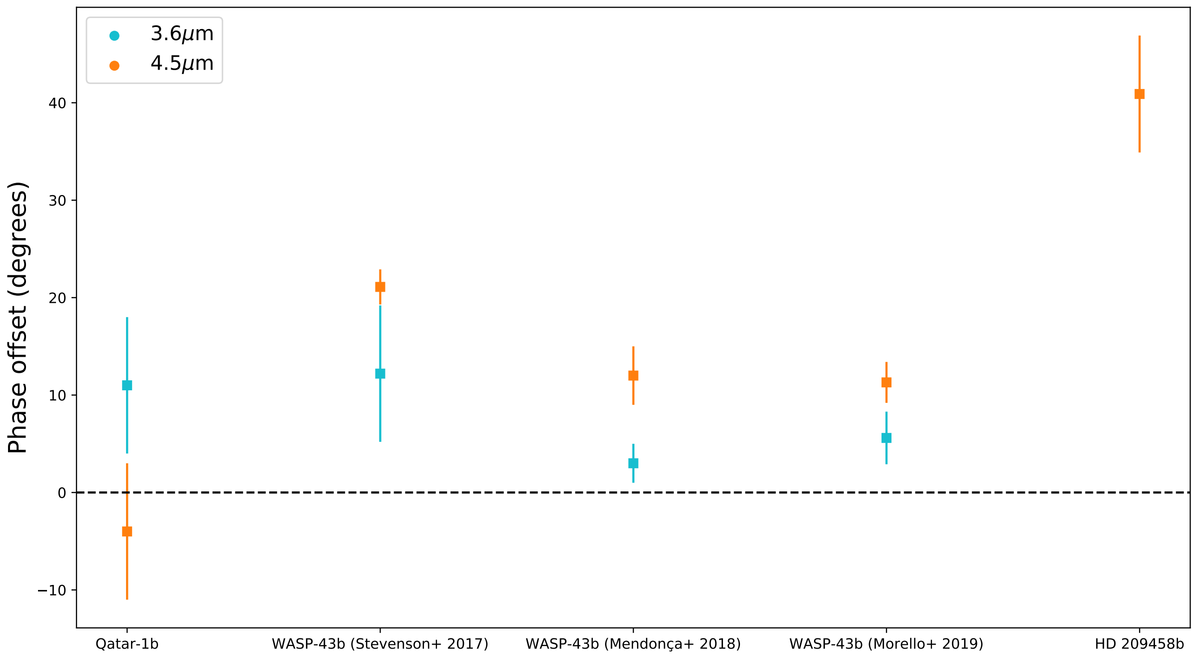

Figure 4.8: Phase offsets for just Qatar-1b, WASP-43b, and HD 209458b using all currently published values (Zellem et al., 2014; Stevenson et al., 2017; Mendonça et al., 2018; Morello et al., 2019).

for some hotter planets (Shporer et al., 2019; Wong et al., 2020a,b; Bourrier et al., 2020; Daylan et al., 2019).

Overall, Qatar-1b makes an interesting target for the *James Webb Space Telescope* (JWST), especially as a comparison to WASP-43b, which will be observed extensively by JWST as part of Early Release Science and Guaranteed Time Observations (Bean et al., 2018). The upcoming ARIEL mission will also be able to measure spectroscopic phase curves at a similar range of wavelengths as JWST (Tinetti et al., 2018) and potentially probe time variability.

4.8 Conclusion

We presented full-orbit infrared phase curves of Qatar-1b taken with the *Spitzer* space telescope at 3.6 μm and 4.5 μm. We summarize our results below.

- The dayside brightness temperatures are the same at both wavelengths.
- The nightside brightness temperatures are the same at both wavelengths, and follow

the trend that hot Jupiters have the same nightside temperatures (Keating et al., 2019; Beatty et al., 2019).

- Qatar-1b circulates a moderate amount of heat from day to night, similar to HD 209458b, but has a higher recirculation efficiency than WASP-43b. The three planets all receive the same amount of stellar irradiation.

- The bright-spot offsets for the two phase curves of Qatar-1b are consistent with zero. They stand in contrast to the significant eastward hotspot offsets predicted by GCMs and observed for HD 209458b and WASP-43b. The three planets all receive the same amount of stellar irradiation, so this discrepancy points to the importance of secondary parameters like rotation rate, gravity, or metallicity in determining their atmospheric conditions. Some physical mechanisms to produce the small offsets for Qatar-1b are subsynchronous rotation, magnetic effects, or dayside clouds, but there is so far no strong evidence for any of these.

- Qatar-1b is an attractive target for the JWST and ARIEL missions, especially as a comparison to WASP-43b which will be observed extensively. In the meantime, *Hubble* UVIS observations may be able to test the dayside cloud hypothesis, as would an analysis of the TESS optical phase curve.

4.9 Acknowledgments

This work is based on observations made with the Spitzer Space Telescope, which is operated by the Jet Propulsion Laboratory, California Institute of Technology under a contract with NASA. D.K., N.B.C., T.J.B., and L.D. are affiliated with, and supported by, the McGill Space Institute, the Institute for Research on Exoplanets, and the Centre for Research in Astrophysics of Québec. J.M.D acknowledges the European Research Council (ERC) European Union's Horizon 2020 research and innovation programme (grant agreement no. 679633; Exo-Atmos) and the Amsterdam Academic Alliance (AAA) Program.

Software: astropy (The Astropy Collaboration 2013, 2018), matplotlib (Hunter 2007), Scipy (Jones et al. 2001), POET (Stevenson et al. 2012; Cubillos et al. 2013), SPCA (Dang et al. 2018; Bell et al. 2019)

4.10 Epilogue

Qualitatively, the results were similar between the two reductions but there were still discrepancies between some of the best-fit parameters. This suggests that although eclipse depths seem to be robust between pipelines (Ingalls et al., 2016), trends across planets whose phase curves were analyzed with disparate pipelines could have additional variance due to discrepancies between the various photometry techniques, detector systematics models, and MCMC algorithms used.

This was part of the motivation behind the wholesale reduction and reanalysis of the suite of published 4.5 μm *Spitzer* phase curves by (Bell et al., 2020), using the SPCA pipeline. The best-fit parameters from their reanalysis of Qatar-1b agreed with the fiducial analysis from this Chapter within 2σ. Along with the large uniform secondary eclipse survey from Garhart et al. (2020), it is clear that hot Jupiter atmospheric characterization is moving towards these types of uniform analyses. The next Chapter will present a complementary technique that leverages the power of cutting-edge Bayesian statistics to share information across observations of separate planets.

5 Atmospheric characterization of hot Jupiters using hierarchical models of Spitzer observations

5.1 Prologue

Hierarchical modelling is a way of sharing information across separate sets of observations by fitting them simultaneously, and accounting for higher level structure in the data. The work in this Chapter is the first application of hierarchical modelling to atmospheric characterization of hot Jupiters. This Chapter demonstrates two applications: fitting repeated *Spitzer* secondary eclipse observations of the same planet, and fitting secondary eclipses from multiple planets. In both cases, hierarchical modelling gives more precise estimates of secondary eclipse depths than analyzing the observations separately. Testing the technique on *Spitzer* data allows us to set the stage for next-generation missions.

5.2 abstract

The field of exoplanet atmospheric characterization is trending towards comparative studies involving many planetary systems, and using Bayesian hierarchical modelling is a natural next step. Here we demonstrate two use cases. We first use hierarchical modelling to quantify variability in repeated observations by reanalyzing a suite of ten *Spitzer* secondary eclipse observations of the hot Jupiter XO-3b. We compare three models: one where we fit ten separate eclipse depths, one where we use a single eclipse depth for all ten observations, and a hierarchical model. By comparing the Widely Applicable Information Criterion of each model, we show that the hierarchical model is preferred over the others. The hierarchical model yields less scatter across the suite of eclipse depths—and higher precision on the individual eclipse depths—than does fitting the observations separately. We find that the hierarchical eclipse depth uncertainty is larger than the uncertainties on the individual eclipse depths, which suggests either slight astrophysical variability or that single eclipse observations underestimate the true eclipse depth uncertainty. Finally, we fit the suite of published dayside brightness measurements of 37 planets from Garhart et al. (2020) using a hierarchical model of brightness temperature vs irradiation temperature. The hierarchical model gives tighter constraints on the individual brightness temperatures than the non-hierarchical model. Although we tested hierarchical modelling on *Spitzer* eclipse data of hot Jupiters, it is applicable to observations of smaller planets like hot neptunes and super earths, as well as for photometric and spectroscopic transit or phase curve observations.

5.3 Introduction

Although the *Spitzer Space Telescope* wasn't designed for exoplanet science, it was a workhorse for the field (for a recent review, read Deming and Knutson, 2020). In particular, observations of exoplanet transits, secondary eclipses, and phase curves with *Spitzer's* Infrared Array Camera have been used to characterize the atmospheres of over a hundred transiting planets.

Substantial progress has been made towards a statistical understanding of exoplanetary atmospheres (Cowan and Agol, 2011a; Sing et al., 2016; Schwartz and Cowan, 2015; Schwartz et al., 2017; Parmentier and Crossfield, 2018; Zhang et al., 2018; Keating et al., 2019, 2020; Baxter et al., 2020; Bell et al., 2021). Many of the planets in these studies had been analyzed using disparate reduction and analysis pipelines, but researchers have started uniformly analyzing observations of multiple planets using a single pipeline. Garhart et al. (2020) independently reduced and analyzed 78 eclipse depths from 36 planets and found that hotter planets had higher brightness temperatures at 4.5 μm than at 3.6 μm. Bell et al. (2021) reanalyzed every available *Spitzer* 4.5 μm hot Jupiter phase curve using an open-source reduction and analysis pipeline, confirming several previously reported trends.

In this work we outline a complementary way to further the statistical understanding of exoplanet atmospheres: fitting measurements from multiple planets simultaneously using hierarchical models to robustly infer trends.

5.3.1 Spitzer Systematics

Exoplanet observations taken with *Spitzer*'s Infrared Array Camera (IRAC; Fazio et al., 2004) are dominated by systematics noise. The systematics are driven by intrapixel sensitivity variations on the detector and by now are well characterized (Ingalls et al., 2016). Detector systematics are typically fitted simultaneously with the astrophysical signal of interest. Each transit, secondary eclipse, and phase curve yields information about the IRAC detector sensitivity, but typically this information is not shared between observations.

Since the *Spitzer* systematics are a function of the centroid location on the pixel, efforts have been made to map the detector sensitivity independently using observations of quiet stars (Ingalls et al., 2012; Krick et al., 2020; May and Stevenson, 2020). The flux of a calibration star should be constant as a function of time, so any deviation must be due to the centroid moving across the detector as the telescope pointing drifts. A crucial assumption for this approach is that the *Spitzer* systematics do not vary with time, and that they are not dependent on the brightness of the star. Ingalls et al. (2012) and May and Stevenson (2020) approached the problem by explicitly calculating the detector sensitivity, while Krick et al. (2020) used a machine learning technique called random forests to look for patterns in the systematics.

Other approaches do not assume anything explicit about the detector sensitivity. Independent component analysis (Waldmann, 2012; Morello et al., 2014, 2016) separates the signal into additive subcomponents using blind source separation, with the idea being that one of these signals is the astrophysical signal. In another approach, Morvan et al. (2020) used the baseline signal before and after a transit to learn and predict the in transit detector systematics using a machine learning technique known as Long short-term memory networks.

In this work, we opted to parameterize and fit the detector systematics simultaneously with the astrophysical signal to account for any correlations between the two.

5.3.2 Hierarchical Models

Bayesian hierarchical models (Gelman et al., 2014) are routinely used in other fields because they offer a natural way to infer higher level trends in a dataset and can increase measurement precision. They are gaining traction in exoplanet studies: for example, to study the mass-radius (Teske et al., 2020) and mass-radius-period (Neil and Rogers, 2020) relations, and radius inflation of hot Jupiters (Sarkis et al., 2021; Thorngren et al., 2021). Hierarchical models have not yet been applied to atmospheric characterization of exoplanets.

There is one major difference between a typical Bayesian model and a hierarchical one. In a traditional Bayesian model, we estimate the probability distribution of our model parameters given our observed data and the prior probability of each model parameter. The prior distribution encodes our previous knowledge about the most likely values of the parameters and is specified before fitting the model. In a hierarchical model, however, the prior distributions themselves are parameterized using so-called hyperparameters. The hyperparameters become part of the model and are fitted simultaneously with the other parameters of interest. As we explain in the next section, this naturally represents how our intuition pools information across observations. It also helps to tame models by compromising between overfitting and underfitting.

Hierarchical models should be used whenever the data allow us to refine our knowledge of the prior distribution, which happens when a certain quantity is measured multiple times. A natural example in exoplanet science is repeated *Spitzer* observations of the same target. To demonstrate, we start with the archetypical suite of of ten *Spitzer* IRAC Channel 2 (4.5 μm) secondary eclipses of the eccentric hot Jupiter XO-3b (Wong et al., 2014). Below we explain the model and present our results. Afterwards, we show how we extend the model to fit multiple eclipses from different planets simultaneously and present results from fitting the eclipse data from Garhart et al. (2020) with a hierarchical model.

5.4 Hierarchical Model of XO-3b Eclipses

In the *Spitzer* data challenge, several groups analyzed ten secondary eclipses of XO-3b in order to test the repeatability and accuracy of various decorrelation techniques (Ingalls et al., 2016). The reduced archival data from the data challenge are publicly available, so we downloaded them rather than reducing them ourselves.

For XO-3b and other planets with repeated secondary eclipse observations, the eclipses have usually been fitted separately from one another, with a separate eclipse depth parameter for each observation (Ingalls et al., 2016; Kilpatrick et al., 2020). In other cases, a single eclipse depth parameter has been used to simultaneously fit multiple secondary eclipse measurements (Wong et al., 2014). This is also what is typically done for phase curves that are bracketed by two eclipses (Cowan et al., 2012; Bell et al., 2021).

However, neither approach quite matches what our intuition tells us. Because we are measuring the same thing each time, fitting the eclipse observations separately amounts to overfitting the individual observations, and fitting a single eclipse parameter amounts to underfitting all of the observations. If we observe one secondary eclipse, we would expect that the next one we observe would have a similar— but not identical— depth, due to measurement uncertainty, if not astrophysical variability. The second eclipse we observe would also change our beliefs about the first one. Each measurement of the planet's eclipse depth can be thought of as a draw from a distribution, with some variance. With enough measurements, the shape of this distribution can be inferred. A hierarchical model naturally takes all of this into account by fitting for the parameters that describe the higher level distribution simultaneously with the astrophysical signal of each observation.

Bayesian analysis requires us to specify priors on the parameters we are trying to infer. We can write down our prior on the ith eclipse depth as

$$D_i \sim \mathcal{N}(\mu, \sigma), \tag{5.1}$$

where we have used the tilde shorthand ($\sim$) to mean that the eclipse depth is drawn from a normal distribution centered on μ with a standard deviation of σ; μ and σ are hyperparameters. In a non-hierarchical model, we would specify μ and σ to represent our prior expectations of what D_i could be. After fitting, we would get a separate posterior distribution for each eclipse depth.

In a hierarchical model, we instead make μ and σ parameters and fit them simultaneously with the ten eclipse depths. We represent our beliefs about hyperparameters μ and σ with hyperpriors. This allows each eclipse observation to inform the others, by pulling the eclipse depths closer to the mode of the distribution of μ. This is known as Bayesian shrinkage. After fitting, we get a posterior distribution for each eclipse depth, as well as for μ and σ.

In the limit that σ goes to infinity, the hierarchical model is equivalent to the model with completely separate eclipse depths. Likewise when σ goes to zero, it is equivalent to the single eclipse depth model. A hierarchical model empirically fits for the amount of pooling based on what is most consistent with the observations.

5.4.1 Priors

Priors are necessary in a fit to encode prior knowledge, as well as to properly sample a model. In all cases, we use weakly informative priors rather than flat, "uninformative" priors. A flat prior is equivalent to saying that all values of eclipse depth are equally likely, even extremely large, unphysical values. Instead, we chose to place a normal prior with a large standard deviation so that we kept the predicted values within the right order of magnitude. Half-normal priors or wide normal priors are unlikely to introduce much bias into the parameter estimates and can make sampling more efficient. Flat priors are discouraged in practice because we usually have at least some vague knowledge of the range of values a parameter can take (Gelman et al., 2017).

5.4.2 Astrophysical Model

The astrophysical model for each observation was a secondary eclipse. We used STARRY (Luger et al., 2019) to compute the shape of each eclipse, with the depth and time of eclipse left as free parameters. We fixed the radius of the planet and host star, the orbital period, ratio of semi-major axis to stellar radius, orbital inclination, longitude of periastron and eccentricity to the literature values.

To get a rough upper limit on the eclipse depth, we used the parameterization of Cowan and Agol (2011a) to calculate the maximum dayside temperature, in the limit of a Bond albedo of zero and no heat recirculation:

$$T_{\mathrm{d,max}} = T_{\mathrm{eff}} \sqrt{\frac{R_\star}{a}} \left(\frac{2}{3}\right)^{1/4}. \tag{5.2}$$

Here T_{eff} is the stellar effective temperature, and $a/R_\star$ is the ratio of semimajor axis to stellar radius. We note that this equation assumes a circular orbit, while XO-3b is on an eccentric orbit ($e = 0.28$; Bonomo et al., 2017). Nonetheless, it allows us to get an order of magnitude estimate of the eclipse depth.

The above temperature can be converted to an eclipse depth using

$$D = \frac{B(\lambda, T_{\rm d})}{B(\lambda, T_{\star,4.5\mu m})} \left(\frac{R_{\rm p}}{R_\star}\right)^2 \tag{5.3}$$

where B is the Planck function, and $T_{\star,4.5\mu m}$ is the brightness temperature of the star at 4.5 μm, which we calculated by integrating PHOENIX models (Allard et al., 2011) over the *Spitzer* bandpass (Baxter et al., 2020). We represent the eclipse depth when $T_{\rm d} = T_{\rm d,max}$ by D_{max}.

For the non-hierarchical model, we placed a wide prior on the eclipse depth to prevent biasing the value: $D \sim \mathcal{N}(D_{max}/2, D_{max}/2)$. For the time of eclipse, we let $\tau \sim \mathcal{N}(\Delta t/2, \Delta t/2)$ where Δt is the duration of the observation, and time is measured from the start of the observation. We experimented with various priors and found that our resulting fits were consistent and not strongly dependent on the choice of priors.

For the hierarchical model, we used a wide Normal prior for the hierarchical mean: $\mu \sim \mathcal{N}(D_{max}/2, D_{max}/2)$. For the hierarchical standard deviation we used a weakly informative Half-Normal prior: $\sigma \sim$ Half-$\mathcal{N}$(300ppm). We then let the individual eclipse depths be drawn from the following higher level distribution: $D_i \sim \mathcal{N}(\mu, \sigma)$.

5.4.3 Detector Systematics: Gaussian Processes

The IRAC detector sensitivity in Channels 1 and 2 depends on the target centroid position on the detector. To parameterize this behaviour, we used a Gaussian process. The advantage of using a Gaussian process is that it doesn't require calculating the detector sensitivity explicitly, in contrast with polynomial models (Cowan et al., 2012) or BLISS (Stevenson et al., 2012b).

When using Gaussian processes, we make the usual assumption that the data are normally distributed, but allow for covariance between data points. The likelihood function can be written

$$p(\text{data}|\gamma) \sim \mathcal{N}(\mu_{\rm GP}, \Sigma), \tag{5.4}$$

where γ represents the model parameters and independent variables, and $\mu_{\rm GP}$ is the mean function around which the data are distributed. The covariance function, Σ, is an $n \times n$ matrix where n is the number of data. The entries along the diagonal of Σ are the measurement uncertainties on each datum, which we denote by σ_{phot}, and the off-diagonal entries are the covariance between data. When the off-diagonal elements are equal to zero, the likelihood function reduces to the usual assumption of independent Gaussian uncertainties.

Although it is computationally intractable to fit each off-diagonal entry of the covariance matrix, they can be parameterized using a kernel function with a handful of parameters. We used the squared exponential kernel employed by Evans et al. (2015)

$$\Sigma_{ij} = A \exp\left[-\left(\frac{x_i - x_j}{l_x}\right)^2 - \left(\frac{y_i - y_j}{l_y}\right)^2 \right], \tag{5.5}$$

where x and y represent the centroid locations on the IRAC detector, in pixel coordinates. The terms l_x and l_y are the covariance lengthscales, and A is the Gaussian process amplitude. The squared exponential kernel has the intuitive property that locations on the detector pixel that are close together should have similar sensitivity. If the length scales are fixed by the user rather than fitted for, this boils down to the Gaussian kernel regression of Knutson et al. (2012) and Lewis et al. (2013).

With no loss of generality, we can let the mean function be zero, and instead fit the residuals between the astrophysical model and observations which gives

$$p(\mathrm{residuals}|\gamma) \sim \mathcal{N}(0, \Sigma). \tag{5.6}$$

We placed weakly informative inverse gamma priors on the lengthscales. We chose the parameters such that 99% of the prior probability was between lengthscales 0 and 1, measured in pixels. This gives $p(l_x), p(l_y) \sim \mathrm{InverseGamma}(\alpha{=}11,\ \beta{=}5)$.

For the amplitude A, we used a weakly informative half normal prior: $A \sim$ Half-$\mathcal{N}(0, \Delta F/3)$, where ΔF is the range of observed flux values. By using a half normal prior, we weakly constrain the scale of the Gaussian process amplitude without introducing bias. We placed the same prior on the white noise uncertainty σ_{phot}.

5.4.4 The posterior

For each eclipse, we fit the eclipse depth D, time of eclipse τ, photometric uncertainty σ_{phot}, Gaussian process lengthscales l_x and l_y, and Gaussian process amplitude A. The planet-to-star flux ratio as a function of time t is given by F. The x and y centroid locations are included as covariates. We also fit for the hierarchical eclipse depth mean μ, and standard deviation σ.

The likelihood function for one eclipse is given by

$$p(F|t, x, y, \sigma_{\mathrm{phot}}, D, \mu, \sigma, \tau, l_x, l_y) \tag{5.7}$$

and the prior is

$$p(t, x, y, \sigma_{\mathrm{phot}}, D, \mu, \sigma, \tau, l_x, l_y). \tag{5.8}$$

We form the posterior function by multiplying the likelihood and prior together:

$$p(D, \mu, \sigma, \theta|F) \propto p(F|D, \mu, \sigma, \theta)p(D, \mu, \sigma, \theta) \tag{5.9}$$

where we have used $\theta = \{t, x, y, \sigma_{\mathrm{phot}}, \tau, l_x, l_y\}$ for simplicity.

First, note that the likelihood function does not depend on the hierarchical parameters directly, so we can remove μ and σ from the brackets of the likelihood function. Second, the eclipse depth depends on the hierarchical parameters in this way:

$$p(D|\mu, \sigma) = \frac{p(D, \mu, \sigma)}{p(\mu, \sigma)}, \tag{5.10}$$

where we have made use of Bayes' theorem.

This means we can rewrite the likelihood and prior to obtain:

$$p(D, \mu, \sigma, \theta|F) \propto p(F|D, \theta)p(D|\mu, \sigma)p(\mu, \sigma, \theta). \tag{5.11}$$

It is this refactoring that makes a hierarchical model different from a non-hierarchical one.

To form the posterior of the full hierarchical model, we multiply the individual eclipse posteriors together:

$$\begin{aligned}&\prod_{i=1}^{n} p(D_i, \mu, \sigma, \theta_i | F_i) \propto \\ &(p(\mu, \sigma))^n \prod_{i=1}^{n} p(F_i | D_i, \theta_i) p(D_i | \mu, \sigma) p(\theta_i)\end{aligned} \tag{5.12}$$

where n is the number of eclipse observations, 10 in the case of the XO-3b dataset. We have also used the fact that the priors on θ_i are independent from the priors on the hyperparameters μ and σ to perform the separation $p(\mu, \sigma, \theta_i) = p(\mu, \sigma)p(\theta_i)$.

5.4.5 Hamiltonian Monte Carlo

We used the probabilistic programming package PyMC3 to build and sample from the model. PyMC3 uses Hamiltonian Monte Carlo (HMC), the state-of-the-art Markov Chain Monte Carlo (MCMC) algorithm, to perform the sampling. HMC is more efficient than other MCMC algorithms, meaning it can effectively describe the posterior using fewer samples than other MCMC algorithms. For high dimensional models, and especially for high dimensional hierarchical models with pathological parameter spaces, the reduction in sample size afforded by HMC is all but necessary (Betancourt and Girolami, 2013).

Hamiltonian Monte Carlo works by treating probabilistic systems as if they are instead physical systems (Betancourt, 2017). The chains in an MCMC sampler move through parameter space to estimate the shape of the posterior; an equivalent physical system is the motion of a satellite orbiting a giant planet where the planet represents the mode of the probability distribution. The crucial step in HMC is to transform these trajectories from parameter space to momentum space (i.e., the space of the derivatives of the coordinates) using the Hamiltonian of the system, and sample from that instead by proposing a move in momentum space. By using conservation of energy, the HMC chains tend to remain in regions of high probability. In this way they efficiently traverse the typical set of the distribution, roughly defined as where the most of the probability mass of the posterior is concentrated.

To use Hamiltonian Monte Carlo, the gradient of the likelihood function, with respect to the parameters, is needed in order to construct the Hamiltonian of the system. PyMC3 does this using Theano, which is a deep learning library that allows for efficient manipulation of matrices (The Theano Development Team et al., 2016). STARRY is also built on Theano and allows for analytic expressions and gradients in the general case of eclipse and phase mapping. In our case, because we are dealing with eclipse-only observations and are able to neglect planetary limb darkening, the eclipse expressions reduce to the analytic expressions of Mandel and Agol (2002). Because astrophysical parameters tend to be correlated, we used the dense mass matrix HMC step from the *exoplanet* package (Foreman-Mackey et al., 2021).

The biggest advantage is that HMC can diagnose problematic posteriors or models. Posteriors with pathological regions, such as high curvature, are hard for typical MCMC samplers to explore efficiently; hierarchical models exhibit such pathologies. This can lead to biases in the final results that are hard to diagnose because typical samplers do not have the ability to properly detect and respond to parameter spaces with extreme geometries. When an HMC chain gets stuck in a region of high curvature or otherwise behaves badly, it will diverge to infinity and the sampler keeps track of where this occurred. Divergences can often be eliminated by changing the acceptance probability of the sampler, or by reparameterizing the model.

5.4.6 Model comparison: Information Criteria

It is common among exoplanet scientists to use the Bayesian Information Criterion (BIC) or Aikake Information Criterion (AIC) to perform model comparison and selection (Schwarz, 1978; Akaike, 1974). Both criteria use the maximum likelihood and a complexity term to penalize overly complex models. These two information criteria describe slightly different things— the AIC measures the relative predictive loss of a set of models, and the BIC measures how close each model is to the true model. In practice (at least in exoplanet science), they typically yield similar conclusions.

A shortcoming shared by BIC and AIC is that they are accurate only when using flat priors, which are not recommended for most models (Gelman et al., 2017). The AIC also assumes that the posterior distributions are multivariate Gaussians. The priors are never flat for hierarchical models, which means we cannot use the AIC or BIC for model comparison.

A more general model comparison tool is the Widely Applicable Information Criterion (WAIC; Watanabe, 2010). The WAIC is Bayesian, uses the full fit posterior and, critically, makes no assumptions about the shape of the posterior or priors. The WAIC is easily computed from the full fit posterior (McElreath, R., 2020):

$$\mathrm{WAIC}(\mathrm{data}, \Theta) = -2\left(\mathrm{lppd} - \sum_{\mathrm{i}} \mathrm{var}_{\theta}\left(\log \mathrm{p}\left(\mathrm{F_i} \mid \mathrm{D_i}, \theta_{\mathrm{i}}\right)\right)\right) \tag{5.13}$$

where Θ is the posterior, F_i stands for the i^{th} eclipse observation, data refers to the entire suite of observations, and lppd stands for the log-pointwise predictive-density,

$$\mathrm{lppd} = \sum_{i} \log\left(\frac{1}{S}\sum_{s=0}^{S} p\left(F_i \mid D_i, \theta_{i,s}\right)\right), \tag{5.14}$$

where S is the number of samples and $\theta_{i,s}$ is the S^{th} set of parameters for the i^{th} observation. The log predictive pointwise density is an estimate of how well the model would fit new, unseen data. The second term in the WAIC expression is a penalty term that penalizes overly complex models.

Once MCMC sampling has finished, the WAIC can be computed in a few lines of code using the MCMC chains. It is also possible to compute the standard error of the WAIC, something that is not possible with the BIC or AIC. If the difference in WAIC between two models is significantly larger than the standard error of the difference, then the model with the smaller WAIC is favoured over the other. If the difference in WAIC is smaller than the standard error of the difference, then the models make equally good predictions and there is no evidence to favour one over the other.

Since all modern secondary eclipse, transit and phase curve analyses use Markov Chain Monte Carlo to sample and store the posterior draws, the WAIC is a better choice than BIC or AIC for model comparison.

5.4.7 Pooling the GP parameters

We hypothesized that fitting a common set of Gaussian process amplitude and length scales across the suite of eclipses would yield more precise eclipse depths by sharing information about the detector sensitivity across the observations. Because we used Hamiltonian Monte Carlo, it was feasible to fully marginalize over the Gaussian process hyperparameters. However, we found that the fitted eclipse depths had nearly identical means and standard deviations between the shared and non-shared detector models of XO-3b. In practice we adopted the shared GP model for XO-3b because it has fewer parameters and is therefore easier to sample.

5.4.8 Results

We fit the ten 4.5 μm eclipses of XO-3b with three models: a model where each eclipse observation had its own, separate eclipse depth parameter, one where we used a single, pooled eclipse depth for all the observations, and a hierarchical model. To fit each model, we used 2000 tuning steps to initialize four HMC chains, and obtained 1000 samples for each chain. After sampling, we confirmed that the Gelman-Rubin statistic was close to 1 for all parameter values, and that there were no divergences. The eclipse depths from each model are shown graphically in Figure 5.1 and tabulated in Table 5.1. The best-fit model for each eclipse observation is shown in Figure 5.2. Figure 5.3 shows the best-fit eclipse signal after removing the detector systematics.

We also computed the ΔWAIC values compared to the best fit model, shown in Table 5.2. The hierarchical model had a significantly lower WAIC than the separate model, and a marginally lower WAIC than the single eclipse depth (pooled) model. This suggests that the eclipse depths are indeed different between observations, but are more similar than if we had used a separate eclipse parameter to describe each. This also hints at some variability from observation to observation. Typical hot Jupiters are predicted to show some epoch-to-epoch variability (Komacek and Showman, 2020), which is another reason to adopt the hierarchical model over the pooled one.

The mean eclipse depth for the three models are consistent with one another within

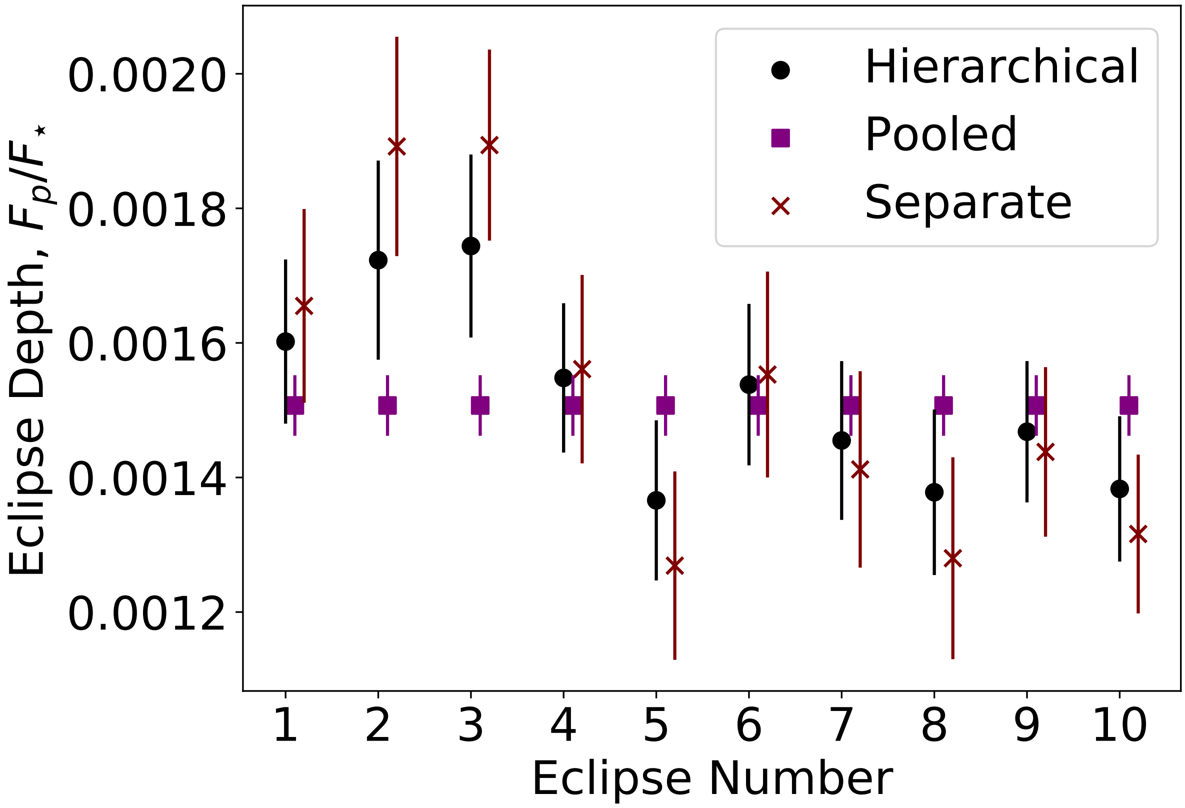

Figure 5.1: Eclipse depths of XO-3b for the three different models. The pooled model has the lowest eclipse depth uncertainty, but is not the best model according to the WAIC. The hierarchical model is the best model, and yields eclipses that are closer together, with lower uncertainties on the individual eclipse depths than the separate model (15% smaller on average). The hierarchical model represents a compromise between the overfit separate model and the underfit pooled model.

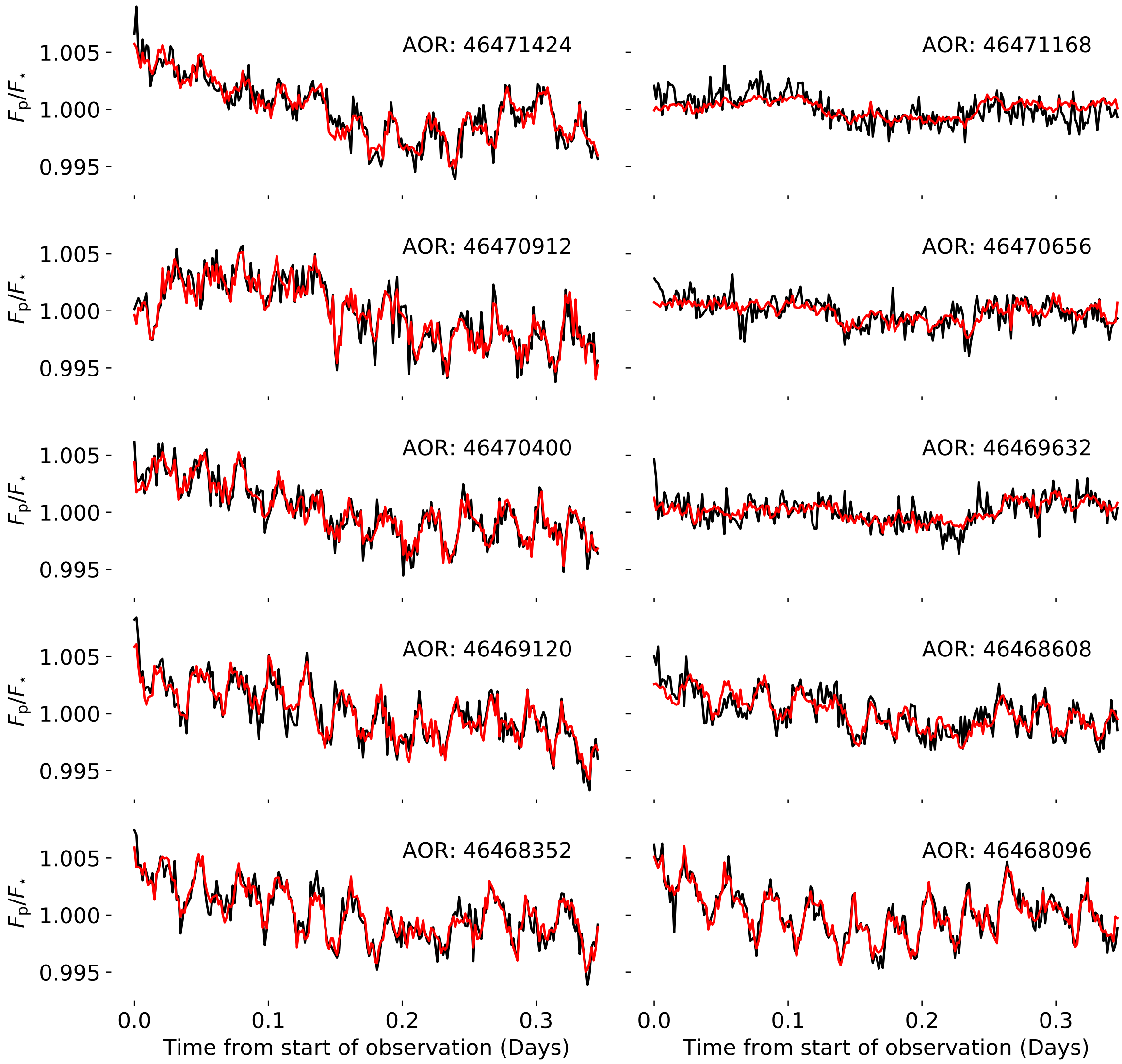

Figure 5.2: The full fit to each of the ten XO-3b eclipses, using the hierarchical model for the eclipse depths and a pooled Gaussian process for the detector systematics.

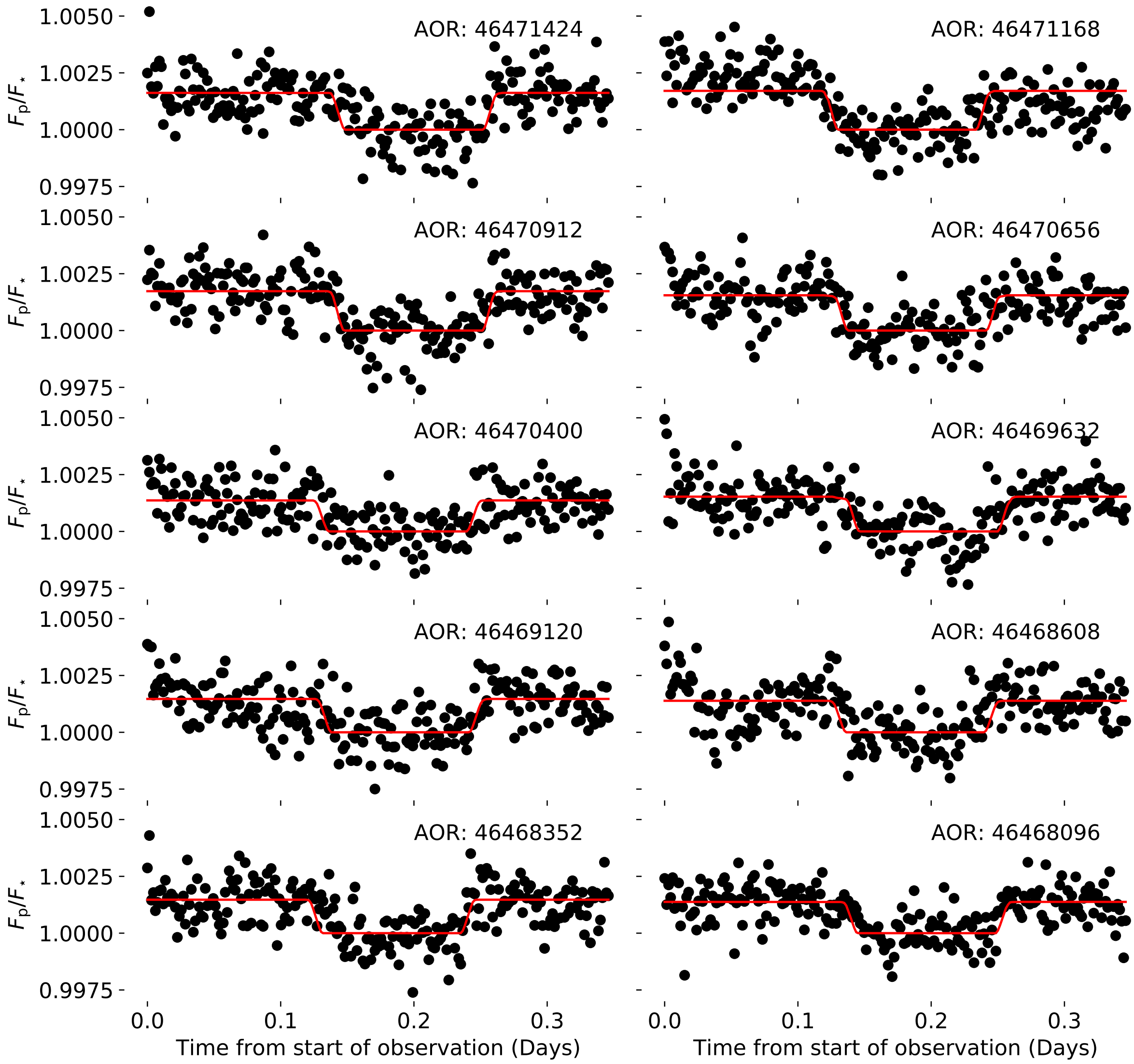

Figure 5.3: The ten XO-3b eclipses with the detector systematics removed using a Gaussian process as a function of stellar centroid location. The eclipse signal is clearly visible in the corrected raw data (represented by the black dots), and the best fit eclipse signal for each is shown as the red line.

Table 5.1: Best-fit eclipse depths from each model of the ten *Spitzer* IRAC channel 2 eclipses of XO-3b. The parameters μ and σ are the hierarchical mean and standard deviation for the suite of eclipse depths. With the pooled model, we are implicitly assuming $\sigma = 0$, while for the separate model we are implicitly assuming $\sigma = \infty$. The hierarchical model fits for the amount of pooling, and is preferred over both the completely pooled and separate models.

Eclipse Number	Hierarchical (ppm)	Pooled (ppm)	Separate (ppm)
1	1602±122	1507±45	1655±144
2	1723±148	1507±45	1892±163
3	1744±136	1507±45	1894±142
4	1548±111	1507±45	1561±140
5	1366±119	1507±45	1269±140
6	1538±120	1507±45	1553±153
7	1455±118	1507±45	1412±146
8	1378±123	1507±45	1280±150
9	1468±105	1507±45	1438±126
10	1383±108	1507±45	1316±118
μ	1520±81	1507±45	1527±219
σ	193±80	0	∞

Table 5.2: Comparison of different information criteria for the three XO-3b eclipse depth models— lower values are better. For the WAIC we also tabulate the standard error in the difference between each model. Using the BIC and AIC the pooled model is preferred. However, our model does not satisfy the assumptions necessitated by the BIC and AIC. The WAIC is more robust. According to the WAIC, the hierarchical model is the preferred model.

Model	Δ WAIC	$\sigma_{\Delta \mathrm{WAIC}}$	ΔAIC	ΔBIC
Hierarchical	0.0	0.0	7.46	10.80
Pooled	8.54	5.04	0	0
Separate	65.66	25.60	20.31	23.03

the uncertainties. In Figure 5.1, we see the effects of shrinkage on the eclipse depths. Compared to the separate model, the hierarchical model yields smaller scatter across the suite of eclipse depths and higher precision on the individual eclipse depths. Additionally, the individual uncertainties on the fitted eclipse depths are smaller by 15% on average in the hierarchical fits compared to the separate fits. The individual eclipse depth observations help constrain each other by shrinking the whole suite of eclipse depths towards the grand mean, but not as much as in the completely pooled model.

5.5 Hierarchical model for multiple planets

While hierarchical modelling is most obviously applicable for repeated measurements of the same planet, we can also extend it to secondary eclipse observations of multiple planets analyzed simultaneously. We considered the observations from Garhart et al. (2020), the largest dataset of uniformly reduced and analyzed hot Jupiter secondary eclipses.

We expect that a hot Jupiter's dayside temperature, $T_{\rm d}$, is approximately proportional to its irradiation temperature, $T_0 = T_{\rm eff}\sqrt{R_\star/a}$. We built a hierarchical model by including this intuition in our hyperprior, and making the hierarchical mean a function of irradiation temperature:

$$\mu_{\rm d} = m\left(T_0 - \langle T_0 \rangle\right) + b,$$

where $\langle T_0 \rangle$ is the average irradiation temperature for the ensemble of planets. In other words, our hierarchical mean is now a line described by a slope and standard deviation in the $T_{\rm d}$ vs T_0 plane. We represent the scatter about this line using the hyperparameter σ_d. The prior on the dayside brightness temperature for a given planet is then $T_{\rm d,p} \sim \mathcal{N}(\mu_{\rm d}, \sigma_d)$.

For this hierarchical model, the hierarchical mean itself depends on two hyperparameters, the slope and intercept of the line, which we fit for simultaneously with the suite of dayside brightness temperatures. We used the following weakly informative priors for the hyperparameters: $m \sim \mathcal{N}(1, 0.5)$, $b \sim \mathcal{N}(2200K, 500K)$, $\sigma_d \sim$ Half-$\mathcal{N}(500K)$.

We included the planets with measurements at both 4.5 μm and 3.6 μm, which gave a total of 33 planets. Fitting 66 eclipse observations simultaneously with a two-dimensional Gaussian process is computationally intractable using the hardware we had available, so we took the published measurements at face value rather than refit them. The reported eclipse depths and uncertainties are correct but were not properly propagated when converting to brightness temperature uncertainties (D. Deming, private communication), so we kept the sample of eclipses and eclipse depths measured by Garhart et al. (2020) but used the brightness temperatures and uncertainties calculated by Baxter et al. (2020). Comparing the two datasets, Garhart et al. (2020) overestimated the brightness temperature uncertainties by about a factor of two for each planet.

We again used PyMC3, and first fit a non-hierarchical model as our baseline, using separate $T_{d,p}$ parameters for each eclipse. As expected, this model just reproduces the published dayside temperatures and uncertainties. This also acts as a confidence check that our priors are not biasing the fitted parameters.

Since there are measurements at two different wavelengths, we fit two different versions of the hierarchical model. In the wavelength dependent model, we allowed the dayside brightness temperature distributions to be different between the two wavelengths, fitting one set of hierarchical parameters for the 4.5 μm measurements, and another set for the 3.6 μm measurements. In the wavelength independent model, we used a common distribution for all the measurements, and thus one set of hierarchical parameters. We tabulate the refit brightness temperatures in Table 5.3 and plot them in Figure 5.4.

We show the difference in WAIC values for the three models in Table 5.4. The wavelength independent model did slightly better than the wavelength dependent model (Δ WAIC = 0.54), however the uncertainty on that difference is 1.35, meaning the models make equally good predictions. In the wavelength independent model, the dayside brightness temperatures for both channels follow the same slope, or equivalently, the ratio of the slopes for each channel is equal to one. This means we are not detecting—nor ruling out—the trend of increasing brightness temperature ratio versus stellar irradiation reported by Garhart et al. (2020) and Baxter et al. (2020). The best-fit hierarchical parameters from our wavelength independent model are $\mu_d = 1.24 \pm 0.06$, $b = 2003 \pm 24K$, and $\sigma_m = 181 \pm 20K$.

The difference in WAIC suggests that the non-hierarchical model makes equally good predictions compared to the wavelength independent hierarchical model (Table 5.4), which is at odds with expectations that irradiation temperature should determine planetary dayside temperatures.

Table 5.3: Results from fitting a wavelength independent hierarchical model to the Garhart et al. (2020) eclipse dataset. The columns $T_{\mathrm{d,ch2}}$ and $T_{\mathrm{d,ch1}}$ list the refit dayside brightness temperatures at 4.5 μm 3.6 μm.

Planet	$T_0(K)$	$T_{\mathrm{d,ch2}}$ (K)	$T_{\mathrm{d,ch1}}$ (K)
HAT-P-13 b	2331±75	1739±81	1776±79
HAT-P-30 b	2315±61	1763±61	1860±49
HAT-P-33 b	2517±48	1912±85	1993±63
HAT-P-40 b	2496±93	1867±100	1975±113
HAT-P-41 b	2739±62	2171±77	2158±124
KELT-2 A b	2418±44	1693±49	1861±42
KELT-3 b	2577±62	2006±58	2270±57
Qatar-1 b	1964±61	1466±93	1409±117
WASP-100 b	3111±242	2362±80	2257±74
WASP-101 b	2198±57	1509±56	1678±58
WASP-103 b	3543±110	3299±51	3005±119
WASP-104 b	2144±61	1779±88	1717±70
WASP-12 b	3654±129	2665±42	2876±40
WASP-121 b	3336±86	2594±34	2370±35
WASP-131 b	2035±51	1174±86	1408±98
WASP-14 b	2636±85	2186±83	2239±38
WASP-18 b	3391±103	3102±92	2917±96
WASP-19 b	2922±65	2273±59	2323±53
WASP-36 b	2403±64	1647±125	1672±154
WASP-43 b	1945±112	1496±24	1660±24
WASP-46 b	2345±78	1910±105	1648±146
WASP-62 b	2018±49	1561±58	1852±68
WASP-63 b	2165±64	1437±104	1586±85
WASP-64 b	2390±74	1705±122	2051±79
WASP-65 b	2100±83	1367±131	1727±94
WASP-74 b	2720±75	2108±49	2003±38
WASP-76 b	3087±66	2471±32	2412±28
WASP-77 A b	2363±44	1635±36	1689±31
WASP-78 b	3246±124	2579±148	2699±123
WASP-79 b	2492±75	1885±52	1895±47
WASP-87 b	3268±96	2815±79	2673±76
WASP-94 A b	2127±109	1412±49	1530±35
WASP-97 b	2178±59	1593±43	1723±39

Table 5.4: WAIC scores for the three models used to fit the suite of eclipses from Garhart et al. (2020)— lower values are better. We also tabulate the standard error of the difference in WAIC between each model. The three models make equally good predictions according to the WAIC scores.

Model	Δ WAIC	$\sigma_{\Delta\mathrm{WAIC}}$
Separate	0.0	0.0
Wavelength Independent	1.13	2.54
Wavelength Dependent	1.67	2.42

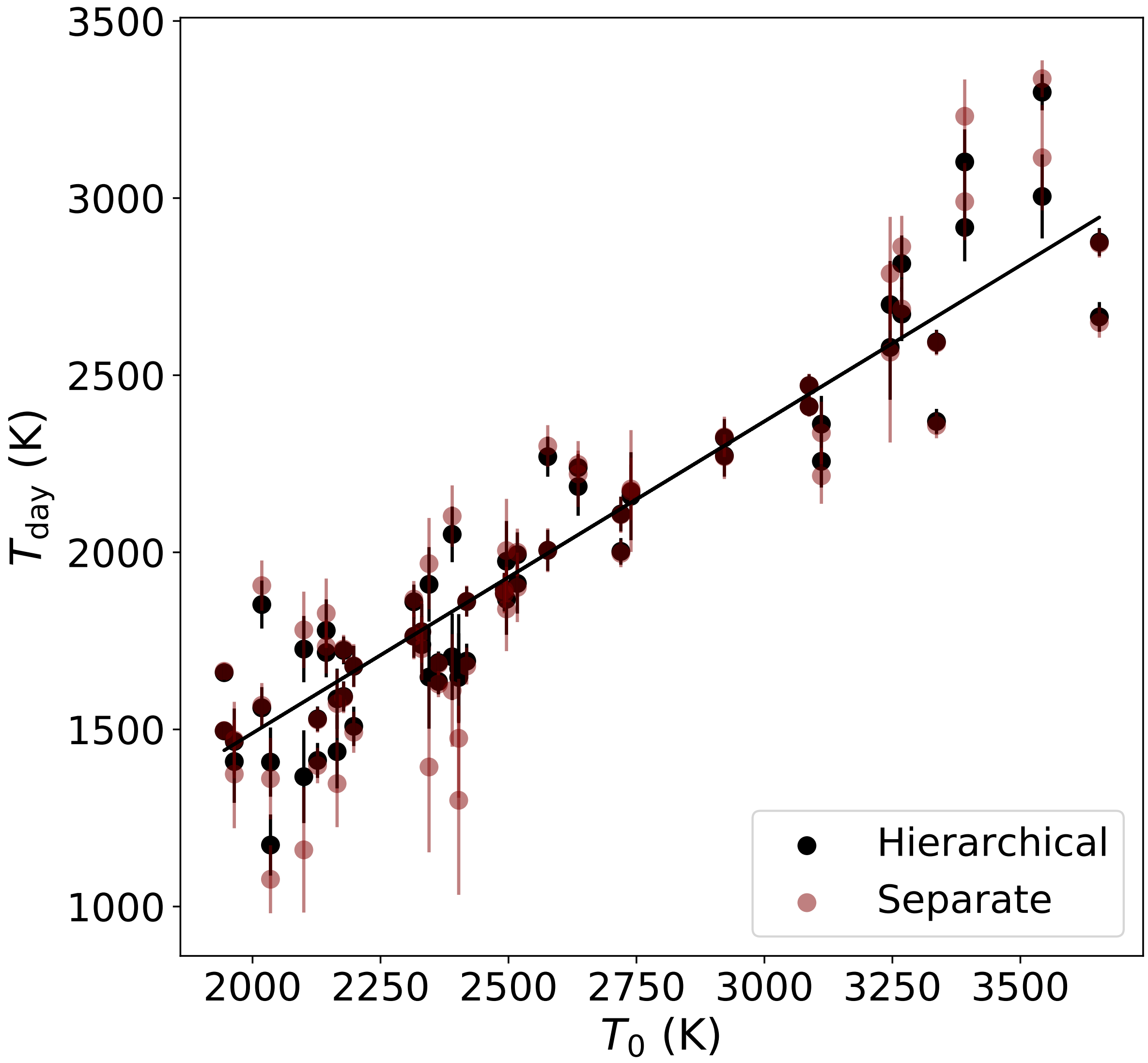

Figure 5.4: Dayside brightness temperatures, at 3.6 μm and 4.5 μm, for the planets analyzed by Garhart et al. (2020), refit with a wavelength independent hierarchical model. The red dots are the published values and the black line is the best fit trend line. The effects of Bayesian shrinkage are evident: the measurements are clustered closer to the line, and the uncertainties on the measurements are reduced.

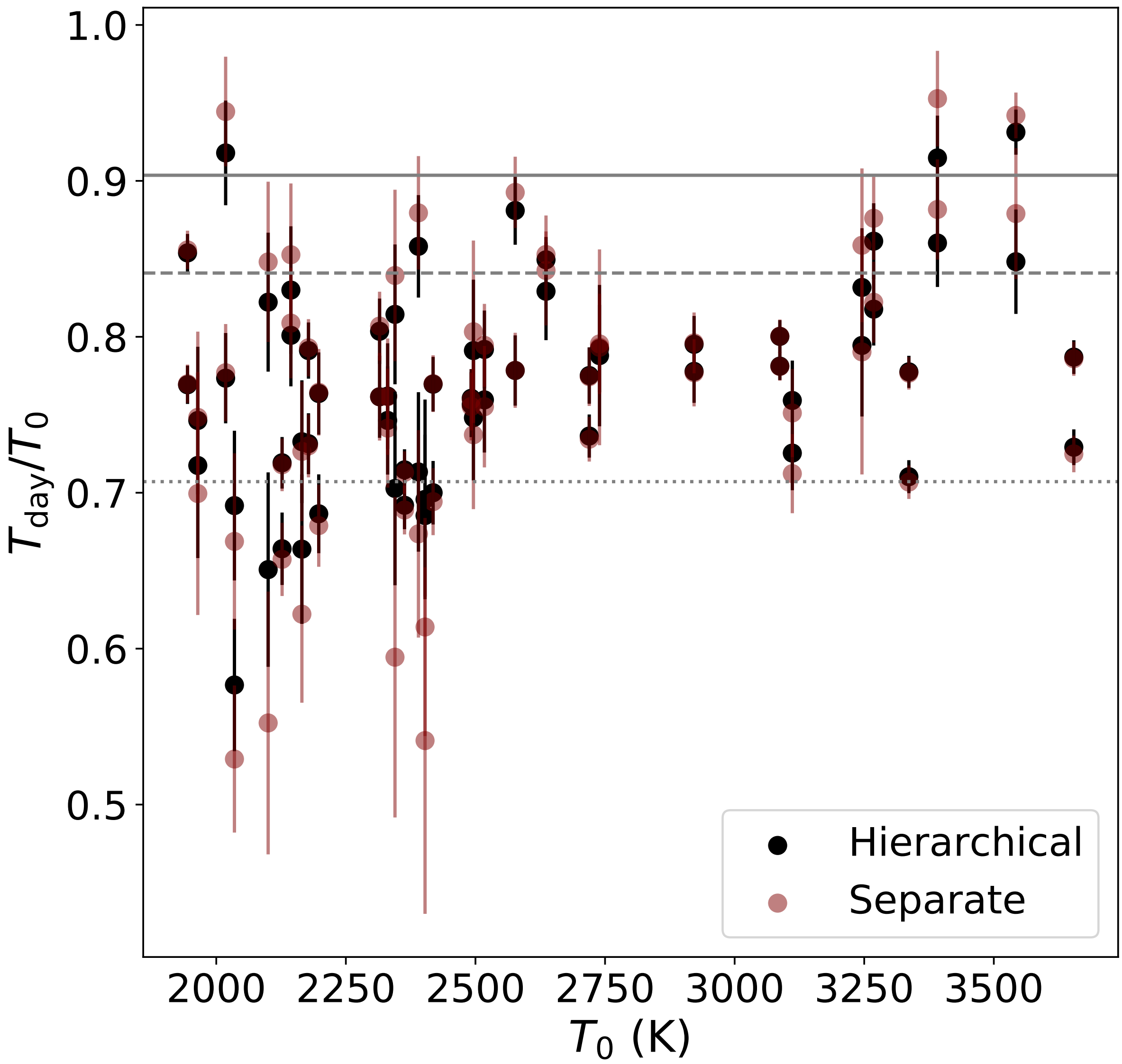

Figure 5.5: Dayside brightness temperatures from Fig 5.4, scaled by irradiation temperature. The horizontal lines represent some theoretical limits on dayside temperature assuming a zero Bond albedo: the solid line assumes zero heat recirculation, the dashed line assumes a uniform dayside hemisphere but a temperature of zero on the nightside, and the dotted line assumes a uniform temperature at every location on the planet.

5.6 Discussion and conclusions

5.6.1 Repeat observations of a single planet

In our reanalysis of the ten secondary eclipses of XO-3b, we found that the hierarchical model was favoured over the two non-hierarchical models. This means that the measured eclipse depths are indeed different from epoch to epoch, yet clustered. The biggest difference compared to previous analyses is that we were able to empirically fit for the amount of epoch-to-epoch scatter favoured by the data, and doing this improves the precision on our measurements by 15% on average, because of Bayesian shrinkage. Notably, we found that the hierarchical eclipse depth had a larger standard deviation than the individual measurements, suggesting that measuring just one eclipse depth could lead one to underestimate the true uncertainty compared to the hierarchical approach.

Hierarchical models could improve measurements of other hot Jupiters and other types of planets. Hierarchical models could be used to robustly test the reported variability in the secondary eclipses of the super earth 55 Cancri e (Demory et al., 2016; Tamburo et al., 2018), or to fit the twelve *Spitzer* eclipses of the recently discovered hot Saturn LTT 9779b (Dragomir et al., 2020). The published variability constraints for HD 189733b (Agol et al., 2010) and HD 209458b (Kilpatrick et al., 2020) could also be revisited with hierarchical models.

Repeated phase curve observations could benefit from using hierarchical models. The hot Jupiter WASP-43b has one published (Stevenson et al., 2017; Mendonça et al., 2018; Morello et al., 2019; May and Stevenson, 2020; Bell et al., 2021), and two unpublished, *Spitzer* phase curves at 4.5 μm. A hierarchical model could be used to better constrain the phase amplitudes and offsets of the three 4.5 μm phase curves by fitting them simultaneously.

To test whether we are seeing the effects of variability or detector systematics, the best approach is to compare planets with repeated observations in both *Spitzer* channels. If certain types of planets have larger hierarchical eclipse standard deviations, the culprit could be time variability that is only exhibited by certain planets. Otherwise, if one

Spitzer channel tends show more variability regardless of planet, it suggests that detector systematics are at play. Spectroscopic observations will also be able to break the degeneracy between variability and detector systematics, as would simultaneous measurements with multiple instruments.

5.6.2 Parallel analysis of multiple planets

We showed that our hierarchical model of measurements from multiple planets yields smaller uncertainties on the individual eclipse depths, and tends to shrink the eclipse depths toward the trend line. We did not detect the trend of increasing brightness temperature ratio with increasing stellar irradiation reported by Garhart et al. (2020) and Baxter et al. (2020), nor did we rule it out. The hierarchical models made predictions that were as good as the non-hierarchical model, when comparing the WAIC values.

One possible explanation is that the uncertainties on the eclipse depths are underestimated due to detector systematics or astrophysical variability. This was first suggested by Hansen et al. (2014), who concluded that the first generation of *Spitzer* eclipse uncertainties may be underestimated by up to a factor of 3, probably due to inadequate treatment of detector systematics. Hot Jupiter infrared eclipse depths are generally assumed to be the same from epoch-to-epoch because most general circulation models produce stable circulation patterns (Komacek and Showman, 2020), but recent work using high-resolution GCMs predicts multiple equilibria in hot Jupiter atmospheres and transient planetary-scale storms (Cho et al., 2021). The consequence of such variability, much like detector systematics, is that measuring just a single eclipse for a planet in a given bandpass would lead one to underestimate the uncertainty. Indeed, we found that for XO-3b, the hierarchical standard deviation was larger than the individual uncertainties by about a factor of 1.5–2. This suggests that if we had observed only one eclipse of XO-3b, we would have underestimated the eclipse depth uncertainty compared to the estimate from the hierarchical model.

In the context of a hierarchical model, small measurement uncertainties leave less leeway for Bayesian shrinkage. Indeed, repeating our analysis using the larger, albeit miscalculated, uncertainties from Garhart et al. (2020) showed a marked improvement when using the hierarchical model compared to the completely separate model (see the Appendix for the results of that analysis).

Another explanation for the marginal performance of hierarchical models on the Garhart et al. (2020) ensemble of planets is that irradiation temperature is not the sole determinant of planetary dayside temperatures. It is becoming clear that secondary parameters like planetary mass, radius, and rotation rate play important roles in determining atmospheric circulation on hot Jupiters (Keating et al., 2019; Bell et al., 2021). Differences in these parameters could contribute additional planet-to-planet scatter.

In this work we used the largest subset of *Spitzer* secondary eclipses that had been uniformly reduced and analyzed. One obvious extension of our work is to refit the detector systematics and astrophysical signals for all *Spitzer* secondary eclipses using a uniform pipeline. We recommend using a hierarchical model for the dayside brightness temperatures and placing a second level of hierarchy on the planets with repeated eclipses. This would take a prohibitively long time using a two dimensional Gaussian process and conventional hardware like we did for XO-3b, but it could potentially be done using high-performance or GPU computing. Alternatively, such a fit could be done using an easier-to-compute detector model like Pixel Level Decorrelation (Deming et al., 2015; Garhart et al., 2020), especially with PyMC3.

In this work we have shown that hierarchical models are useful when analyzing repeated measurements from a single target, or when doing comparative exoplanetology of many targets. Next generation telescopes like *James Webb* and *Ariel* will make repeated measurements of certain targets, and will both carry out photometric and spectroscopic transit, eclipse, and phase curve surveys for a variety of targets (Bean et al., 2018; Tinetti et al., 2018; Charnay et al., 2021). This will allow for atmospheric characterization of potentially thousands of more exoplanets, from Earth-like planets to ultra-hot Jupiters, and we recommend that these comparative surveys incorporate hierarchical modelling to make measurements and predictions that are as robust as possible.

Acknowledgements

This project was conceived at the "Multi-dimensional characterization of distant worlds: spectral retrieval and spatial mapping" workshop hosted by the Michigan Institute for Research in Astrophysics and spearheaded by Emily Rauscher. We are particularly grateful to David van Dyk for a pedagogical introduction to Bayesian shrinkage. We acknowledge support from the McGill Space Institute and l'Institut de recherche sur les exoplanètes. We have made use of open-source software provided by the Python, Astropy, SciPy, Matplotlib, and PyMC3 communities.

Data Availability

The reduced photometry for the ten archival secondary eclipse observations of XO-3b are freely available at `https://irachpp.spitzer.caltech.edu/page/data-challenge-2015`. The code used in the XO-3b reanalysis, and a Jupyter notebook showing the reanalysis of the Garhart et al. (2020) eclipses can both be found at `https://github.com/dylanskeating/HARMONiE`.

5.7 Analysis using inflated uncertainties

We also considered the brightness temperatures and uncertainties reported by Garhart et al. (2020). Their eclipse depths, eclipse depth uncertainties, and brightness temperatures are correct, but the brightness temperature uncertainties were derived by taking the relative uncertainty in eclipse depth and using that to calculate the uncertainty in brightness temperature (D. Deming, private communication). In their reanalysis, Baxter et al. (2020) used the eclipse depths and uncertainties reported by Garhart et al. (2020) but fully propagated those uncertainties through the Planck function, which is non-linear, to derive uncertainties on the brightness temperatures. Comparing the uncertainties reported in both works, the uncertainties of Garhart et al. (2020) are roughly twice as big as those reported by Baxter et al. (2020).

Table 5.5: WAIC scores for the three models, using the artificially inflated brightness temperature uncertainties from (Garhart et al., 2020). We also tabulate the standard error of the difference in WAIC between each model. The two hierarchical models both make equally good predictions, and significantly outperform the non-hierarchical model.

Model	Δ WAIC	$\sigma_{\Delta \mathrm{WAIC}}$
Wavelength Dependent	0.0	0.0
Wavelength Independent	0.25	1.8
Separate	11.09	3.61

To see how our conclusions would change had we used the artificially inflated uncertainties, we refit the multi-planet hierarchical model from Section 5.5. According the ΔWAIC scores (Table 5.5), the wavelength independent hierarchical model makes much better predictions than the non-hierarchical model, and marginally better predictions than the wavelength dependent model. Again, we do not detect the trend of increasing 4.5 μm to 3.6 μm brightness temperature ratio, nor do we rule it out.

The refit brightness temperatures are shown in Figure 5.6 and Figure 5.7. When measurement uncertainties are higher, Bayesian shrinkage is more dramatic.

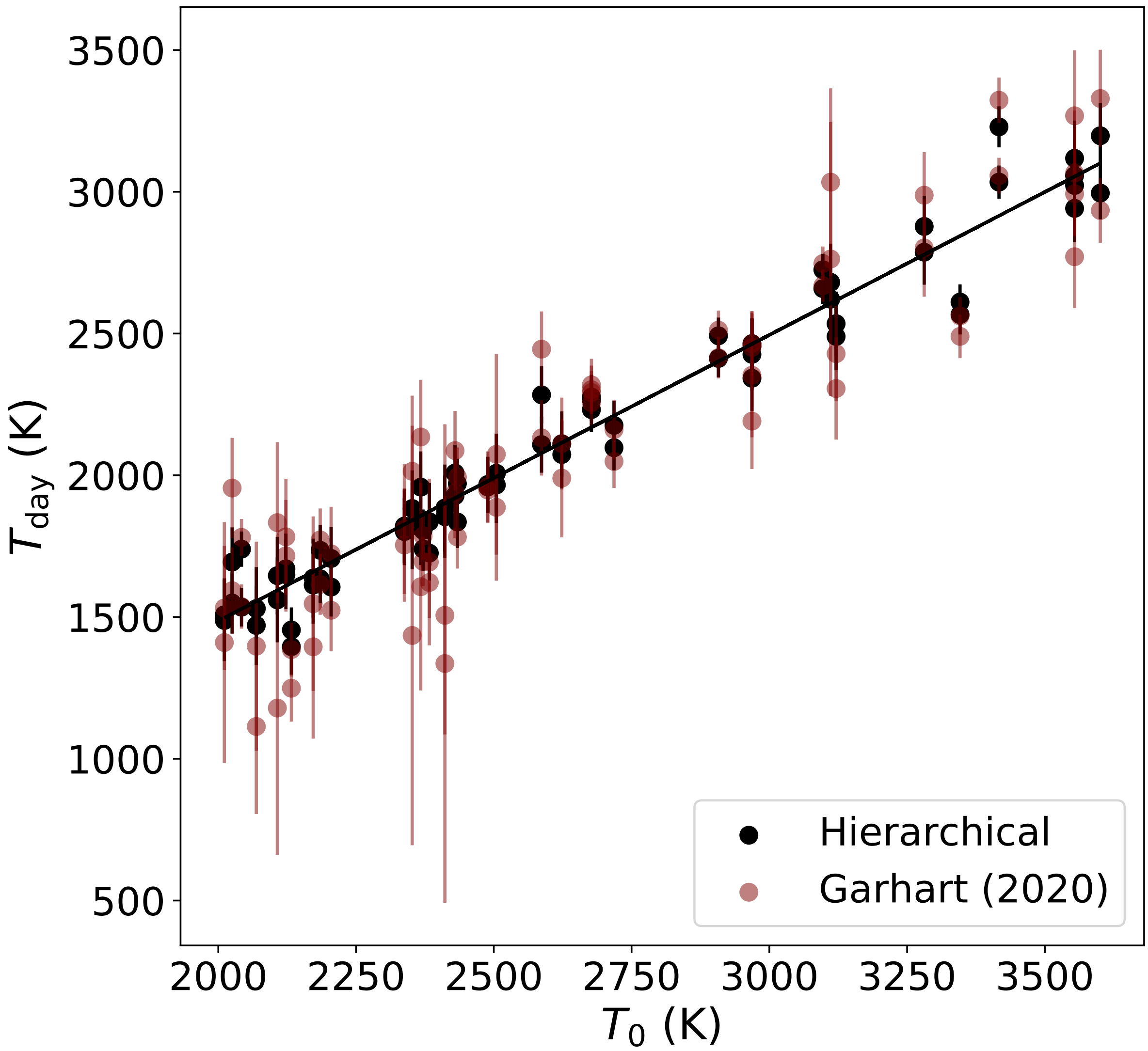

Figure 5.6: Dayside brightness temperatures refit with a wavelength independent hierarchical model. We used the inflated uncertainties from (Garhart et al., 2020). The red dots are the published values and the black line is the best fit trend line. The effects of Bayesian shrinkage are evident: the measurements are clustered closer to the line, and the uncertainties on the measurements are reduced.

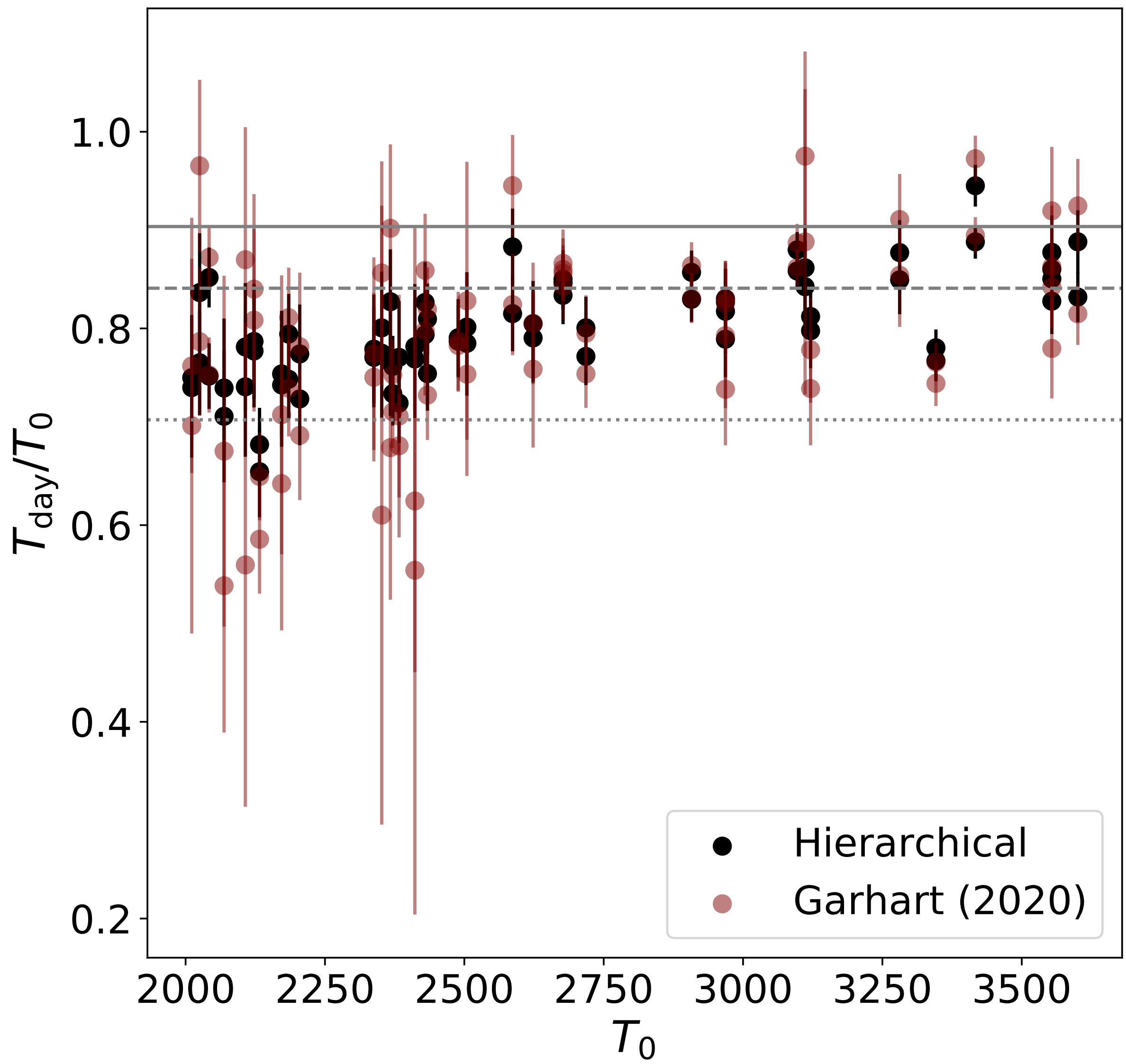

Figure 5.7: Dayside brightness temperatures from Fig 5.6, this time scaled by irradiation temperature. The horizontal lines represent some theoretical limits on dayside temperature assuming a zero Bond albedo: the solid line assumes zero heat recirculation, the dashed line assumes a uniform dayside hemisphere but a temperature of zero on the nightside, and the dotted line assumes a uniform temperature at every location on the planet.

6 General Discussion and Conclusion

A guiding hypothesis behind most hot Jupiter atmospheric characterization to date is that the amount of incoming stellar irradiation is the most important factor determining atmospheric circulation. Increasing the stellar irradiation causes a planet to radiate faster than it can advect the absorbed flux from day to night. This should cause dayside temperatures and phase curve amplitudes to increase with increasing irradiation, and the bright spot offset to decrease with increasing irradiation. Two planets that receive the same amount of stellar irradiation should have similar circulation patterns and phase curves. However, the diversity of observed phase curves has made it clear that this picture is incomplete.

The 4.5 μm *Spitzer* phase curve of the hot Jupiter HD 209458b showed that the planet has a hot nightside ($T_{\rm night} = 927 \pm 77$K) and thus must be efficiently transporting heat from day to night (Zellem et al., 2014). In contrast, fellow hot Jupiter WASP-43b receives the same amount of stellar flux as HD 209458b but was initially reported to be emitting no flux from its nightside, indicating non-existent day-night heat transport (Stevenson et al., 2017). In the work presented in Chapter 2, we suggested that the detection of a negative nightside flux by Stevenson et al. (2014, 2017) was due to the authors not imposing physically possible phase curves when fitting and hence mis-estimating the instrumental systematics. By correcting negative regions of the phase curves, we showed that WASP-43b transports a similar amount of heat from day to night as HD 209458b, drastically altering the inferred energy budget of the planet. Several reanalyses have all confirmed that WASP-43b transports a moderate amount of heat from day to night (Mendonça et al., 2018; Morello et al., 2019; May and Stevenson, 2020; Bell et al., 2020). Subsequent analyses of other phase curves have demanded that the phase curves be strictly positive when fitting observations (Dang et al., 2018; Arcangeli et al., 2019; Bell et al., 2020). WASP-43b will be studied extensively with the *James Webb Space Telescope* in both the Early Release Science and Guaranteed Time Observations programs. Full-orbit, spectroscopic phase curves will be observed with the NIRISS and MIRI instruments, which will allow for much more accurate and precise estimates of WASP-43b's nightside brightness temperatures between 2.9–12 μm. This will also allow nightside spectral retrieval to be performed, which will help determine the cloud composition (Bean et al., 2018).

Dayside temperatures on hot Jupiters have long been noted to track the planets' irradiation temperatures; planets that receive more stellar irradiation have higher dayside temperatures than planets receiving less flux (Cowan and Agol, 2011a). Dayside temperatures can be measured with secondary eclipses, which last several hours. In contrast, to measure nightside temperatures, full-orbit phase curves lasting a day or more are necessary. There are fewer phase curves than secondary eclipse measurements: more than a hundred planets had their secondary eclipses observed in at least one *Spitzer* bandpass, while 29 hot Jupiters were observed for a full orbit. Not all of these phase curves have been published yet.

At the time of writing of the manuscript in Chapter 3, just twelve hot Jupiters had published phase curves. Several of the phase curves had the same problem as WASP-43b: they were not strictly positive, requiring impossibly negative fluxes at some longitudes on the planet. After correcting these phase curves for negative flux, we found that the nightside effective temperature as a function of irradiation temperature is relatively constant, and just under 1100 K. The few ultra-hot Jupiters in the sample have hotter nightside temperatures than that, due to an additional heat transport mechanism in the form of hydrogen dissociation and recombination (Bell and Cowan, 2018; Tan and Komacek, 2019). The nightside trend was confirmed by the reanalysis of Bell et al. (2020)

It could be that despite the vast differences in irradiation temperatures, radii, masses, and orbital periods of hot Jupiters, the forces at work in their atmospheres all conspire to transport just the right amount of heat from the dayside of each planet to make the nightside temperatures the same from planet to planet. The simpler explanation, and the one that we espoused in Chapter 3, is that the constant temperature is suggestive of a universal nightside cloud species across the planets that is opaque to outgoing long-wave radiation, and disconnects the observed flux, emitted from the cloud tops, from the temperature and pressure structure below. For the very hottest planets, additional heat transport from hydrogen dissociation and recombination produce greater nightside temperatures, evaporating cloud particles.

Clouds are predicted to be ubiquitous on hot Jupiter nightsides (Parmentier et al., 2016), and the constant temperature suggests that they are likely to be silicate clouds, based on their temperatures and the predicted photospheric pressures. Microphysical cloud models predict that transmission spectra of hot Jupiters are likely to be dominated by optically thick silicate clouds, because silicate clouds have lower nucleation energies than clouds with other compositions and therefore condense more easily (Gao et al., 2020). Alternatively, Parmentier et al. (2021) suggested that the dominant cloud species on hot Jupiter nightsides depends strongly on the planets' equilibrium temperatures, and the constant nightside temperature is instead due to the strong dependence of the radiative timescale with temperature rather than a universal cloud species. The authors still required nightside clouds to reconcile the mismatch between their exact predictions at the *Spitzer* observations, but in this framework the cloud composition would instead vary with the irradiation temperature of each planet, much like what is seen for brown dwarfs (Parmentier and Crossfield, 2018). Each cloud species will have a unique spectral signature in the 5-15μm bandpass, observable with the Mid-infrared Instrument (MIRI) onboard JWST, meaning it will be possible to test both hypotheses using spectroscopic phase curves.

Early phase curve studies focused on comparing planets with different irradiation temperatures, but there are now enough observations that it is possible to examine the effects of other physical properties. The work in Chapter 4 showed that three planets with the same irradiation temperatures but different radii, masses, and orbital periods all exhibit different atmospheric circulation patterns. Qatar-1b has a negligible bright spot offset, at odds with the significant eastward offsets observed for HD 209458b and WASP-43b. One possible explanation, again, hinges on the effects of clouds— Roman et al. (2021) showed that including clouds in GCMs reduces phase curve offsets compared to cloud free models. Additionally, cloud models that simply add clouds to a cloud free GCM after the simulation reaches equilibrium have significantly different circulation patterns than GCMs that incorporate radiative feedback from clouds (Harada et al., 2021). Cloud models of various levels of sophistication have been successfully implemented in GCMs (Lee et al., 2016, 2017; Lines et al., 2019; Gao et al., 2020; Helling et al., 2021). Another explanation for the small offset for Qatar-1b is magnetic drag due to interactions with the planet's magnetic field, but magnetohydrodynamic effects have not yet been implemented in GCMs. There are still mismatches between GCM predictions and trends from observed phase curves, which means that incorporating magnetohydrodynamics, cloud formation microphysics, and radiative feedback from clouds is a necessary step forward.

It is becoming clear that although irradiation temperature is not the only determinant of hot Jupiter climate, more observations are needed to untangle the effects of other physical properties. In 2018 we submitted a successful Spitzer proposal to observe phase curves at 4.5 μm for ten additional hot Jupiters that had not been previously observed; this survey was the final phase curve survey performed by Spitzer before the mission ended (PID 14059, PI Bean). The irradiation temperatures of the planets in the sample spanned from 1600 K to 4000 K, more or less evenly spaced across this range. Three of the phase curves from this program have been published so far, for the ultra-hot Jupiters KELT-9b (Mansfield et al., 2020a), KELT-16b, and MASCARA-1b (Bell et al., 2020), and the rest are forthcoming. I was a coauthor on both papers. KELT-9b is the hottest planet in the sample, and is in fact the hottest planet known so far with a dayside as hot as K4-type star (T_{day} = 4600 K; Gaudi et al. (2017)). The *Spitzer* phase curve from our program shows evidence that KELT-9b has efficient day-night heat transport due to hydrogen dissociation and recombination (Mansfield et al., 2020a). Its nightside temperature is a scorching 2556 ± 100K, likely too hot for clouds to form.

KELT-16b and MASCARA-1b have similar radii ($1.4R_{\mathrm{jup}}$) and masses ($3M_{\mathrm{jup}}$) to one another and receive the same amount of stellar irradiation from their host stars ($T_0 \approx 3500K$). The main difference is their rotational periods, which are 0.97 and 2.15 days respectively. This could lead to differences in Coriolis forces and hence different atmospheric circulation patterns; MASCARA-1b is expected to have a larger phase offset and nightside temperature than KELT-16b (Tan and Showman, 2020; Bell et al., 2020). Despite this, their best-fit phase curve properties were found to be identical within uncertainties (Bell et al., 2020). Additionally, their dayside temperatures, nightside temperatures, and phase offsets are consistent with the similarly irradiated planets WASP-18b, WASP-103b, and the brown dwarf KELT-1b (Bell et al., 2020).

It is unclear why there was more uniformity for this set of ultra-hot Jupiters than for the trio of merely-hot Jupiters HD 209458b, WASP-43b, and Qatar-1b, but comparing other temperature "temperature twin" planets could help resolve this mystery. For instance WASP-34b, the least-irradiated planet in our phase curve survey, has the same irradiation temperature as HD 189733b, but twice the rotation period (4.32 days). The 7 remaining unpublished phase curves from our study are for hot Jupiters with irradiation temperatures ranging from 1639 K to 3195 K, and including other observing programs, there are 14 hot Jupiters with unpublished 4.5 μm *Spitzer* phase curves, and 5 of these planets also have 3.6 μm phase curves. Even though the *Spitzer* mission is over, there is still more hot Jupiter science to be wrung out of it.

The work presented in Chapter 4 demonstrated the utility of comparing different reduction and analysis pipelines, as some of the retrieved phase curve parameters were discrepant between the two pipelines that I used. This was also found to be the case in the wholesale, uniform reanalysis of published *Spitzer* phase curves, where discrepancies between the reanalysis and previous literature values were found (Bell et al., 2020). The takeaway is that these types of comparisons should be done as soon as possible for next-generation exoplanet surveys like *James Webb* and *Ariel*, rather than waiting until the end of the mission like was done for *Spitzer*.

Likewise, hierarchical models like the ones outlined in Chapter 5 deserve to be the default when analyzing repeated observations of the same target, or when doing comparative exoplanetology. They should be incorporated from the get-go, for instance for the repeated transits or eclipses that *James Webb* will collect during its Early Release Science and Guaranteed Time Observation period, or for the comparative eclipse and phase curve surveys planned for the *Ariel* mission. *James Webb* has the potential to detect variability in secondary eclipses (Komacek and Showman, 2020), and phase curve variability may be detectable with *Ariel* (Komacek and Showman, 2020). This motivates making repeated observations of the same target, and these repeated observations should be modelled hierarchically. Finally, hierarchical models could also be used to combine observations that access the same wavelength, for instance, augmenting upcoming *JWST* NIRISS spectroscopic observations with existing *Spitzer* transits or eclipses .

Bibliography

E. Agol, N. B. Cowan, H. A. Knutson, D. Deming, J. H. Steffen, G. W. Henry, and D. Charbonneau. The Climate of HD 189733b from Fourteen Transits and Eclipses Measured by Spitzer. *The Astrophysical Journal*, 721(2):1861–1877, Oct. 2010. doi: 10.1088/0004-637X/721/2/1861.

H. Akaike. A New Look at the Statistical Model Identification. *IEEE Transactions on Automatic Control*, 19:716–723, Jan. 1974.

F. Allard, P. H. Hauschildt, and A. Schweitzer. Spherically Symmetric Model Atmospheres for Low-Mass Pre-Main-Sequence Stars with Effective Temperatures between 2000 and 6800 K. *The Astrophysical Journal*, 539(1):366–371, Aug. 2000. doi: 10.1086/309218.

F. Allard, D. Homeier, and B. Freytag. Model Atmospheres From Very Low Mass Stars to Brown Dwarfs. In C. Johns-Krull, M. K. Browning, and A. A. West, editors, *16th Cambridge Workshop on Cool Stars, Stellar Systems, and the Sun*, volume 448 of *Astronomical Society of the Pacific Conference Series*, page 91, Dec. 2011.

K. A. Alsubai, N. R. Parley, D. M. Bramich, R. G. West, P. M. Sorensen, A. Collier Cameron, D. W. Latham, K. Horne, D. R. Anderson, G. Á. Bakos, D. J. A. Brown, L. A. Buchhave, G. A. Esquerdo, M. E. Everett, G. Fżrész, J. D. Hartman, C. Hellier, G. M. Miller, D. Pollacco, S. N. Quinn, J. C. Smith, R. P. Stefanik, and A. Szentgyorgyi. Qatar-1b: a hot Jupiter orbiting a metal-rich K dwarf star. *Monthly Notices of the Royal Astronomical Society*, 417(1):709–716, Oct. 2011. doi: 10.1111/j.1365-2966.2011.19316.x.

I. Angelo and R. Hu. A Case for an Atmosphere on Super-Earth 55 Cancri e. *The Astronomical Journal*, 154(6):232, Dec. 2017. doi: 10.3847/1538-3881/aa9278.

J. Arcangeli, J.-M. Désert, V. Parmentier, K. B. Stevenson, J. L. Bean, M. R. Line, L. Kreidberg, J. J. Fortney, and A. P. Showman. Climate of an ultra hot Jupiter. Spectroscopic phase curve of WASP-18b with HST/WFC3. *Astronomy and Astrophysics*, 625:A136, May 2019. doi: 10.1051/0004-6361/201834891.

D. J. Armstrong, E. de Mooij, J. Barstow, H. P. Osborn, J. Blake, and N. F. Saniee. Variability in the atmosphere of the hot giant planet HAT-P-7 b. *Nature Astronomy*, 1:0004, Dec. 2016. doi: 10.1038/s41550-016-0004.

C. Baxter, J.-M. Désert, V. Parmentier, M. Line, J. Fortney, J. Arcangeli, J. L. Bean, K. O. Todorov, and M. Mansfield. A transition between the hot and the ultra-hot Jupiter atmospheres. *Astronomy and Astrophysics*, 639:A36, July 2020. doi: 10.1051/0004-6361/201937394.

J. L. Bean, K. B. Stevenson, N. M. Batalha, Z. Berta-Thompson, L. Kreidberg, N. Crouzet, B. Benneke, M. R. Line, D. K. Sing, H. R. Wakeford, H. A. Knutson, E. M. R. Kempton, J.-M. Désert, I. Crossfield, N. E. Batalha, J. de Wit, V. Parmentier, J. Harrington, J. I. Moses, M. Lopez-Morales, M. K. Alam, J. Blecic, G. Bruno, A. L. Carter, J. W. Chapman, L. Decin, D. Dragomir, T. M. Evans, J. J. Fortney, J. D. Fraine, P. Gao, A. García Muñoz, N. P. Gibson, J. M. Goyal, K. Heng, R. Hu, S. Kendrew, B. M. Kilpatrick, J. Krick, P.-O. Lagage, M. Lendl, T. Louden, N. Madhusudhan, A. M. Mandell, M. Mansfield, E. M. May, G. Morello, C. V. Morley, N. Nikolov, S. Redfield, J. E. Roberts, E. Schlawin, J. J. Spake, K. O. Todorov, A. Tsiaras, O. Venot, W. C. Waalkes, P. J. Wheatley, R. T. Zellem, D. Angerhausen, D. Barrado, L. Carone, S. L. Casewell, P. E. Cubillos, M. Damiano, M. de Val-Borro, B. Drummond, B. Edwards, M. Endl, N. Espinoza, K. France, J. E. Gizis, T. P. Greene, T. K. Henning, Y. Hong, J. G. Ingalls, N. Iro, P. G. J. Irwin, T. Kataria, F. Lahuis, J. Leconte, J. Lillo-Box, S. Lines, J. D. Lothringer, L. Mancini, F. Marchis, N. Mayne, E. Palle, E. Rauscher, G. Roudier, E. L. Shkolnik, J. Southworth, M. R. Swain, J. Taylor, J. Teske, G. Tinetti, P. Tremblin, G. S. Tucker, R. van Boekel, I. P. Waldmann, I. C. Weaver, and T. Zingales. The Transiting Exoplanet Community Early Release Science Program for JWST. *Publications of the ASP*, 130(993):114402, Nov. 2018. doi: 10.1088/1538-3873/aadbf3.

T. G. Beatty, M. S. Marley, B. S. Gaudi, K. D. Colón, J. J. Fortney, and A. P. Showman. Spitzer Phase Curves of KELT-1b and the Signatures of Nightside Clouds in Thermal Phase Observations. *The Astronomical Journal*, 158(4):166, Oct. 2019. doi: 10.3847/1538-3881/ab33fc.

T. J. Bell and N. B. Cowan. Increased Heat Transport in Ultra-hot Jupiter Atmospheres through H_2 Dissociation and Recombination. *The Astrophysical Journal Letters*, 857(2):L20, Apr. 2018. doi: 10.3847/2041-8213/aabcc8.

T. J. Bell, M. Zhang, P. E. Cubillos, L. Dang, L. Fossati, K. O. Todorov, N. B. Cowan, D. Deming, R. T. Zellem, K. B. Stevenson, I. J. M. Crossfield, I. Dobbs-Dixon, J. J. Fortney, H. A. Knutson, and M. R. Line. Mass loss from the exoplanet WASP-12b inferred from Spitzer phase curves. *Monthly Notices of the Royal Astronomical Society*, 489(2):1995–2013, Oct. 2019. doi: 10.1093/mnras/stz2018.

T. J. Bell, L. Dang, N. B. Cowan, J. Bean, J.-M. Désert, J. J. Fortney, D. Keating, E. Kempton, L. Kreidberg, M. R. Line, M. Mansfield, V. Parmentier, K. B. Stevenson, M. Swain, and R. T. Zellem. A Comprehensive Reanalysis of Spitzer's 4.5 μm Phase Curves, and the Phase Variations of the Ultra-hot Jupiters MASCARA-1b and KELT-16b. *arXiv e-prints*, art. arXiv:2010.00687, Oct. 2020.

T. J. Bell, L. Dang, N. B. Cowan, J. Bean, J.-M. Désert, J. J. Fortney, D. Keating, E. Kempton, L. Kreidberg, M. R. Line, M. Mansfield, V. Parmentier, K. B. Stevenson, M. Swain, and R. T. Zellem. A comprehensive reanalysis of Spitzer's 4.5 μm phase curves, and the phase variations of the ultra-hot Jupiters MASCARA-1b and KELT-16b. *Monthly Notices of the Royal Astronomical Society*, 504(3):3316–3337, July 2021. doi: 10.1093/mnras/stab1027.

M. Betancourt. The Convergence of Markov chain Monte Carlo Methods: From the Metropolis method to Hamiltonian Monte Carlo. *arXiv e-prints*, art. arXiv:1706.01520, June 2017.

M. J. Betancourt and M. Girolami. Hamiltonian Monte Carlo for Hierarchical Models. *arXiv e-prints*, art. arXiv:1312.0906, Dec. 2013.

J. Blecic, J. Harrington, N. Madhusudhan, K. B. Stevenson, R. A. Hardy, P. E. Cubillos, M. Hardin, O. Bowman, S. Nymeyer, D. R. Anderson, C. Hellier, A. M. S. Smith, and A. Collier Cameron. Spitzer Observations of the Thermal Emission from WASP-43b. *The Astrophysical Journal*, 781(2):116, Feb. 2014. doi: 10.1088/0004-637X/781/2/116.

A. S. Bonomo, S. Desidera, S. Benatti, F. Borsa, S. Crespi, M. Damasso, A. F. Lanza, A. Sozzetti, G. Lodato, F. Marzari, C. Boccato, R. U. Claudi, R. Cosentino, E. Covino, R. Gratton, A. Maggio, G. Micela, E. Molinari, I. Pagano, G. Piotto, E. Poretti, R. Smareglia, L. Affer, K. Biazzo, A. Bignamini, M. Esposito, P. Giacobbe, G. Hébrard, L. Malavolta, J. Maldonado, L. Mancini, A. Martinez Fiorenzano, S. Masiero, V. Nascimbeni, M. Pedani, M. Rainer, and G. Scandariato. The GAPS Programme with HARPS-N at TNG . XIV. Investigating giant planet migration history via improved eccentricity and mass determination for 231 transiting planets. *Astronomy and Astrophysics*, 602:A107, June 2017. doi: 10.1051/0004-6361/201629882.

V. Bourrier, D. Kitzmann, T. Kuntzer, V. Nascimbeni, M. Lendl, B. Lavie, H. J. Hoeijmakers, L. Pino, D. Ehrenreich, K. Heng, R. Allart, H. M. Cegla, X. Dumusque, C. Melo, N. Astudillo-Defru, D. A. Caldwell, M. Cretignier, H. Giles, C. E. Henze, J. Jenkins, C. Lovis, F. Murgas, F. Pepe, G. R. Ricker, M. E. Rose, S. Seager, D. Segransan, A. Suárez-Mascareño, S. Udry, R. Vanderspek, and A. Wyttenbach. Optical phase curve of the ultra-hot Jupiter WASP-121b. *Astronomy and Astrophysics*, 637: A36, May 2020. doi: 10.1051/0004-6361/201936647.

A. Burrows, D. Sudarsky, and I. Hubeny. L and T Dwarf Models and the L to T Transition. *The Astrophysical Journal*, 640(2):1063–1077, Apr. 2006. doi: 10.1086/500293.

D. Charbonneau, L. E. Allen, S. T. Megeath, G. Torres, R. Alonso, T. M. Brown, R. L. Gilliland, D. W. Latham, G. Mandushev, F. T. O'Donovan, and A. Sozzetti. Detection of Thermal Emission from an Extrasolar Planet. *The Astrophysical Journal*, 626(1): 523–529, June 2005. doi: 10.1086/429991.

B. Charnay, J. M. Mendonça, L. Kreidberg, N. B. Cowan, J. Taylor, T. J. Bell, O. Demangeon, B. Edwards, C. A. Haswell, G. Morello, L. V. Mugnai, E. Pascale, G. Tinetti, P. Tremblin, and R. T. Zellem. A survey of exoplanet phase curves with Ariel. *arXiv e-prints*, art. arXiv:2102.06523, Feb. 2021.

G. Chen, R. van Boekel, H. Wang, N. Nikolov, J. J. Fortney, U. Seemann, W. Wang, L. Mancini, and T. Henning. Broad-band transmission spectrum and K-band thermal emission of WASP-43b as observed from the ground. *Astronomy and Astrophysics*, 563: A40, Mar. 2014. doi: 10.1051/0004-6361/201322740.

J. Y. K. Cho, J. W. Skinner, and H. T. Thrastarson. Storms, Variability, and Multiple Equilibria on Hot Jupiters. *The Astrophysical Journal Letters*, 913(2):L32, June 2021. doi: 10.3847/2041-8213/abfd37.

K. A. Collins, J. F. Kielkopf, and K. G. Stassun. Transit Timing Variation Measurements of WASP-12b and Qatar-1b: No Evidence Of Additional Planets. *The Astronomical Journal*, 153(2):78, Feb. 2017. doi: 10.3847/1538-3881/153/2/78.

N. B. Cowan and E. Agol. Inverting Phase Functions to Map Exoplanets. *The Astrophysical Journal Letters*, 678(2):L129, May 2008. doi: 10.1086/588553.

N. B. Cowan and E. Agol. The Statistics of Albedo and Heat Recirculation on Hot Exoplanets. *The Astrophysical Journal*, 729(1):54, Mar. 2011a. doi: 10.1088/0004-637X/729/1/54.

N. B. Cowan and E. Agol. A Model for Thermal Phase Variations of Circular and Eccentric Exoplanets. *The Astrophysical Journal*, 726(2):82, Jan. 2011b. doi: 10.1088/0004-637X/726/2/82.

N. B. Cowan, E. Agol, and D. Charbonneau. Hot nights on extrasolar planets: mid-infrared phase variations of hot Jupiters. *Monthly Notices of the Royal Astronomical Society*, 379(2):641–646, Aug. 2007. doi: 10.1111/j.1365-2966.2007.11897.x.

N. B. Cowan, P. Machalek, B. Croll, L. M. Shekhtman, A. Burrows, D. Deming, T. Greene, and J. L. Hora. Thermal Phase Variations of WASP-12b: Defying Predictions. *The Astrophysical Journal*, 747(1):82, Mar. 2012. doi: 10.1088/0004-637X/747/1/82.

N. B. Cowan, P. A. Fuentes, and H. M. Haggard. Light curves of stars and exoplanets: estimating inclination, obliquity and albedo. *Monthly Notices of the Royal Astronomical Society*, 434(3):2465–2479, Sept. 2013. doi: 10.1093/mnras/stt1191.

N. B. Cowan, V. Chayes, É. Bouffard, M. Meynig, and H. M. Haggard. Odd Harmonics in Exoplanet Photometry: Weather or Artifact? *Monthly Notices of the Royal Astronomical Society*, 467(1):747–757, May 2017. doi: 10.1093/mnras/stx133.

P. Cruz, D. Barrado, J. Lillo-Box, M. Diaz, J. Birkby, M. López-Morales, and J. J. Fortney. Detection of the secondary eclipse of Qatar-1b in the Ks band. *Astronomy and Astrophysics*, 595:A61, Oct. 2016. doi: 10.1051/0004-6361/201526333.

P. Cubillos, J. Harrington, N. Madhusudhan, K. B. Stevenson, R. A. Hardy, J. Blecic, D. R. Anderson, M. Hardin, and C. J. Campo. WASP-8b: Characterization of a Cool and Eccentric Exoplanet with Spitzer. *The Astrophysical Journal*, 768(1):42, May 2013. doi: 10.1088/0004-637X/768/1/42.

P. E. Cubillos, D. Keating, N. B. Cowan, J. M. Vos, B. Burningham, M. Ygouf, T. Karalidi, Y. Zhou, and E. C. Gonzales. Longitudinally Resolved Spectral Retrieval. *Submitted to AAS Journals.*, 2021.

F. Dai, J. N. Winn, L. Yu, and S. Albrecht. The Stellar Obliquity, Planet Mass, and Very Low Albedo of Qatar-2 from K2 Photometry. *The Astronomical Journal*, 153(1):40, Jan. 2017. doi: 10.3847/1538-3881/153/1/40.

L. Dang, N. B. Cowan, J. C. Schwartz, E. Rauscher, M. Zhang, H. A. Knutson, M. Line, I. Dobbs-Dixon, D. Deming, S. Sundararajan, J. J. Fortney, and M. Zhao. Detection of a westward hotspot offset in the atmosphere of hot gas giant CoRoT-2b. *Nature Astronomy*, 2:220–227, Mar. 2018. doi: 10.1038/s41550-017-0351-6.

R. I. Dawson and D. C. Fabrycky. Radial Velocity Planets De-aliased: A New, Short Period for Super-Earth 55 Cnc e. *The Astrophysical Journal*, 722(1):937–953, Oct. 2010. doi: 10.1088/0004-637X/722/1/937.

T. Daylan, M. N. Günther, T. Mikal-Evans, D. K. Sing, I. Wong, A. Shporer, P. Niraula, J. de Wit, D. D. B. Koll, V. Parmentier, T. Fetherolf, S. R. Kane, G. R. Ricker, R. Vanderspek, S. Seager, J. N. Winn, J. M. Jenkins, D. A. Caldwell, D. Charbonneau, C. E. Henze, M. Paegert, S. Rinehart, M. Rose, L. Sha, E. Quintana, and J. N. Villasenor. TESS observations of the WASP-121 b phase curve. *arXiv e-prints*, art. arXiv:1909.03000, Sept. 2019.

J. de Wit, M. Gillon, B. O. Demory, and S. Seager. Towards consistent mapping of distant worlds: secondary-eclipse scanning of the exoplanet HD 189733b. *Astronomy and Astrophysics*, 548:A128, Dec. 2012. doi: 10.1051/0004-6361/201219060.

D. Deming and H. A. Knutson. Highlights of exoplanetary science from Spitzer. *Nature Astronomy*, 4:453–466, May 2020. doi: 10.1038/s41550-020-1100-9.

D. Deming, S. Seager, L. J. Richardson, and J. Harrington. Infrared radiation from an extrasolar planet. *Nature*, 434(7034):740–743, Mar. 2005. doi: 10.1038/nature03507.

D. Deming, H. Knutson, J. Kammer, B. J. Fulton, J. Ingalls, S. Carey, A. Burrows, J. J. Fortney, K. Todorov, E. Agol, N. Cowan, J.-M. Desert, J. Fraine, J. Langton, C. Morley, and A. P. Showman. Spitzer Secondary Eclipses of the Dense, Modestly-irradiated, Giant Exoplanet HAT-P-20b Using Pixel-level Decorrelation. *The Astrophysical Journal*, 805(2):132, June 2015. doi: 10.1088/0004-637X/805/2/132.

B.-O. Demory, J. de Wit, N. Lewis, J. Fortney, A. Zsom, S. Seager, H. Knutson, K. Heng, N. Madhusudhan, M. Gillon, T. Barclay, J.-M. Desert, V. Parmentier, and N. B.

Cowan. Inference of Inhomogeneous Clouds in an Exoplanet Atmosphere. *The Astrophysical Journal Letters*, 776(2):L25, Oct. 2013. doi: 10.1088/2041-8205/776/2/L25.

B.-O. Demory, M. Gillon, N. Madhusudhan, and D. Queloz. Variability in the super-Earth 55 Cnc e. *Monthly Notices of the Royal Astronomical Society*, 455(2):2018–2027, Jan. 2016. doi: 10.1093/mnras/stv2239.

D. Dragomir, I. J. M. Crossfield, B. Benneke, I. Wong, T. Daylan, M. Diaz, D. Deming, P. Molliere, L. Kreidberg, J. S. Jenkins, D. Berardo, J. L. Christiansen, C. D. Dressing, V. Gorjian, S. R. Kane, T. Mikal-Evans, F. Y. Morales, M. Werner, G. R. Ricker, R. Vanderspek, S. Seager, J. N. Winn, J. M. Jenkins, K. D. Colón, W. Fong, N. Guerrero, K. Hesse, H. P. Osborn, M. E. Rose, J. C. Smith, and E. B. Ting. Spitzer Reveals Evidence of Molecular Absorption in the Atmosphere of the Hot Neptune LTT 9779b. *The Astrophysical Journal Letters*, 903(1):L6, Nov. 2020. doi: 10.3847/2041-8213/abbc70.

M. Esposito, E. Covino, S. Desidera, L. Mancini, V. Nascimbeni, R. Zanmar Sanchez, K. Biazzo, A. F. Lanza, G. Leto, J. Southworth, A. S. Bonomo, A. Suárez Mascareño, C. Boccato, R. Cosentino, R. U. Claudi, R. Gratton, A. Maggio, G. Micela, E. Molinari, I. Pagano, G. Piotto, E. Poretti, R. Smareglia, A. Sozzetti, L. Affer, D. R. Anderson, G. Andreuzzi, S. Benatti, A. Bignamini, F. Borsa, L. Borsato, S. Ciceri, M. Damasso, L. di Fabrizio, P. Giacobbe, V. Granata, A. Harutyunyan, T. Henning, L. Malavolta, J. Maldonado, A. Martinez Fiorenzano, S. Masiero, P. Molaro, M. Molinaro, M. Pedani, M. Rainer, G. Scandariato, and O. D. Turner. The GAPS Programme with HARPS-N at TNG. XIII. The orbital obliquity of three close-in massive planets hosted by dwarf K-type stars: WASP-43, HAT-P-20 and Qatar-2. *Astronomy and Astrophysics*, 601: A53, May 2017. doi: 10.1051/0004-6361/201629720.

T. M. Evans, S. Aigrain, N. Gibson, J. K. Barstow, D. S. Amundsen, P. Tremblin, and P. Mourier. A uniform analysis of HD 209458b Spitzer/IRAC light curves with Gaussian process models. *Monthly Notices of the Royal Astronomical Society*, 451(1):680–694, July 2015. doi: 10.1093/mnras/stv910.

G. G. Fazio, J. L. Hora, L. E. Allen, M. L. N. Ashby, P. Barmby, L. K. Deutsch, J. S. Huang, S. Kleiner, M. Marengo, S. T. Megeath, G. J. Melnick, M. A. Pahre, B. M. Patten, J. Polizotti, H. A. Smith, R. S. Taylor, Z. Wang, S. P. Willner, W. F. Hoffmann, J. L. Pipher, W. J. Forrest, C. W. McMurty, C. R. McCreight, M. E. McKelvey, R. E. McMurray, D. G. Koch, S. H. Moseley, R. G. Arendt, J. E. Mentzell, C. T. Marx, P. Losch, P. Mayman, W. Eichhorn, D. Krebs, M. Jhabvala, D. Y. Gezari, D. J. Fixsen, J. Flores, K. Shakoorzadeh, R. Jungo, C. Hakun, L. Workman, G. Karpati, R. Kichak, R. Whitley, S. Mann, E. V. Tollestrup, P. Eisenhardt, D. Stern, V. Gorjian, B. Bhattacharya, S. Carey, B. O. Nelson, W. J. Glaccum, M. Lacy, P. J. Lowrance, S. Laine, W. T. Reach, J. A. Stauffer, J. A. Surace, G. Wilson, E. L. Wright, A. Hoffman, G. Domingo, and M. Cohen. The Infrared Array Camera (IRAC) for the Spitzer Space Telescope. *The Astrophysical Journal, Supplement*, 154(1):10–17, Sept. 2004. doi: 10.1086/422843.

D. A. Fischer, G. W. Marcy, R. P. Butler, S. S. Vogt, G. Laughlin, G. W. Henry, D. Abouav, K. M. G. Peek, J. T. Wright, J. A. Johnson, C. McCarthy, and H. Isaacson. Five Planets Orbiting 55 Cancri. *The Astrophysical Journal*, 675(1):790–801, Mar. 2008. doi: 10.1086/525512.

D. Foreman-Mackey, D. W. Hogg, D. Lang, and J. Goodman. emcee: The MCMC Hammer. *Publications of the ASP*, 125(925):306, Mar. 2013. doi: 10.1086/670067.

D. Foreman-Mackey, A. Savel, R. Luger, E. Agol, I. Czekala, A. Price-Whelan, C. Hedges, E. Gilbert, L. Bouma, T. Barclay, and T. D. Brandt. exoplanet-dev/exoplanet v0.5.0, May 2021. URL `https://doi.org/10.5281/zenodo.1998447`.

J. J. Fortney, R. I. Dawson, and T. D. Komacek. Hot Jupiters: Origins, Structure, Atmospheres. *arXiv e-prints*, art. arXiv:2102.05064, Feb. 2021.

P. Gao, D. P. Thorngren, G. K. H. Lee, J. J. Fortney, C. V. Morley, H. R. Wakeford, D. K. Powell, K. B. Stevenson, and X. Zhang. Aerosol composition of hot giant exoplanets dominated by silicates and hydrocarbon hazes. *Nature Astronomy*, 4:951–956, May 2020. doi: 10.1038/s41550-020-1114-3.

E. Garhart, D. Deming, A. Mandell, H. Knutson, and J. J. Fortney. Spitzer secondary eclipses of Qatar-1b. *Astronomy and Astrophysics*, 610:A55, Feb. 2018. doi: 10.1051/0004-6361/201731637.

E. Garhart, D. Deming, A. Mandell, H. A. Knutson, N. Wallack, A. Burrows, J. J. Fortney, C. Hood, C. Seay, D. K. Sing, B. Benneke, J. D. Fraine, T. Kataria, N. Lewis, N. Madhusudhan, P. McCullough, K. B. Stevenson, and H. Wakeford. Statistical Characterization of Hot Jupiter Atmospheres Using Spitzer's Secondary Eclipses. *The Astronomical Journal*, 159(4):137, Apr. 2020. doi: 10.3847/1538-3881/ab6cff.

B. S. Gaudi, K. G. Stassun, K. A. Collins, T. G. Beatty, G. Zhou, D. W. Latham, A. Bieryla, J. D. Eastman, R. J. Siverd, J. R. Crepp, E. J. Gonzales, D. J. Stevens, L. A. Buchhave, J. Pepper, M. C. Johnson, K. D. Colon, E. L. N. Jensen, J. E. Rodriguez, V. Bozza, S. C. Novati, G. D'Ago, M. T. Dumont, T. Ellis, C. Gaillard, H. Jang-Condell, D. H. Kasper, A. Fukui, J. Gregorio, A. Ito, J. F. Kielkopf, M. Manner, K. Matt, N. Narita, T. E. Oberst, P. A. Reed, G. Scarpetta, D. C. Stephens, R. R. Yeigh, R. Zambelli, B. J. Fulton, A. W. Howard, D. J. James, M. Penny, D. Bayliss, I. A. Curtis, D. L. Depoy, G. A. Esquerdo, A. Gould, M. D. Joner, R. B. Kuhn, J. Labadie-Bartz, M. B. Lund, J. L. Marshall, K. K. McLeod, R. W. Pogge, H. Relles, C. Stockdale, T. G. Tan, M. Trueblood, and P. Trueblood. A giant planet undergoing extreme-ultraviolet irradiation by its hot massive-star host. *Nature*, 546(7659):514–518, June 2017. doi: 10.1038/nature22392.

B. S. Gaudi, J. L. Christiansen, and M. R. Meyer. The Demographics of Exoplanets. *arXiv e-prints*, art. arXiv:2011.04703, Nov. 2020.

A. Gelman, J. B. Carlin, H. S. Stern, D. D. B., A. Vehtari, and D. B. Rubin. *Bayesian Data Analysis, (3rd ed.).* Boca Raton : CRC Press, 2014.

A. Gelman, D. Simpson, and M. Betancourt. The Prior Can Often Only Be Understood in the Context of the Likelihood. *Entropy*, 19(10):555, Oct. 2017. doi: 10.3390/e19100555.

M. Gillon, A. H. M. J. Triaud, J. J. Fortney, B. O. Demory, E. Jehin, M. Lendl, P. Magain,

P. Kabath, D. Queloz, R. Alonso, D. R. Anderson, A. Collier Cameron, A. Fumel, L. Hebb, C. Hellier, A. Lanotte, P. F. L. Maxted, N. Mowlavi, and B. Smalley. The TRAPPIST survey of southern transiting planets. I. Thirty eclipses of the ultra-short period planet WASP-43 b. *Astronomy and Astrophysics*, 542:A4, June 2012. doi: 10.1051/0004-6361/201218817.

C. J. Hansen, J. C. Schwartz, and N. B. Cowan. Features in the broad-band eclipse spectra of exoplanets: signal or noise? *Monthly Notices of the Royal Astronomical Society*, 444(4):3632–3640, Nov. 2014. doi: 10.1093/mnras/stu1699.

C. K. Harada, E. M. R. Kempton, E. Rauscher, M. Roman, I. Malsky, M. Brinjikji, and V. DiTomasso. Signatures of Clouds in Hot Jupiter Atmospheres: Modeled High-resolution Emission Spectra from 3D General Circulation Models. *The Astrophysical Journal*, 909(1):85, Mar. 2021. doi: 10.3847/1538-4357/abdc22.

C. Hellier, D. R. Anderson, A. Collier Cameron, M. Gillon, E. Jehin, M. Lendl, P. F. L. Maxted, F. Pepe, D. Pollacco, D. Queloz, D. Ségransan, B. Smalley, A. M. S. Smith, J. Southworth, A. H. M. J. Triaud, S. Udry, and R. G. West. WASP-43b: the closest-orbiting hot Jupiter. *Astronomy and Astrophysics*, 535:L7, Nov. 2011. doi: 10.1051/0004-6361/201117081.

C. Helling, D. Lewis, D. Samra, L. Carone, V. Graham, O. Herbort, K. L. Chubb, M. Min, R. Waters, V. Parmentier, and N. Mayne. Cloud property trends in hot and ultra-hot giant gas planets (WASP-43b, WASP-103b, WASP-121b, HAT-P-7b, and WASP-18b). *arXiv e-prints*, art. arXiv:2102.11688, Feb. 2021.

K. Heng and B.-O. Demory. Understanding Trends Associated with Clouds in Irradiated Exoplanets. *The Astrophysical Journal*, 777(2):100, Nov. 2013. doi: 10.1088/0004-637X/777/2/100.

K. Heng and A. P. Showman. Atmospheric Dynamics of Hot Exoplanets. *Annual Review of Earth and Planetary Sciences*, 43:509–540, May 2015. doi: 10.1146/annurev-earth-060614-105146.

A. W. Hindle, P. J. Bushby, and T. M. Rogers. Shallow-water Magnetohydrodynamics for Westward Hotspots on Hot Jupiters. *The Astrophysical Journal Letters*, 872(2): L27, Feb. 2019. doi: 10.3847/2041-8213/ab05dd.

J. R. Houck, T. L. Roellig, J. Van Cleve, W. J. Forrest, T. L. Herter, C. R. Lawrence, K. Matthews, H. J. Reitsema, B. T. Soifer, D. M. Watson, D. Weedman, M. Huisjen, J. R. Troeltzsch, D. J. Barry, J. Bernard-Salas, C. Blacken, B. R. Brandl, V. Charmandaris, D. Devost, G. E. Gull, P. Hall, C. P. Henderson, S. J. U. Higdon, B. E. Pirger, J. Schoenwald, G. C. Sloan, K. I. Uchida, P. N. Appleton, L. Armus, M. J. Burgdorf, S. B. Fajardo-Acosta, C. J. Grillmair, J. G. Ingalls, P. W. Morris, and H. I. Teplitz. The infrared spectrograph on the Spitzer Space Telescope. In J. C. Mather, editor, *Optical, Infrared, and Millimeter Space Telescopes*, volume 5487 of *Society of Photo-Optical Instrumentation Engineers (SPIE) Conference Series*, pages 62–76, Oct. 2004. doi: 10.1117/12.550517.

S. Hoyer, E. Pallé, D. Dragomir, and F. Murgas. Ruling out the Orbital Decay of the WASP-43b Exoplanet. *The Astronomical Journal*, 151(6):137, June 2016. doi: 10.3847/0004-6256/151/6/137.

J. G. Ingalls, J. E. Krick, S. J. Carey, S. Laine, J. A. Surace, W. J. Glaccum, C. C. Grillmair, and P. J. Lowrance. Intra-pixel gain variations and high-precision photometry with the Infrared Array Camera (IRAC). In M. C. Clampin, G. G. Fazio, H. A. MacEwen, and J. Oschmann, Jacobus M., editors, *Space Telescopes and Instrumentation 2012: Optical, Infrared, and Millimeter Wave*, volume 8442 of *Society of Photo-Optical Instrumentation Engineers (SPIE) Conference Series*, page 84421Y, Sept. 2012. doi: 10.1117/12.926947.

J. G. Ingalls, J. E. Krick, S. J. Carey, J. R. Stauffer, P. J. Lowrance, C. J. Grillmair, D. Buzasi, D. Deming, H. Diamond-Lowe, T. M. Evans, G. Morello, K. B. Stevenson, I. Wong, P. Capak, W. Glaccum, S. Laine, J. Surace, and L. Storrie-Lombardi. Repeatability and Accuracy of Exoplanet Eclipse Depths Measured with Post-cryogenic Spitzer. *The Astronomical Journal*, 152(2):44, Aug. 2016. doi: 10.3847/0004-6256/152/2/44.

A. R. Iyer, M. R. Swain, R. T. Zellem, M. R. Line, G. Roudier, G. Rocha, and J. H. Livingston. A Characteristic Transmission Spectrum Dominated by H_2O Applies to the Majority of HST/WFC3 Exoplanet Observations. *The Astrophysical Journal*, 823 (2):109, June 2016. doi: 10.3847/0004-637X/823/2/109.

T. Kataria, A. P. Showman, J. J. Fortney, K. B. Stevenson, M. R. Line, L. Kreidberg, J. L. Bean, and J.-M. Désert. The Atmospheric Circulation of the Hot Jupiter WASP-43b: Comparing Three-dimensional Models to Spectrophotometric Data. *The Astrophysical Journal*, 801(2):86, Mar. 2015. doi: 10.1088/0004-637X/801/2/86.

D. Keating and N. B. Cowan. Revisiting the Energy Budget of WASP-43b: Enhanced Day-Night Heat Transport. *The Astrophysical Journal Letters*, 849(1):L5, Nov. 2017. doi: 10.3847/2041-8213/aa8b6b.

D. Keating, N. B. Cowan, and L. Dang. Uniformly hot nightside temperatures on short-period gas giants. *Nature Astronomy*, 3:1092–1098, Aug. 2019. doi: 10.1038/s41550-019-0859-z.

D. Keating, K. B. Stevenson, N. B. Cowan, E. Rauscher, J. L. Bean, T. Bell, L. Dang, D. Deming, J.-M. Désert, Y. K. Feng, J. J. Fortney, T. Kataria, E. M. R. Kempton, N. Lewis, M. R. Line, M. Mansfield, E. May, C. Morley, and A. P. Showman. Smaller than Expected Bright-spot Offsets in Spitzer Phase Curves of the Hot Jupiter Qatar-1b. *The Astronomical Journal*, 159(5):225, May 2020. doi: 10.3847/1538-3881/ab83f4.

B. M. Kilpatrick, T. Kataria, N. K. Lewis, R. T. Zellem, G. W. Henry, N. B. Cowan, J. de Wit, J. J. Fortney, H. Knutson, S. Seager, A. P. Showman, and G. S. Tucker. Evaluating Climate Variability of the Canonical Hot-Jupiters HD 189733b and HD 209458b through Multi-epoch Eclipse Observations. *The Astronomical Journal*, 159 (2):51, Feb. 2020. doi: 10.3847/1538-3881/ab6223.

D. M. Kipping. Binning is sinning: morphological light-curve distortions due to finite integration time. *Monthly Notices of the Royal Astronomical Society*, 408(3):1758–1769, Nov. 2010. doi: 10.1111/j.1365-2966.2010.17242.x.

D. M. Kipping and D. S. Spiegel. Detection of visible light from the darkest world. *Monthly Notices of the Royal Astronomical Society*, 417(1):L88–L92, Oct. 2011. doi: 10.1111/j.1745-3933.2011.01127.x.

H. A. Knutson, D. Charbonneau, L. E. Allen, J. J. Fortney, E. Agol, N. B. Cowan, A. P. Showman, C. S. Cooper, and S. T. Megeath. A map of the day-night contrast of the extrasolar planet HD 189733b. *Nature*, 447(7141):183–186, May 2007. doi: 10.1038/nature05782.

H. A. Knutson, D. Charbonneau, N. B. Cowan, J. J. Fortney, A. P. Showman, E. Agol, G. W. Henry, M. E. Everett, and L. E. Allen. Multiwavelength Constraints on the Day-Night Circulation Patterns of HD 189733b. *The Astrophysical Journal*, 690(1): 822–836, Jan. 2009. doi: 10.1088/0004-637X/690/1/822.

H. A. Knutson, N. Lewis, J. J. Fortney, A. Burrows, A. P. Showman, N. B. Cowan, E. Agol, S. Aigrain, D. Charbonneau, D. Deming, J.-M. Désert, G. W. Henry, J. Langton, and G. Laughlin. 3.6 and 4.5 μm Phase Curves and Evidence for Non-equilibrium Chemistry in the Atmosphere of Extrasolar Planet HD 189733b. *The Astrophysical Journal*, 754(1):22, July 2012. doi: 10.1088/0004-637X/754/1/22.

T. D. Komacek and A. P. Showman. Atmospheric Circulation of Hot Jupiters: Dayside-Nightside Temperature Differences. *The Astrophysical Journal*, 821(1):16, Apr. 2016. doi: 10.3847/0004-637X/821/1/16.

T. D. Komacek and A. P. Showman. Temporal Variability in Hot Jupiter Atmospheres. *The Astrophysical Journal*, 888(1):2, Jan. 2020. doi: 10.3847/1538-4357/ab5b0b.

T. D. Komacek and X. Tan. Effects of Dissociation/Recombination on the Day-Night Temperature Contrasts of Ultra-hot Jupiters. *Research Notes of the American Astronomical Society*, 2(2):36, May 2018. doi: 10.3847/2515-5172/aac5e7.

T. D. Komacek, A. P. Showman, and X. Tan. Atmospheric Circulation of Hot Jupiters: Dayside-Nightside Temperature Differences. II. Comparison with Observations. *The Astrophysical Journal*, 835(2):198, Feb. 2017. doi: 10.3847/1538-4357/835/2/198.

V. B. Kostov, J. A. Orosz, A. D. Feinstein, W. F. Welsh, W. Cukier, N. Haghighipour, B. Quarles, D. V. Martin, B. T. Montet, G. Torres, A. H. M. J. Triaud, T. Barclay, P. Boyd, C. Briceno, A. C. Cameron, A. C. M. Correia, E. A. Gilbert, S. Gill, M. Gillon, J. Haqq-Misra, C. Hellier, C. Dressing, D. C. Fabrycky, G. Furesz, J. M. Jenkins, S. R. Kane, R. Kopparapu, V. K. Hodžić, D. W. Latham, N. Law, A. M. Levine, G. Li, C. Lintott, J. J. Lissauer, A. W. Mann, T. Mazeh, R. Mardling, P. F. L. Maxted, N. Eisner, F. Pepe, J. Pepper, D. Pollacco, S. N. Quinn, E. V. Quintana, J. F. Rowe, G. Ricker, M. E. Rose, S. Seager, A. Santerne, D. Ségransan, D. R. Short, J. C. Smith, M. R. Standing, A. Tokovinin, T. Trifonov, O. Turner, J. D. Twicken, S. Udry, R. Vanderspek, J. N. Winn, E. T. Wolf, C. Ziegler, P. Ansorge, F. Barnet, J. Bergeron, M. Huten, G. Pappa, and T. van der Straeten. TOI-1338: TESS' First Transiting Circumbinary Planet. *The Astronomical Journal*, 159(6):253, June 2020. doi: 10.3847/1538-3881/ab8a48.

L. Kreidberg. batman: BAsic Transit Model cAlculatioN in Python. *Publications of the ASP*, 127(957):1161, Nov. 2015. doi: 10.1086/683602.

L. Kreidberg, M. R. Line, V. Parmentier, K. B. Stevenson, T. Louden, M. Bonnefoy, J. K. Faherty, G. W. Henry, M. H. Williamson, K. Stassun, T. G. Beatty, J. L. Bean, J. J. Fortney, A. P. Showman, J.-M. Désert, and J. Arcangeli. Global Climate and Atmospheric Composition of the Ultra-hot Jupiter WASP-103b from HST and Spitzer Phase Curve Observations. *The Astronomical Journal*, 156(1):17, July 2018. doi: 10.3847/1538-3881/aac3df.

J. E. Krick, J. Fraine, J. Ingalls, and S. Deger. Random Forests Applied to High-precision Photometry Analysis with Spitzer IRAC. *The Astronomical Journal*, 160(3):99, Sept. 2020. doi: 10.3847/1538-3881/aba11f.

G. Lee, I. Dobbs-Dixon, C. Helling, K. Bognar, and P. Woitke. Dynamic mineral clouds on HD 189733b. I. 3D RHD with kinetic, non-equilibrium cloud formation. *Astronomy and Astrophysics*, 594:A48, Oct. 2016. doi: 10.1051/0004-6361/201628606.

G. K. H. Lee, K. Wood, I. Dobbs-Dixon, A. Rice, and C. Helling. Dynamic mineral clouds on HD 189733b. II. Monte Carlo radiative transfer for 3D cloudy exoplanet atmospheres: combining scattering and emission spectra. *Astronomy and Astrophysics*, 601:A22, May 2017. doi: 10.1051/0004-6361/201629804.

N. K. Lewis, A. P. Showman, J. J. Fortney, M. S. Marley, R. S. Freedman, and K. Lodders. Atmospheric Circulation of Eccentric Hot Neptune GJ436b. *The Astrophysical Journal*, 720(1):344–356, Sept. 2010. doi: 10.1088/0004-637X/720/1/344.

N. K. Lewis, H. A. Knutson, A. P. Showman, N. B. Cowan, G. Laughlin, A. Burrows, D. Deming, J. R. Crepp, K. J. Mighell, E. Agol, G. Á. Bakos, D. Charbonneau, J.-M. Désert, D. A. Fischer, J. J. Fortney, J. D. Hartman, S. Hinkley, A. W. Howard, J. A. Johnson, M. Kao, J. Langton, and G. W. Marcy. Orbital Phase Variations of the Eccentric Giant Planet HAT-P-2b. *The Astrophysical Journal*, 766(2):95, Apr. 2013. doi: 10.1088/0004-637X/766/2/95.

S. Lines, N. J. Mayne, J. Manners, I. A. Boutle, B. Drummond, T. Mikal-Evans, K. Kohary, and D. K. Sing. Overcast on Osiris: 3D radiative-hydrodynamical simulations of a cloudy hot Jupiter using the parametrized, phase-equilibrium cloud formation code EDDYSED. *Monthly Notices of the Royal Astronomical Society*, 488(1):1332–1355, Sept. 2019. doi: 10.1093/mnras/stz1788.

M. López-Morales and S. Seager. Thermal Emission from Transiting Very Hot Jupiters: Prospects for Ground-based Detection at Optical Wavelengths. *The Astrophysical Journal Letters*, 667(2):L191–L194, Oct. 2007. doi: 10.1086/522118.

T. Louden and L. Kreidberg. SPIDERMAN: an open-source code to model phase curves and secondary eclipses. *Monthly Notices of the Royal Astronomical Society*, 477(2): 2613–2627, June 2018. doi: 10.1093/mnras/sty558.

R. Luger, E. Agol, D. Foreman-Mackey, D. P. Fleming, J. Lustig-Yaeger, and R. Deitrick. starry: Analytic Occultation Light Curves. *The Astronomical Journal*, 157(2):64, Feb. 2019. doi: 10.3847/1538-3881/aae8e5.

N. B. Lust, D. Britt, J. Harrington, S. Nymeyer, K. B. Stevenson, E. L. Ross, W. Bowman, and J. Fraine. Least Asymmetry Centering Method and Comparisons. *Publications of the ASP*, 126(946):1092, Dec. 2014. doi: 10.1086/679470.

C. Majeau, E. Agol, and N. B. Cowan. A Two-dimensional Infrared Map of the Extrasolar Planet HD 189733b. *The Astrophysical Journal Letters*, 747(2):L20, Mar. 2012. doi: 10.1088/2041-8205/747/2/L20.

K. Mandel and E. Agol. Analytic Light Curves for Planetary Transit Searches. *The Astrophysical Journal Letters*, 580(2):L171–L175, Dec. 2002. doi: 10.1086/345520.

M. Mansfield, E. Schlawin, J. Lustig-Yaeger, A. D. Adams, E. Rauscher, J. Arcangeli, Y. K. Feng, P. Gupta, D. Keating, K. B. Stevenson, and T. G. Beatty. Eigenspectra: a framework for identifying spectra from 3D eclipse mapping. *Monthly Notices of the Royal Astronomical Society*, 499(4):5151–5162, Dec. 2020a. doi: 10.1093/mnras/staa3179.

M. Mansfield, E. Schlawin, J. Lustig-Yaeger, A. D. Adams, E. Rauscher, J. Arcangeli, Y. K. Feng, P. Gupta, D. Keating, K. B. Stevenson, and T. G. Beatty. Eigenspectra: a framework for identifying spectra from 3D eclipse mapping. *Monthly Notices of the Royal Astronomical Society*, 499(4):5151–5162, Dec. 2020b. doi: 10.1093/mnras/staa3179.

P. F. L. Maxted, D. R. Anderson, A. P. Doyle, M. Gillon, J. Harrington, N. Iro, E. Jehin, D. Lafrenière, B. Smalley, and J. Southworth. Spitzer 3.6 and 4.5 μm full-orbit light curves of WASP-18. *Monthly Notices of the Royal Astronomical Society*, 428(3):2645–2660, Jan. 2013. doi: 10.1093/mnras/sts231.

E. M. May and K. B. Stevenson. Introducing a New Spitzer Master BLISS Map to Remove the Instrument Systematic Phase-curve-parameter Degeneracy, as Demonstrated by a Reanalysis of the 4.5 μm WASP-43b Phase Curve. *The Astronomical Journal*, 160(3):140, Sept. 2020. doi: 10.3847/1538-3881/aba833.

B. E. McArthur, M. Endl, W. D. Cochran, G. F. Benedict, D. A. Fischer, G. W. Marcy, R. P. Butler, D. Naef, M. Mayor, D. Queloz, S. Udry, and T. E. Harrison. Detection of a Neptune-Mass Planet in the ρ^1 Cancri System Using the Hobby-Eberly Telescope. *The Astrophysical Journal Letters*, 614(1):L81–L84, Oct. 2004. doi: 10.1086/425561.

McElreath, R. *Statistical Rethinking, (2nd ed.)*. Boca Raton : CRC Press, 2020.

J. M. Mendonça, M. Malik, B.-O. Demory, and K. Heng. Revisiting the Phase Curves of WASP-43b: Confronting Re-analyzed Spitzer Data with Cloudy Atmospheres. *The Astronomical Journal*, 155(4):150, Apr. 2018. doi: 10.3847/1538-3881/aaaebc.

K. Menou. Magnetic Scaling Laws for the Atmospheres of Hot Giant Exoplanets. *The Astrophysical Journal*, 745(2):138, Feb. 2012. doi: 10.1088/0004-637X/745/2/138.

G. Morello, I. P. Waldmann, G. Tinetti, G. Peres, G. Micela, and I. D. Howarth. A New Look at Spitzer Primary Transit Observations of the Exoplanet HD 189733b. *The Astrophysical Journal*, 786(1):22, May 2014. doi: 10.1088/0004-637X/786/1/22.

G. Morello, I. P. Waldmann, and G. Tinetti. Repeatability of Spitzer/IRAC Exoplanetary Eclipses with Independent Component Analysis. *The Astrophysical Journal*, 820(2):86, Apr. 2016. doi: 10.3847/0004-637X/820/2/86.

G. Morello, C. Danielski, D. Dickens, P. Tremblin, and P. O. Lagage. An Independent Analysis of the Spitzer/IRAC Phase Curves of WASP43 b. *The Astronomical Journal*, 157(5):205, May 2019. doi: 10.3847/1538-3881/ab14e2.

C. V. Morley, J. J. Fortney, M. S. Marley, C. Visscher, D. Saumon, and S. K. Leggett. Neglected Clouds in T and Y Dwarf Atmospheres. *The Astrophysical Journal*, 756(2):172, Sept. 2012. doi: 10.1088/0004-637X/756/2/172.

C. V. Morley, H. Knutson, M. Line, J. J. Fortney, D. Thorngren, M. S. Marley, D. Teal, and R. Lupu. Forward and Inverse Modeling of the Emission and Transmission Spectrum of GJ 436b: Investigating Metal Enrichment, Tidal Heating, and Clouds. *The Astronomical Journal*, 153(2):86, Feb. 2017. doi: 10.3847/1538-3881/153/2/86.

M. Morvan, N. Nikolaou, A. Tsiaras, and I. P. Waldmann. Detrending Exoplanetary Transit Light Curves with Long Short-term Memory Networks. *The Astronomical Journal*, 159(3):109, Mar. 2020. doi: 10.3847/1538-3881/ab6aa7.

A. R. Neil and L. A. Rogers. A Joint Mass-Radius-Period Distribution of Exoplanets. *The Astrophysical Journal*, 891(1):12, Mar. 2020. doi: 10.3847/1538-4357/ab6a92.

V. Parmentier and I. J. M. Crossfield. *Exoplanet Phase Curves: Observations and Theory.* Springer International Publishing AG, 2018. doi: 10.1007/978-3-319-55333-7_116.

V. Parmentier, J. J. Fortney, A. P. Showman, C. Morley, and M. S. Marley. Transitions in the Cloud Composition of Hot Jupiters. *The Astrophysical Journal*, 828(1):22, Sept. 2016. doi: 10.3847/0004-637X/828/1/22.

V. Parmentier, A. P. Showman, and J. J. Fortney. The cloudy shape of hot Jupiter thermal phase curves. *Monthly Notices of the Royal Astronomical Society*, 501(1): 78–108, Jan. 2021. doi: 10.1093/mnras/staa3418.

E. K. Pass, N. B. Cowan, P. E. Cubillos, and J. G. Sklar. Estimating dayside effective temperatures of hot Jupiters and associated uncertainties through Gaussian process regression. *Monthly Notices of the Royal Astronomical Society*, 489(1):941–950, Oct. 2019. doi: 10.1093/mnras/stz2226.

D. Perez-Becker and A. P. Showman. Atmospheric Heat Redistribution on Hot Jupiters. *The Astrophysical Journal*, 776(2):134, Oct. 2013. doi: 10.1088/0004-637X/776/2/134.

R. Perna, K. Menou, and E. Rauscher. Magnetic Drag on Hot Jupiter Atmospheric Winds. *The Astrophysical Journal*, 719(2):1421–1426, Aug. 2010. doi: 10.1088/0004-637X/719/2/1421.

D. Powell, X. Zhang, P. Gao, and V. Parmentier. Formation of Silicate and Titanium Clouds on Hot Jupiters. *The Astrophysical Journal*, 860(1):18, June 2018. doi: 10.3847/1538-4357/aac215.

E. Rauscher and E. M. R. Kempton. The Atmospheric Circulation and Observable Properties of Non-synchronously Rotating Hot Jupiters. *The Astrophysical Journal*, 790(1): 79, July 2014. doi: 10.1088/0004-637X/790/1/79.

E. Rauscher and K. Menou. Three-dimensional Atmospheric Circulation Models of HD 189733b and HD 209458b with Consistent Magnetic Drag and Ohmic Dissipation. *The Astrophysical Journal*, 764(1):103, Feb. 2013. doi: 10.1088/0004-637X/764/1/103.

E. Rauscher, V. Suri, and N. B. Cowan. A More Informative Map: Inverting Thermal Orbital Phase and Eclipse Light Curves of Exoplanets. *The Astronomical Journal*, 156 (5):235, Nov. 2018. doi: 10.3847/1538-3881/aae57f.

T. M. Rogers. Constraints on the magnetic field strength of HAT-P-7 b and other hot giant exoplanets. *Nature Astronomy*, 1:0131, June 2017. doi: 10.1038/s41550-017-0131.

M. Roman and E. Rauscher. Modeling the Effects of Inhomogeneous Aerosols on the Hot Jupiter Kepler-7b's Atmospheric Circulation. *The Astrophysical Journal*, 850(1): 17, Nov. 2017. doi: 10.3847/1538-4357/aa8ee4.

M. Roman and E. Rauscher. Modeled Temperature-dependent Clouds with Radiative Feedback in Hot Jupiter Atmospheres. *The Astrophysical Journal*, 872(1):1, Feb. 2019. doi: 10.3847/1538-4357/aafdb5.

M. T. Roman, E. M. R. Kempton, E. Rauscher, C. K. Harada, J. L. Bean, and K. B. Stevenson. Clouds in Three-dimensional Models of Hot Jupiters over a Wide Range of Temperatures. I. Thermal Structures and Broadband Phase-curve Predictions. *The Astrophysical Journal*, 908(1):101, Feb. 2021. doi: 10.3847/1538-4357/abd549.

J. F. Rowe, J. M. Matthews, S. Seager, E. Miller-Ricci, D. Sasselov, R. Kuschnig, D. B. Guenther, A. F. J. Moffat, S. M. Rucinski, G. A. H. Walker, and W. W. Weiss. The Very Low Albedo of an Extrasolar Planet: MOST Space-based Photometry of HD 209458. *The Astrophysical Journal*, 689(2):1345–1353, Dec. 2008. doi: 10.1086/591835.

H. N. Russell. On the light variations of asteroids and satellites. *The Astrophysical Journal*, 24:1–18, July 1906. doi: 10.1086/141361.

P. Sarkis, C. Mordasini, T. Henning, G. D. Marleau, and P. Mollière. Evidence of three mechanisms explaining the radius anomaly of hot Jupiters. *Astronomy and Astrophysics*, 645:A79, Jan. 2021. doi: 10.1051/0004-6361/202038361.

J. C. Schwartz and N. B. Cowan. Balancing the energy budget of short-period giant planets: evidence for reflective clouds and optical absorbers. *Monthly Notices of the Royal Astronomical Society*, 449(4):4192–4203, June 2015. doi: 10.1093/mnras/stv470.

J. C. Schwartz and N. B. Cowan. Knot a Bad Idea: Testing BLISS Mapping for Spitzer Space Telescope Photometry. *Publications of the ASP*, 129(971):014001, Jan. 2017. doi: 10.1088/1538-3873/129/971/014001.

J. C. Schwartz, Z. Kashner, D. Jovmir, and N. B. Cowan. Phase Offsets and the Energy Budgets of Hot Jupiters. *The Astrophysical Journal*, 850(2):154, Dec. 2017. doi: 10.3847/1538-4357/aa9567.

G. Schwarz. Estimating the Dimension of a Model. *Annals of Statistics*, 6(2):461–464, July 1978.

A. P. Showman and T. Guillot. Atmospheric circulation and tides of "51 Pegasus b-like" planets. *Astronomy and Astrophysics*, 385:166–180, Apr. 2002. doi: 10.1051/0004-6361:20020101.

A. P. Showman, C. S. Cooper, J. J. Fortney, and M. S. Marley. Atmospheric Circulation of Hot Jupiters: Three-dimensional Circulation Models of HD 209458b and HD 189733b with Simplified Forcing. *The Astrophysical Journal*, 682(1):559–576, July 2008. doi: 10.1086/589325.

A. P. Showman, J. J. Fortney, Y. Lian, M. S. Marley, R. S. Freedman, H. A. Knutson, and D. Charbonneau. Atmospheric Circulation of Hot Jupiters: Coupled Radiative-Dynamical General Circulation Model Simulations of HD 189733b and HD 209458b. *The Astrophysical Journal*, 699(1):564–584, July 2009. doi: 10.1088/0004-637X/699/1/564.

A. Shporer, I. Wong, C. X. Huang, M. R. Line, K. G. Stassun, T. Fetherolf, S. R. Kane, L. G. Bouma, T. Daylan, M. N. Güenther, G. R. Ricker, D. W. Latham, R. Vanderspek, S. Seager, J. N. Winn, J. M. Jenkins, A. Glidden, Z. Berta-Thompson, E. B. Ting, J. Li, and K. Haworth. TESS Full Orbital Phase Curve of the WASP-18b System. *The Astronomical Journal*, 157(5):178, May 2019. doi: 10.3847/1538-3881/ab0f96.

D. K. Sing, J. J. Fortney, N. Nikolov, H. R. Wakeford, T. Kataria, T. M. Evans, S. Aigrain, G. E. Ballester, A. S. Burrows, D. Deming, J.-M. Désert, N. P. Gibson, G. W. Henry, C. M. Huitson, H. A. Knutson, A. Lecavelier Des Etangs, F. Pont, A. P. Showman, A. Vidal-Madjar, M. H. Williamson, and P. A. Wilson. A continuum from clear to cloudy hot-Jupiter exoplanets without primordial water depletion. *Nature*, 529(7584): 59–62, Jan. 2016. doi: 10.1038/nature16068.

K. G. Stassun, K. A. Collins, and B. S. Gaudi. Accurate Empirical Radii and Masses of Planets and Their Host Stars with Gaia Parallaxes. *The Astronomical Journal*, 153 (3):136, Mar. 2017. doi: 10.3847/1538-3881/aa5df3.

K. B. Stevenson, J. Harrington, J. J. Fortney, T. J. Loredo, R. A. Hardy, S. Nymeyer, W. C. Bowman, P. Cubillos, M. O. Bowman, and M. Hardin. Transit and Eclipse Analyses of the Exoplanet HD 149026b Using BLISS Mapping. *The Astrophysical Journal*, 754(2):136, Aug. 2012a. doi: 10.1088/0004-637X/754/2/136.

K. B. Stevenson, J. Harrington, J. J. Fortney, T. J. Loredo, R. A. Hardy, S. Nymeyer, W. C. Bowman, P. Cubillos, M. O. Bowman, and M. Hardin. Transit and Eclipse Analyses of the Exoplanet HD 149026b Using BLISS Mapping. *The Astrophysical Journal*, 754(2):136, Aug. 2012b. doi: 10.1088/0004-637X/754/2/136.

K. B. Stevenson, J. Harrington, N. B. Lust, N. K. Lewis, G. Montagnier, J. I. Moses, C. Visscher, J. Blecic, R. A. Hardy, P. Cubillos, and C. J. Campo. Two nearby Sub-Earth-sized Exoplanet Candidates in the GJ 436 System. *The Astrophysical Journal*, 755(1):9, Aug. 2012c. doi: 10.1088/0004-637X/755/1/9.

K. B. Stevenson, J.-M. Désert, M. R. Line, J. L. Bean, J. J. Fortney, A. P. Showman,

T. Kataria, L. Kreidberg, P. R. McCullough, G. W. Henry, D. Charbonneau, A. Burrows, S. Seager, N. Madhusudhan, M. H. Williamson, and D. Homeier. Thermal structure of an exoplanet atmosphere from phase-resolved emission spectroscopy. *Science*, 346(6211):838–841, Nov. 2014. doi: 10.1126/science.1256758.

K. B. Stevenson, M. R. Line, J. L. Bean, J.-M. Désert, J. J. Fortney, A. P. Showman, T. Kataria, L. Kreidberg, and Y. K. Feng. Spitzer Phase Curve Constraints for WASP-43b at 3.6 and 4.5 μm. *The Astronomical Journal*, 153(2):68, Feb. 2017. doi: 10.3847/1538-3881/153/2/68.

D. Sudarsky, A. Burrows, and P. Pinto. Albedo and Reflection Spectra of Extrasolar Giant Planets. *The Astrophysical Journal*, 538(2):885–903, Aug. 2000. doi: 10.1086/309160.

P. Tamburo, A. Mandell, D. Deming, and E. Garhart. Confirming Variability in the Secondary Eclipse Depth of the Super-Earth 55 Cancri e. *The Astronomical Journal*, 155(5):221, May 2018. doi: 10.3847/1538-3881/aabd84.

X. Tan and T. D. Komacek. The Atmospheric Circulation of Ultra-hot Jupiters. *The Astrophysical Journal*, 886(1):26, Nov. 2019. doi: 10.3847/1538-4357/ab4a76.

X. Tan and A. P. Showman. Atmospheric Circulation of Tidally Locked Gas Giants with Increasing Rotation and Implications for White Dwarf-Brown Dwarf Systems. *The Astrophysical Journal*, 902(1):27, Oct. 2020. doi: 10.3847/1538-4357/abb3d4.

J. Teske, S. Xuesong Wang, A. Wolfgang, T. Gan, M. Plotnykov, D. J. Armstrong, R. P. Butler, B. Cale, J. D. Crane, W. Howard, E. L. N. Jensen, N. Law, S. A. Shectman, P. Plavchan, D. Valencia, A. Vanderburg, G. Ricker, R. Vanderspek, D. W. Latham, S. Seager, J. W. Winn, J. M. Jenkins, V. Adibekyan, D. Barrado, S. C. C. Barros, D. J. A. Brown, E. M. Bryant, J. Burt, D. A. Caldwell, D. Charbonneau, R. Cloutier, K. A. Collins, K. I. Collins, N. D. Colon, D. M. Conti, O. D. S. Demangeon, J. D. Eastman, M. Elmufti, F. Feng, E. Flowers, N. M. Guerrero, S. Hojjatpanah, J. M. Irwin, G. Isopi, J. Lillo-Box, F. Mallia, B. Massey, M. Mori, S. E. Mullally, N. Narita,

T. Nishiumi, A. Osborn, M. Paegert, J. Pitogo de Leon, S. N. Quinn, M. Reefe, R. P. Schwarz, A. Shporer, A. Soubkiou, S. G. Sousa, C. Stockdale, P. A. Strøm, T.-G. Tan, P. Tenenbaum, P. J. Wheatley, J. Wittrock, D. A. Yahalomi, F. Zohrabi, and B. Zouhair. The Magellan-TESS Survey I: Survey Description and Mid-Survey Results. *arXiv e-prints*, art. arXiv:2011.11560, Nov. 2020.

The Theano Development Team, R. Al-Rfou, G. Alain, A. Almahairi, C. Angermueller, D. Bahdanau, N. Ballas, F. Bastien, J. Bayer, A. Belikov, A. Belopolsky, Y. Bengio, A. Bergeron, J. Bergstra, V. Bisson, J. Bleecher Snyder, N. Bouchard, N. Boulanger-Lewandowski, X. Bouthillier, A. de Brébisson, O. Breuleux, P.-L. Carrier, K. Cho, J. Chorowski, P. Christiano, T. Cooijmans, M.-A. Côté, M. Côté, A. Courville, Y. N. Dauphin, O. Delalleau, J. Demouth, G. Desjardins, S. Dieleman, L. Dinh, M. Ducoffe, V. Dumoulin, S. Ebrahimi Kahou, D. Erhan, Z. Fan, O. Firat, M. Germain, X. Glorot, I. Goodfellow, M. Graham, C. Gulcehre, P. Hamel, I. Harlouchet, J.-P. Heng, B. Hidasi, S. Honari, A. Jain, S. Jean, K. Jia, M. Korobov, V. Kulkarni, A. Lamb, P. Lamblin, E. Larsen, C. Laurent, S. Lee, S. Lefrancois, S. Lemieux, N. Léonard, Z. Lin, J. A. Livezey, C. Lorenz, J. Lowin, Q. Ma, P.-A. Manzagol, O. Mastropietro, R. T. McGibbon, R. Memisevic, B. van Merriënboer, V. Michalski, M. Mirza, A. Orlandi, C. Pal, R. Pascanu, M. Pezeshki, C. Raffel, D. Renshaw, M. Rocklin, A. Romero, M. Roth, P. Sadowski, J. Salvatier, F. Savard, J. Schlüter, J. Schulman, G. Schwartz, I. Vlad Serban, D. Serdyuk, S. Shabanian, É. Simon, S. Spieckermann, S. Ramana Subramanyam, J. Sygnowski, J. Tanguay, G. van Tulder, J. Turian, S. Urban, P. Vincent, F. Visin, H. de Vries, D. Warde-Farley, D. J. Webb, M. Willson, K. Xu, L. Xue, L. Yao, S. Zhang, and Y. Zhang. Theano: A Python framework for fast computation of mathematical expressions. *arXiv e-prints*, art. arXiv:1605.02688, May 2016.

D. P. Thorngren, J. J. Fortney, E. D. Lopez, T. A. Berger, and D. Huber. Slow Cooling and Fast Reinflation for Hot Jupiters. *arXiv e-prints*, art. arXiv:2101.05285, Jan. 2021.

G. Tinetti, P. Drossart, P. Eccleston, P. Hartogh, A. Heske, J. Leconte, G. Micela, M. Ollivier, G. Pilbratt, L. Puig, D. Turrini, B. Vandenbussche, P. Wolkenberg, J.-

P. Beaulieu, L. A. Buchave, M. Ferus, M. Griffin, M. Guedel, K. Justtanont, P.-O. Lagage, P. Machado, G. Malaguti, M. Min, H. U. Nørgaard-Nielsen, M. Rataj, T. Ray, I. Ribas, M. Swain, R. Szabo, S. Werner, J. Barstow, M. Burleigh, J. Cho, V. C. du Foresto, A. Coustenis, L. Decin, T. Encrenaz, M. Galand, M. Gillon, R. Helled, J. C. Morales, A. G. Muñoz, A. Moneti, I. Pagano, E. Pascale, G. Piccioni, D. Pinfield, S. Sarkar, F. Selsis, J. Tennyson, A. Triaud, O. Venot, I. Waldmann, D. Waltham, G. Wright, J. Amiaux, J.-L. Auguères, M. Berthé, N. Bezawada, G. Bishop, N. Bowles, D. Coffey, J. Colomé, M. Crook, P.-E. Crouzet, V. Da Peppo, I. E. Sanz, M. Focardi, M. Frericks, T. Hunt, R. Kohley, K. Middleton, G. Morgante, R. Ottensamer, E. Pace, C. Pearson, R. Stamper, K. Symonds, M. Rengel, E. Renotte, P. Ade, L. Affer, C. Alard, N. Allard, F. Altieri, Y. André, C. Arena, I. Argyriou, A. Aylward, C. Baccani, G. Bakos, M. Banaszkiewicz, M. Barlow, V. Batista, G. Bellucci, S. Benatti, P. Bernardi, B. Bézard, M. Blecka, E. Bolmont, B. Bonfond, R. Bonito, A. S. Bonomo, J. R. Brucato, A. S. Brun, I. Bryson, W. Bujwan, S. Casewell, B. Charnay, C. C. Pestellini, G. Chen, A. Ciaravella, R. Claudi, R. Clédassou, M. Damasso, M. Damiano, C. Danielski, P. Deroo, A. M. Di Giorgio, C. Dominik, V. Doublier, S. Doyle, R. Doyon, B. Drummond, B. Duong, S. Eales, B. Edwards, M. Farina, E. Flaccomio, L. Fletcher, F. Forget, S. Fossey, M. Fränz, Y. Fujii, Á. García-Piquer, W. Gear, H. Geoffray, J. C. Gérard, L. Gesa, H. Gomez, R. Graczyk, C. Griffith, D. Grodent, M. G. Guarcello, J. Gustin, K. Hamano, P. Hargrave, Y. Hello, K. Heng, E. Herrero, A. Hornstrup, B. Hubert, S. Ida, M. Ikoma, N. Iro, P. Irwin, C. Jarchow, J. Jaubert, H. Jones, Q. Julien, S. Kameda, F. Kerschbaum, P. Kervella, T. Koskinen, M. Krijger, N. Krupp, M. Lafarga, F. Landini, E. Lellouch, G. Leto, A. Luntzer, T. Rank-Lüftinger, A. Maggio, J. Maldonado, J.-P. Maillard, U. Mall, J.-B. Marquette, S. Mathis, P. Maxted, T. Matsuo, A. Medvedev, Y. Miguel, V. Minier, G. Morello, A. Mura, N. Narita, V. Nascimbeni, N. Nguyen Tong, V. Noce, F. Oliva, E. Palle, P. Palmer, M. Pancrazzi, A. Papageorgiou, V. Parmentier, M. Perger, A. Petralia, S. Pezzuto, R. Pierrehumbert, I. Pillitteri, G. Piotto, G. Pisano, L. Prisinzano, A. Radioti, J.-M. Réess, L. Rezac, M. Rocchetto, A. Rosich, N. Sanna, A. Santerne, G. Savini, G. Scandariato, B. Sicardy, C. Sierra, G. Sindoni, K. Skup, I. Snellen, M. Sobiecki, L. Soret, A. Sozzetti, A. Stiepen, A. Strugarek, J. Taylor, W. Taylor, L. Terenzi, M. Tessenyi, A. Tsiaras, C. Tucker, D. Valencia, G. Vasisht, A. Vazan, F. Vilardell, S. Vinatier, S. Viti, R. Waters, P. Wawer, A. Wawrzaszek, A. Whitworth, Y. L. Yung, S. N. Yurchenko, M. R. Z. Osorio, R. Zellem, T. Zingales, and F. Zwart. A chemical survey of exoplanets with ARIEL. *Experimental Astronomy*, 46(1):135–209, Nov. 2018. doi: 10.1007/s10686-018-9598-x.

I. P. Waldmann. Of "Cocktail Parties" and Exoplanets. *The Astrophysical Journal*, 747 (1):12, Mar. 2012. doi: 10.1088/0004-637X/747/1/12.

W. Wang, R. van Boekel, N. Madhusudhan, G. Chen, G. Zhao, and T. Henning. Ground-based Detections of Thermal Emission from the Dense Hot Jupiter WASP-43b in the H and K $_s$ Bands. *The Astrophysical Journal*, 770(1):70, June 2013. doi: 10.1088/0004-637X/770/1/70.

S. Watanabe. Asymptotic Equivalence of Bayes Cross Validation and Widely Applicable Information Criterion in Singular Learning Theory. *arXiv e-prints*, art. arXiv:1004.2316, Apr. 2010.

J. N. Winn. *Exoplanet Transits and Occultations*, pages 55–77. University of Arizona Press, 2010.

J. G. Winters, A. A. Medina, J. M. Irwin, D. Charbonneau, N. Astudillo-Defru, E. P. Horch, J. D. Eastman, E. H. Vrijmoet, T. J. Henry, H. Diamond-Lowe, E. Winston, T. Barclay, X. Bonfils, G. R. Ricker, R. Vanderspek, D. W. Latham, S. Seager, J. N. Winn, J. M. Jenkins, S. Udry, J. D. Twicken, J. K. Teske, P. Tenenbaum, F. Pepe, F. Murgas, P. S. Muirhead, J. Mink, C. Lovis, A. M. Levine, S. Lépine, W.-C. Jao, C. E. Henze, G. Furész, T. Forveille, P. Figueira, G. A. Esquerdo, C. D. Dressing, R. F. Díaz, X. Delfosse, C. J. Burke, F. Bouchy, P. Berlind, and J.-M. Almenara. Three Red Suns in the Sky: A Transiting, Terrestrial Planet in a Triple M-dwarf System at 6.9 pc. *The Astronomical Journal*, 158(4):152, Oct. 2019. doi: 10.3847/1538-3881/ab364d.

I. Wong, H. A. Knutson, N. B. Cowan, N. K. Lewis, E. Agol, A. Burrows, D. Deming, J. J. Fortney, B. J. Fulton, J. Langton, G. Laughlin, and A. P. Showman. Constraints on the Atmospheric Circulation and Variability of the Eccentric Hot Jupiter XO-3b. *The Astrophysical Journal*, 794(2):134, Oct. 2014. doi: 10.1088/0004-637X/794/2/134.

I. Wong, H. A. Knutson, N. K. Lewis, T. Kataria, A. Burrows, J. J. Fortney, J. Schwartz, E. Agol, N. B. Cowan, D. Deming, J.-M. Désert, B. J. Fulton, A. W. Howard, J. Langton, G. Laughlin, A. P. Showman, and K. Todorov. 3.6 and 4.5 μm Phase Curves of the Highly Irradiated Eccentric Hot Jupiter WASP-14b. *The Astrophysical Journal*, 811(2):122, Oct. 2015. doi: 10.1088/0004-637X/811/2/122.

I. Wong, H. A. Knutson, T. Kataria, N. K. Lewis, A. Burrows, J. J. Fortney, J. Schwartz, A. Shporer, E. Agol, N. B. Cowan, D. Deming, J.-M. Désert, B. J. Fulton, A. W. Howard, J. Langton, G. Laughlin, A. P. Showman, and K. Todorov. 3.6 and 4.5 μm Spitzer Phase Curves of the Highly Irradiated Hot Jupiters WASP-19b and HAT-P-7b. *The Astrophysical Journal*, 823(2):122, June 2016. doi: 10.3847/0004-637X/823/2/122.

I. Wong, B. Benneke, A. Shporer, T. Fetherolf, S. R. Kane, G. R. Ricker, R. Vanderspek, S. Seager, J. N. Winn, K. A. Collins, I. Mireles, R. Morris, P. Tenenbaum, E. B. Ting, S. Rinehart, and J. N. Villaseñor. TESS Phase Curve of the Hot Jupiter WASP-19b. *The Astronomical Journal*, 159(3):104, Mar. 2020a. doi: 10.3847/1538-3881/ab6d6e.

I. Wong, A. Shporer, D. Kitzmann, B. M. Morris, K. Heng, H. J. Hoeijmakers, B.-O. Demory, J. P. Ahlers, M. Mansfield, J. L. Bean, T. Daylan, T. Fetherolf, J. E. Rodriguez, B. Benneke, G. R. Ricker, D. W. Latham, R. Vanderspek, S. Seager, J. N. Winn, J. M. Jenkins, C. J. Burke, J. L. Christiansen, Z. Essack, M. E. Rose, J. C. Smith, P. Tenenbaum, and D. Yahalomi. Exploring the Atmospheric Dynamics of the Extreme Ultrahot Jupiter KELT-9b Using TESS Photometry. *The Astronomical Journal*, 160(2):88, Aug. 2020b. doi: 10.3847/1538-3881/aba2cb.

J. T. Wright, G. W. Marcy, A. W. Howard, J. A. Johnson, T. D. Morton, and D. A. Fischer. The Frequency of Hot Jupiters Orbiting nearby Solar-type Stars. *The Astrophysical Journal*, 753(2):160, July 2012. doi: 10.1088/0004-637X/753/2/160.

R. K. Yadav and D. P. Thorngren. Estimating the Magnetic Field Strength in Hot Jupiters. *The Astrophysical Journal Letters*, 849(1):L12, Nov. 2017. doi: 10.3847/2041-8213/aa93fd.

R. T. Zellem, N. K. Lewis, H. A. Knutson, C. A. Griffith, A. P. Showman, J. J. Fortney, N. B. Cowan, E. Agol, A. Burrows, D. Charbonneau, D. Deming, G. Laughlin, and J. Langton. The 4.5 μm Full-orbit Phase Curve of the Hot Jupiter HD 209458b. *The Astrophysical Journal*, 790(1):53, July 2014. doi: 10.1088/0004-637X/790/1/53.

M. Zhang, H. A. Knutson, T. Kataria, J. C. Schwartz, N. B. Cowan, A. P. Showman, A. Burrows, J. J. Fortney, K. Todorov, J.-M. Desert, E. Agol, and D. Deming. Phase Curves of WASP-33b and HD 149026b and a New Correlation between Phase Curve Offset and Irradiation Temperature. *The Astronomical Journal*, 155(2):83, Feb. 2018. doi: 10.3847/1538-3881/aaa458.

X. Zhang and A. P. Showman. Effects of Bulk Composition on the Atmospheric Dynamics on Close-in Exoplanets. *The Astrophysical Journal*, 836(1):73, Feb. 2017. doi: 10.3847/1538-4357/836/1/73.

G. Zhou, D. D. R. Bayliss, L. Kedziora-Chudczer, G. Salter, C. G. Tinney, and J. Bailey. K_s-band secondary eclipses of WASP-19b and WASP-43b with the Anglo-Australian Telescope. *Monthly Notices of the Royal Astronomical Society*, 445(3):2746–2757, Dec. 2014. doi: 10.1093/mnras/stu1893.